Understanding Attitude Behavior of Inactive GLONASS Satellites using Spin Period Evolution

Inaugural dissertation
of the Faculty of Science
University of Bern

presented by

Abdul Rachman

from Indonesia

Supervisor of the doctoral thesis:
Prof. Dr. T. Schildknecht
Astronomical Institute of University of Bern

Co-supervisor of the doctoral thesis:
Dr. A. Vananti
Astronomical Institute of University of Bern

Understanding Attitude Behavior of Inactive GLONASS Satellites using Spin Period Evolution

Inaugural dissertation
of the Faculty of Science
University of Bern

presented by

Abdul Rachman

from Indonesia

Supervisor of the doctoral thesis:
Prof. Dr. T. Schildknecht
Astronomical Institute of University of Bern

Co-supervisor of the doctoral thesis:
Dr. A. Vananti
Astronomical Institute of University of Bern

Accepted by the Faculty of Science.

Bern, 05.07.2023

The Dean:
Prof. Dr. Marco Herwegh

Abstract

Light curve analysis of defunct satellites is critical for characterizing the rotational motion of space debris. Accurate understanding of this aspect will benefit active debris removal and on-orbit servicing missions as parts of solution to the space debris issue. In this study, we explored the attitude behavior of inactive GLONASS satellites, specifically the repeating triangular pattern observed in their spin period evolution. We utilized a large amount of data available in the light curve database maintained by the Astronomical Institute of the University of Bern (AIUB).

The morphology of the inactive GLONASS light curves typically features four peaks in two pairs and is attributed to the presence of four evenly distributed thermal control flaps or radiators on the satellite bus. The analysis of the periods extracted from the light curves shows that nearly all of the inactive GLONASS satellites are rotating and exhibit the oscillating pattern in their spin period evolution with an increasing or decreasing secular trend. Interestingly, three objects were found to cycle between uniform and tumbling motion, indicative of the YORP effect. Through modeling and simulation, we found that the oscillating pattern is likely a result of canted solar panels that provide an asymmetry in the satellite model and enable a wind wheel or fan-like mechanism to operate. The secular trend is a consequence of differing values of the specular reflection coefficients of the front and back side of the solar panels.

Using empirical models constructed from the spin period evolution of 18 selected objects, we found significant variations in the average spin period and amplitude of the oscillations, which range from 8.11 sec to 469.58 sec and 1.10 sec to 513.24 sec, respectively. However, the average oscillation period remains relatively constant at around 1 year. Notably, the average spin period correlates well with the average amplitude. Also, the selected objects tend to rotate faster over their lifetime and the rate is correlated with the angular acceleration. The empirical models can be used to estimate the spin period at any point in time within the interval covered by the observations and also in the future or in the past assuming that the oscillating pattern is preserved and shows a (roughly) linear trend.

Acknowledgments

Contents

List of Figures

List of Tables

List of Symbols

N torque $(\mathrm{kg} \cdot \mathrm{m}^2/\mathrm{s}^2)$ or $(\mathrm{N} \cdot \mathrm{m})$
I moment of inertia $(\mathrm{kg} \cdot \mathrm{m}^2)$
ω angular velocity $(\mathrm{rad/s})$
L angular momentum $(\mathrm{kg} \cdot \mathrm{m}^2/\mathrm{s})$

Abbreviations

ADR	Active Debris Removal
AIUB	Astronomical Institute of the University of Bern
COSPAR	Committee On Space Research
GEO	Geostationary Earth Orbit
GNSS	Global Navigation Satellite Systems
GSO	Geosynchronous Earth Orbit
GTO	Geosynchronous Transfer Orbit
IGSO	Inclined Geosynchronous orbit
iOTA	in-Orbit Tumbling Analysis
LEO	Low Earth Orbit
LRA	Laser Retroreflector Array
MEO	Medium Earth Orbit
NASA ODPO	NASA Orbital Debris Program Office
RSO	Resident Space Object
SLR	Satellite Laser Ranging
SSN	Space Surveillance Network
TLE	Two-Line Element
YORP	Yarkovsky-O'Keefe-Radzievskii-Paddack
ZIMLAT	Zimmerwald Laser and Astrometry Telescope

1. Introduction

This chapter explains what motivates this study in Section 1.1, and then its objective, the methodology to achieve the objective, and how the dissertation is structured in Section 1.2.

1.1. Motivation

Modern human civilization depends on space technology. Orbiting spacecraft are now vital as communications links, navigation beacons, scientific investigation platforms, and providers of remote sensing data for weather, climate, land use, and national security purposes (*National Research Council*, 1995). However, as the number of spacecrafts increases, the number of undesirable excesses related to space activities also escalates. These undesirable excesses are coming from any artificial object in orbit which does not have any useful function. They include nonfunctional spacecraft, spent rocket bodies, mission-related objects, the products of spacecraft surface deterioration, and fragments from spacecraft and rocket body breakups (Fig. 1.1). All of these objects are called space debris which may collide with operational spacecraft in hypervelocity speed of around 10 km/s in average. Therefore, even a small debris of size less than 1 mm can still harm vulnerable parts of a spacecraft. In addition, unlike some active satellites that can be controlled to change their motion to avoid a collision, all space debris is unmaneuverable. It is the combination of speed and lack of control that makes space debris such a threat to the space activity.

Since 1994 the Scientific and Technical Subcommittee (STSC) of the United Nations has been discussing space debris issue annually (*NASA*, 2008). Nevertheless, two events that contributed significantly (and instantaneously) to the population of space debris were still taking place as can be seen in the growth of fragmentation debris as shown in Fig. 1.1. With a purpose to test their anti satellite (ASAT) system, China shoot their own defunct polar-orbiting weather satellite named FENGYUN-1C in January 2007 at an altitude of nearly 900 km. NASA Orbital Debris Program Office estimated that more than 35,000 pieces of debris larger than 1 cm was produced during the event (*Kelso*, 2007). U.S. Space Surveillance Network has cataloged nearly 3,400 distinct debris bigger than 5 cm until January 2014 and it was predicted that 50% of the debris could still be in orbit 20 years after the event due to its high altitude (*NASA ODPO*, 2014). A subsequent event that also adds a significant contribution to the population of space debris took place in February 2009 when
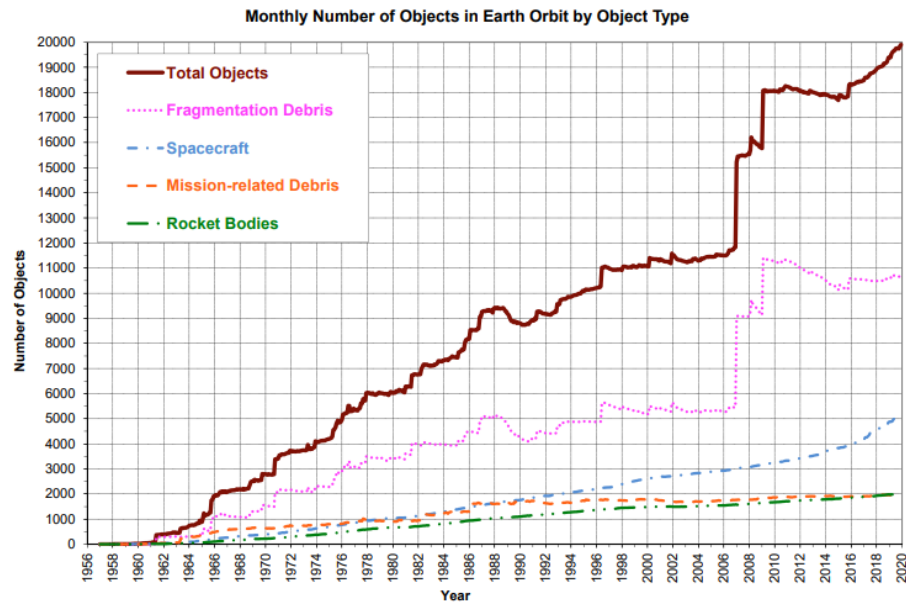
Figure 1.1.: Historical monthly number of artificial objects in Earth orbit (*NASA ODPO*, 2020a).

IRIDIUM-33 collided with COSMOS-2251 at an altitude of around 790 km. The first satellite is an active American communication satellite while the latter is a defunct Russian communication satellite. The event produced more than 2,000 cataloged debris and marked the first accidental collision between two intact objects (*NASA ODPO*, 2013).

Currently, two methods have been identified to protect the space environment in terms of space debris issue. The first method is through the creation of a set of mitigation guidelines, which have been discussed since the 1980s (*NASA*, 2008). So far, several countries and organizations have taken this route including the United States, Russia, Japan and the European Space Agency (ESA). The UN also makes its own guidelines to be implemented voluntarily by member countries. The guideline is based on previous guidelines that have been developed by various countries and organizations which take into account treaties and principles of the United Nations in the space domain. However, later theoretical studies show that mitigation (prevention) alone is not sufficient to stabilize the growing amount of space debris (*Liou and Johnson*, 2008). The number will continue to escalate even without further launches (which is considered impossible) according to the so-called Kessler Syndrome (*Kessler and Cour-Palais*, 1978). This result leads to a conclusion that it is necessary to also perform a second method namely remediation (treatment) of the space debris population.

Remediation is performed by moving a selected debris to a desired orbit (of little operational value) or bringing it back to Earth. Compared to the mitigation, the remediation is more assertive, therefore it is also called active debris removal (ADR).

Several methods have been proposed for carrying out ADR missions, for example by using a special satellite equipped with a robotic arm to capture a target and then to drag it into the atmosphere. Another method uses a net that is thrown at a target to wrap it and then the satellite connected by a rope (tether) to the target pulls it into the atmosphere. However, unlike the mitigation of space debris that has been around for decades, remediation is still in an experimental phase. One of the commonly considered challenges that has to be overcome with this method is the uncooperative nature of the target debris. It is common for a large debris to tumble since it still possesses angular momentum left from its attitude control system when the failure occurred (*Nishida and Kawamoto*, 2011). Therefore, conducting an ADR mission to a debris object will be more difficult compared with a cooperative target.

The Astronomical Institute of the University of Bern (AIUB) in Switzerland has produced and maintained a light curve database since January 2007 which contains more than 3000 light curves from 512 selected space objects (*Rachman et al.*, 2017). The objects cover all orbital regions and different types of objects. The light curve itself is the variation of relative magnitude as a function of time with duration spans from 3 until 20 minutes and sampling interval of about twice the exposure time. It can be used to determine attitude states of space debris including spin period and spin axis orientation (*Yanagisawa and Kurosaki*, 2012; *Silha et al.*, 2015; *Earl et al.*, 2018). Fig. 1.2 shows that inside the database, light curves that indicate a rotating behavior of the related objects (either fast or slow rotator) constitute the biggest portion of the database compared with other attitude groups. The largest number of rotators was located in the GEO/other (73 out of 167 rotators) but the largest percentage was located in the MEO (70.8%) (*Rachman et al.*, 2017).
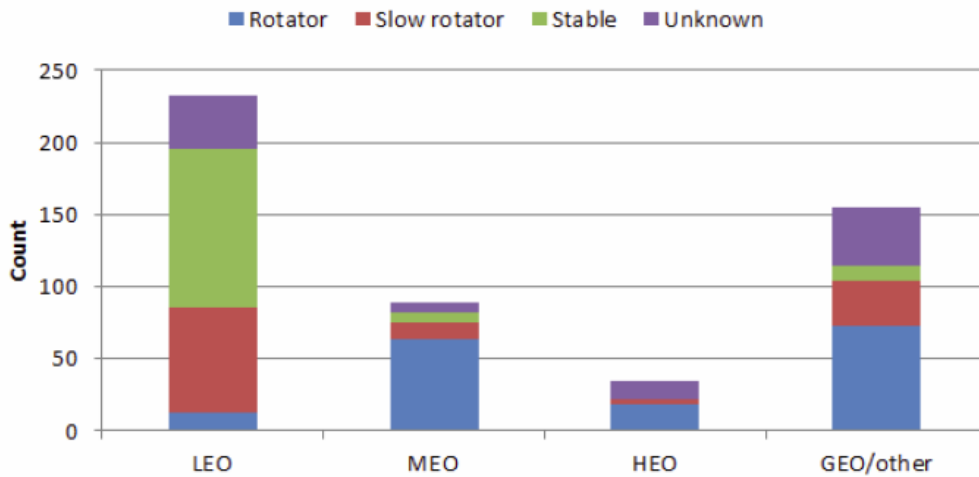
Figure 1.2.: Number of objects in the AIUB light curve database as a function of orbital type and attitude group (*Rachman et al.*, 2017).

In AIUB light curve database, the MEO rotators are mostly defunct GLONASS navigation satellites. Historical spin period evolution of some of these objects re-

vealed a roughly annual oscillating pattern which looks like a series of peaks which form triangular shapes consist of linear segments as shown in Fig. 1.3. Twenty six objects were found having this pattern clearly in the database and they are all defunct GLONASS satellites. Most of them are GLONASS block IIv satellites which have been considered debris for more than a decade. Different satellites possess different patterns but they are so persistent that for these objects someone can even predict future spin periods of the satellites by utilizing them (*Rachman et al.*, 2018). While the study of spin state evolution of defunct satellites have been carried out by several researchers (*Albuja and Scheeres*, 2013; *Earl*, 2017; *Benson et al.*, 2017), we noticed that the objects concerned are all in geosynchronous orbits. In addition, compared with GLONASS satellites, those objects usually lack retro reflector arrays which can be used to determine the spin state of an inactive satellite (*Pittet et al.*, 2018). All GLONASS satellites are equipped with retro-reflector panels that allow them to act as cooperative targets to laser instruments. This allows the objects to be observed not only by optical telescopes but also with laser equipment (*Kirchner et al.*, 2017; *Silha et al.*, 2017). The possibility to observe space debris using more than one observation techniques will increase the quality of the observation itself. In addition to its benefit for ADR missions, knowledge of the attitude of inactive spacecraft will also benefit on-orbit servicing missions which can also be a part of the solution to the space debris issue (*Wilde et al.*, 2019).
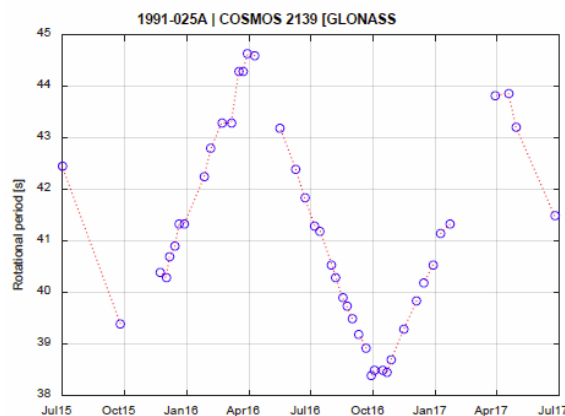
Figure 1.3.: An example of a spin period evolution of a GLONASS satellite taken from *Rachman et al.* (2018).

1.2. Objective, methodology, and structure

The objective of this study is to understand the oscillating pattern which we have seen in the spin period evolution of some of the inactive GLONASS satellites inside the AIUB light curve database. To achieve this, we use a methodology that consists of five steps.

First Analyzing the results of light curve data processing already available in the database for all GLONASS satellites.

Second Updating data of all GLONASS satellites inside the database. This process includes planning new observations, doing the observations, and processing the resulting light curves which are conducted on a daily basis. We performed the planning and the data processing by using several scripts developed at AIUB. We performed the data acquisition (together with other observers) using the optical system of ZIMLAT (Zimmerwald Laser and Astrometric Telescope) at Zimmerwald Observatory (owned by AIUB) which uses a CCD camera to detect and record the incoming light. The updating process is performed since October 2016 until November 2020. We developed a software to improve the process of planning and data processing and to better access the database as well.

Third Analyzing new data of all GLONASS satellites for characterization of their spin period evolution.

Fourth Doing simulation to understand the physical drivers that are responsible for the apparent trend of the spin period evolution of the selected objects. It is performed using iOTA which is a software for debris attitude motion measurements and modeling (created through collaboration between AIUB, ESA, and HTG) and other available tools. We simulated the rotation rate of one of the GLONASS satellites in the database (with a clear oscillating pattern in their spin period evolution) under different attitude conditions. For this, we created a satellite model with cylinder shape for the bus and two rectangular plates as wings for the solar panels. The validation is conducted by comparing the resulted spin period evolution with a real spin period evolution from a selected satellite. The comparison is performed iteratively until the two patterns can be considered matched.

Fifth Interpreting all the results.

This dissertation begins with the *first chapter* by introducing the space debris issue which motivates this study, stating its objective, and how to achieve it. In the *second chapter*, it gives a review on the space debris topic then describes the theory of rigid body dynamics and forces/torques typically acting on spacecraft which are necessary to explain their attitude behavior. It then reports some progresses and results from several attitude studies of inactive satellites especially the ones which analyze their spin period evolution. It closes the chapter by describing some characteristics of GLONASS satellites. In the *third chapter*, it describes how the AIUB light curve database is produced and maintained. The daily tasks involved three successive phases which are planning, observation, and data processing. Regarding these phases, it also explains what efforts have been given to improve the planning and data processing phases during the time of this study. Finally, after describing the latest status of the whole database, it describes specifically the database col-

lection of the inactive GLONASS satellites. In the *fourth chapter*, it presents the main part of this study which is the spin period evolution of inactive GLONASS satellites. It starts the chapter by describing the characteristic of spin period evolution of selected objects from the group as obtained from observations. After that, it explains how to create an empirical period evolution model for the selected objects. Then, it describes how to reproduce the primary features of the oscillating pattern by creating a satellite model as a representative of the group. Then it explains how to estimate spin period values using the empirical period evolution models. It closes the chapter by interpreting all the results. And finally, in the *fifth chapter*, it gives the summary of the study and also suggests several improvements to the photometry activity conducted at AIUB and several possible future studies.

2. Literature Study

This chapter starts by giving a review on space debris including its current population, how it is measured, and the kind of instruments that are employed in the measurements. After that, it describes the potential hazard of space debris to space activities and the efforts to minimize the risk. These are all described in Section 2.1. Then, Section 2.2 describes the theory of rigid body (attitude) dynamics which is necessary to explain the attitude behavior of inactive artificial satellites. Section 2.3 explains about environmental and non-environmental torques which are the main drivers of the behavior. After that, Section 2.4 reports the progress and results of the study on inactive satellite attitudes through some selected works. The focus is given especially on the ones that are using satellite's spin period evolution as they are parallel with this study. Finally, GLONASS satellites which are the main objects of this study are introduced and some of their aspects are discussed in Section 2.5. One of those aspects is disposal mechanism which is necessary to give us a more complete description of the space debris environment around the satellites.

2.1. Space debris review

Space debris by definition is "all man-made objects, including fragments and elements thereof, in Earth orbit or re-entering the atmosphere, that are non-functional" (*UNOOSA*, 2010). This leads to an enormous size range since it does not only include large objects of several meters in size like defunct satellites and spent upper stage but also all sort of centimeter and millimeter-sized debris created by explosions and collisions of their parent objects. Moreover, it also consists of even tiny particles like paint flakes as resulted from surface degradation of the parent objects and slag or dust that are produced from solid rocket motor firings. Since all these objects are basically coming from operating satellites or rocket bodies around the Earth, they share the same regions in near-Earth space with altitudes ranging from 300 to 40,000 km. Being orbiting in the same regions with operational spacecrafts means that space debris is not only contaminating the space but also has the potential to hinder and even put future space activities to an end.
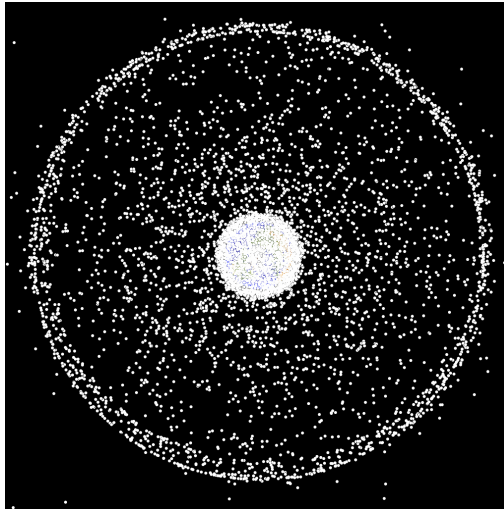
Figure 2.1.: A view from a vantage point above the north pole of objects in Earth orbit that are currently being tracked by the Space Surveillance Network as of January 1, 2019. Approximately 95% of these objects is space debris. Credit: NASA Orbital Debris Program Office (ODPO).
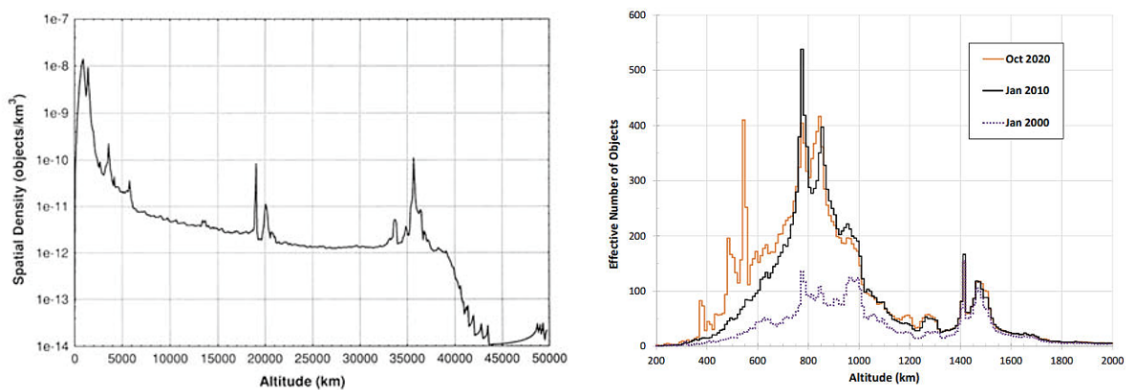
Figure 2.2.: Spatial density of objects in the 1994 US Space Command Satellite Catalog (*National Research Council*, 1995) (left) and effective numbers of objects per 10 km altitude bin between 200 and 2000 km altitude at three different epochs (*NASA ODPO*, 2020c) (right). These are objects, approximately 10 cm and larger, tracked by the Space Surveillance Network.

Most space debris is located in low Earth orbit (LEO) region with altitudes below 2,000 km and geostationary Earth orbit (GEO) region with altitudes of 35,786 km as depicted in Fig. 2.1. In the figure, the LEO region is the one that now appears almost completely covers the Earth (at the center) while the GEO region is the one that looked like a ring around the Earth. However, we can clearly see in the figure that space objects also populate the area between those two regions which is called medium Earth orbit (MEO) region. Actually, objects in this area concentrate at

an altitude of approximately 20,200 km in a special orbit called semi-synchronous orbit. Therefore, space debris is mostly found in those three regions which represent valuable resources because they have characteristics that enable spacecraft operating within them to execute their mission more effectively (*National Research Council*, 1995). This is clearly seen on the left side of Fig. 2.2 which shows how the spatial densities of objects in those three regions stand out among others. Focusing on LEO region only, we witnessed a sharp increase in its density in the last 20 years as depicted on the right side of the figure. This happened due to fragments generated from the FENGYUN-1C anti satellite test in 2007 and the accidental collision between COSMOS-2251 and the operational IRIDIUM-33 spacecraft in 2009 and later (after 2010) by the on-going build-up of the STARLINK large constellation and the proliferation of CubeSats below about 650 km altitude as shown on the right side of the figure.
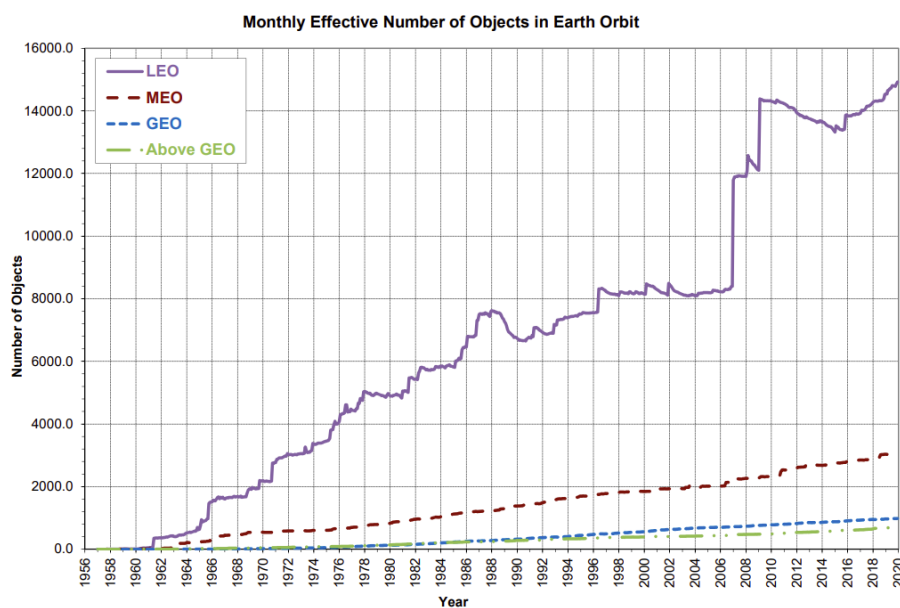
Figure 2.3.: Historical monthly effective number of artificial objects in Earth orbit (*NASA ODPO*, 2020b).

Compared with other regions, the LEO region is the most dynamic as can be seen in Fig. 2.3. The figure shows monthly effective number of cataloged objects in Earth orbit by orbital regime cataloged by the U.S. Space Surveillance Network (SSN) except those with SSN numbers of 80,000 and greater. In the figure, LEO includes resident space objects (RSOs) with altitudes within or crossing below 2,000 km; MEO RSOs with altitudes within or crossing the range from 2,000 km to 35,586 km; GEO RSOs with altitudes within or crossing the range from 35,586 km to 35,986 km; and the remainder (above GEO) with altitudes within or crossing the range from 35,986 km to 600,000 km. "Effective" number sums the fraction of each orbit that falls within the specified ranges. Cataloged objects without available orbital

elements are excluded in the graph. The two substantial jumps after 2006 correspond to the two disastrous events that took place in January 2007 and February 2009 that have been mentioned in the previous paragraph. Regarding their mass, all the regions share a similar trend where the total mass steadily increases since the beginning of the space age. Total masses of cataloged objects in LEO, MEO, and GEO are currently around 3200 tons, 2250 tons, and 1900 tons, respectively (*NASA ODPO*, 2020b).
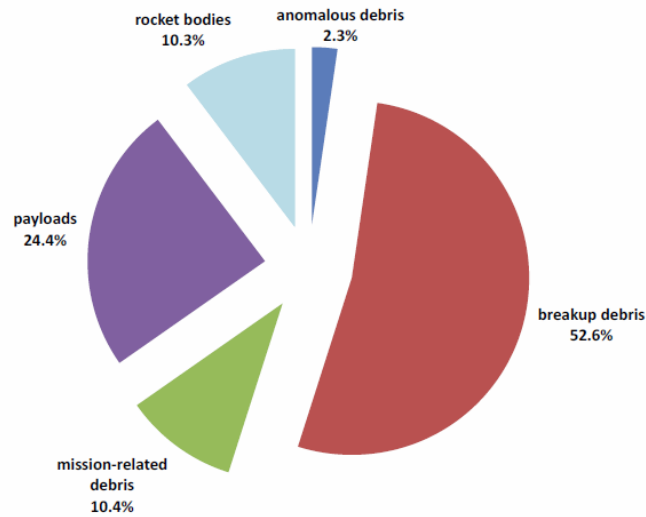
Figure 2.4.: Relative segments of the cataloged in-orbit Earth satellite population (*NASA ODPO*, 2018).
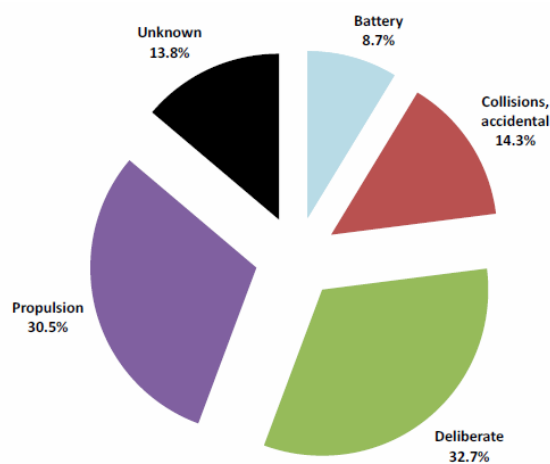
Figure 2.5.: Proportion of cataloged satellite breakup debris remaining in orbit (*NASA ODPO*, 2018).

More than half of the in-orbit artificial satellites population are smaller objects produced from fragmentation or breakups of their parent objects as shown in Fig.

2.4. A satellite breakup is usually a destructive disassociation of an orbital payload, rocket body, or structure, often with a wide range of ejecta velocities (*NASA ODPO*, 2018). It may be accidental or the result of intentional actions, e.g., due to a propulsion system malfunction or a space weapons test, respectively. An anomalous event is the unplanned separation (usually at low velocity) of one or more detectable objects from a parent object, which remains essentially intact. It can be caused by material deterioration of items such as thermal blankets, protective shields, solar panels, or by the impact of small particles. Basically, a satellite breakup produces considerably more debris, both trackable and non-trackable, than an anomalous event. Mission-related debris result from the intentional release of objects, usually in small numbers, during normal on-orbit operations (e.g. objects ejected during the deployment, activation, and de-orbit of payloads and during manned operations). Also from the figure we can see that only about 10% of the population are rocket bodies and 24% are payloads. Operational satellites only contributes about 5% of the whole population.

Propulsion-related events and deliberate actions are the primary causes of satellite breakups as shown in Fig. 2.5, although the cause for almost one in four breakups remains uncertain (*NASA ODPO*, 2018). The most serious deliberate actions so far is the FENGYUN-1C event in January 2007 due to the high altitude of the event. Propulsion-related breakups, currently the most frequent class (it was deliberate actions previously), include catastrophic malfunctions during orbital injection or maneuvers, subsequent explosions based on residual propellants, and failures of active attitude control systems. Rocket body events are carried as "Unknown" until a failure mechanism can be confidently identified for that rocket body design and is associated with a given rocket body event. *NASA ODPO* (2018) also reported that the rate of satellite breakups increased noticeably in the last 40 years at an average pace of approximately four fragmentation per year since 2001 and that an absolute majority of the satellite breakup debris in orbit today have originated from payloads. In the case of the latter, it was mostly due to the two fragmentation events after 2007 that we have mentioned before.

Our knowledge on space debris population and characteristics comes from various methods of measurements (due to the enormous range of sizes and altitudes of space debris) and modeling. In general, radar measurements have been used for lower altitudes and optical measurements for higher altitude orbits. The reason for this is that optical telescopes have higher sensitivity in terms of object size at large distances: while the radar sensitivity falls off proportional to the distance to the fourth, the sensitivity of optical instruments is only reduced proportional to the distance squared (*Schildknecht*, 2007). For very small debris, in situ measurements such as returned spacecraft surfaces are utilized. For example in the United States, the Department of Defense maintains a catalog and ephemeris of orbital objects and debris for sizes as small as 5 to 10 cm diameter in LEO and about 1 m diameter in GEO using its worldwide network of radar and optical sensors that comprise the SSN while NASA concentrates on statistically measuring size and orbit distribution
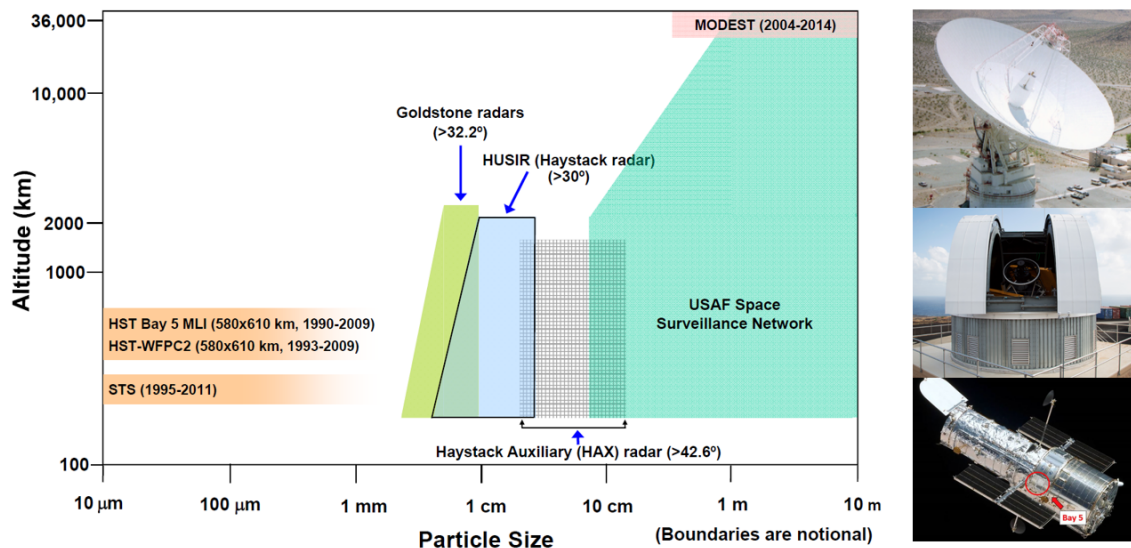
Figure 2.6.: Measurement data used by the NASA ODPO to describe the space debris populations in the near-Earth space environment (left) and type of instruments used for the data: radar, optical telescope, and in situ measurement, from top to bottom respectively (right). Credit: NASA ODPO.

of the debris environment for sizes smaller than these limits (*NASA*, 2008). For statistical measurements of the LEO debris environment for sizes less than 10 cm, NASA uses several radars namely the Haystack, the Haystack Auxiliary (HAX), and the Goldstone radars. For debris sizes smaller than can be measured from ground sensors, NASA relies on examination of materials that have been exposed to the orbital space environment and other in situ measurements, e.g. Long Duration Exposure Facility (LDEF), solar arrays from the HST, the Orbital Debris Collector (ODC), and the Space Shuttles. Fig. 2.6 shows the coverage of the aforementioned methods used in the United States as function of altitude and particle size.[1] In addition to the various methods we have mentioned, space-based sensors and ground-based laboratory experiments (such as NASA DebriSat project) have also been used. Moreover, researchers have also utilized satellite laser ranging (SLR) which uses laser pulses to measure the distance to a satellite from a station to observe space debris. Advanced techniques that have been continuously improved over the years for precise orbital tracks of active satellites can be adapted further to improve the ranging precision and orbital predictions to aid in space situational awareness, maintaining object catalogs, debris remediation and conjunction assessment (*Shappirio et al.*, 2016).

In near Earth orbits as depicted in Fig. 2.1, space objects move in velocity of several km/s (around 7 km/s in LEO). At this hypervelocity speed, which translates to several thousands of km/h, even a small particle can damage, degrade, or destroy

---

[1]Note that there is a data gap around 1 mm size.

an expensive and fully functional spacecraft due to the very high velocities involved in a collision, on the average about 11 km/s (*NASA*, 2008). In case of large debris, what happened to Iridium 33 in February 2009 is a clear example; while in case of small particles, an example took place during the flight of STS-7 in 1983 when a paint fleck only 0.2 mm in size impacted the window and created a pit 0.4 mm deep, which exceeded the allowable damage criteria for reuse of the window outer pane during subsequent launches. The probability that debris will collide with a given spacecraft depends on the spacecraft's size and the debris flux through its orbital region (*National Research Council*, 1995). The effect of spacecraft size on the likelihood of being struck is simple; the chance of impact is directly proportional to the spacecraft's cross-sectional area relative to the debris flux and the amount of time exposed to the environment. The relationship between the probability of collision and the orbital region is far more complex, varying significantly with altitude and to a lesser degree with inclination. Although accidental collisions are relatively uncommon to date, but are expected to increase as more objects are placed into orbit (*NASA*, 2008).
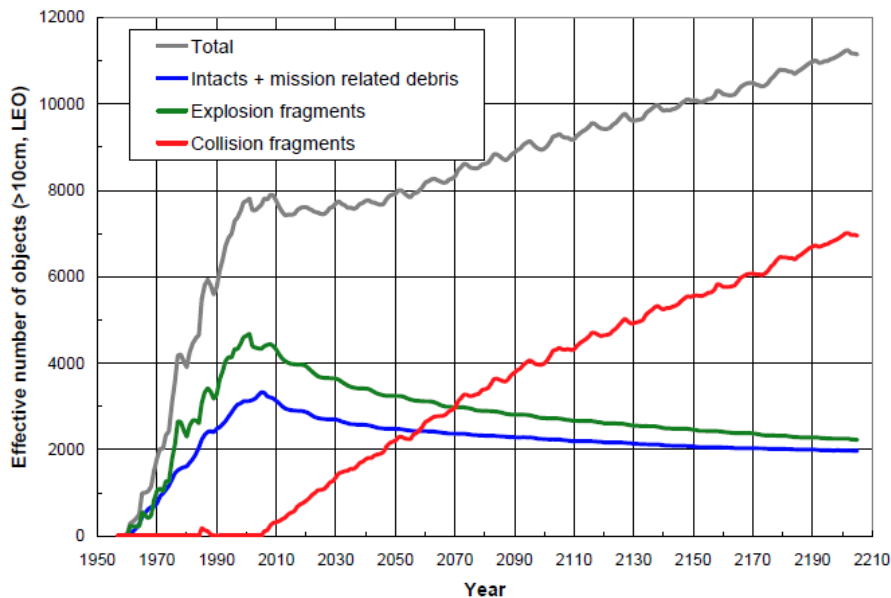
Figure 2.7.: Effective number of LEO objects, 10 cm and larger, from the LEGEND simulations based on the "no new launches" assumption (*NASA*, 2008).

Two methods have been identified to prevent space debris from further polluting our space environment and threaten the sustainability of outer space activity in the future. The first method is through the creation of a set of mitigation guidelines with a purpose to prevent the creation of new debris. This mitigation measures can be divided into two broad categories: 1) those that curtail the generation of potentially harmful space debris in the near term; and 2) those that limit their generation over the longer term (*UNOOSA*, 2010). The former involves the cur-

tailment of the production of mission-related debris and the avoidance of break-ups (e.g., through better spacecraft and rocket design; through commitment to avoid intentional destruction and other harmful activities). The latter concerns end-of-life disposal procedures that remove decommissioned spacecraft and launch vehicle orbital stages from regions populated by operational spacecraft. However, theoretical studies show that mitigation (prevention) alone is not sufficient to stabilize the space debris population in the future (*Liou and Johnson*, 2008). Even without further launches, the population will continue to increase (see Fig. 2.7) and eventually trigger a cascading effect of collision among RSOs which is called Kessler Syndrome (*Kessler and Cour-Palais*, 1978). Therefore, another method namely remediation (treatment) of the space debris population is proposed. Remediation, which is also called active debris removal (ADR), is performed by moving a selected (large) debris to a desired orbit (of little operational value) or bringing it back to Earth. To maintain the LEO population at a level comparable to the current environment requires a successful implementation of the commonly-adopted mitigation measures and a removal rate of about five objects per year (*Liou*, 2011).

While the mitigation measures have been around for about two decades, the remediation is still in its experimental phase. One of the commonly considered challenges that has to be overcome with this latter method is the uncooperative nature of the target debris. It is common for a large debris to tumble since it still possesses angular momentum left from its attitude control system when the failure occurred (*Nishida and Kawamoto*, 2011). Therefore, conducting an ADR mission to a debris object will be more difficult compared with a cooperative target. JAXA found that a tumbling object can still be captured only if its tumbling rate is below 30°/s as reported by *Shan et al.* (2016).

2.2. Rigid body dynamics

The motion of a satellite in space is a coupling between *translational* (orbital) and *rotational* motions. Therefore, describing the attitude motion of a satellite is only a part of the whole picture of describing its motion. However, since this study is about satellite attitude, this section will be confined only to describe about the rotational motion. In fact, much of attitude dynamics analysis can be performed by largely ignoring orbital effects (*Hughes*, 2004).

The attitude of a satellite is its orientation in space. The study of this motion is contained within the realm of satellite (or in general: spacecraft) attitude dynamics which is an applied science whose aim is to understand and predict how satellites (or spacecraft) orientation evolves (*Hughes*, 2004). For the purpose of the current study, the satellite structure will be considered as a *rigid body* which means that the distance between any two given points on the body remains constant in time (regardless of external forces or moments exerted on it). Moreover, a rigid body is usually considered as a continuous distribution of mass. Although a real satellite

is not rigid but some aspects of its observed behavior can be explained using the simplification.

2.2.1. Attitude representations

To study the attitude motion of a rigid body will require different coordinate systems and attitude representations (also called attitude parameterization). In three-dimensional space, two of the most common ways to represent the attitude of a rigid body are *Euler angles* and *quaternions* (with the former being the most popular). This section will describe those representations following the method given in (*Diebel*, 2006). Two different right-handed orthogonal coordinate systems will be used in order to discuss these attitude representations as illustrated in Fig. 2.8. They are a so called "world" coordinate system (x, y, z) or the *reference frame*, which is fixed in inertial space, and a body-fixed coordinate system (x', y', z') or the *spacecraft frame* (or *body frame* for short), which is rigidly connected to the object. Here, points and vectors in the body-fixed coordinate system are marked with a prime while those in the "world" coordinate system are not (e.g., $\boldsymbol{z}'$ is the vector expressed in the body-fixed coordinate system and $\boldsymbol{z}$ is the same vector expressed in the "world" coordinate system).
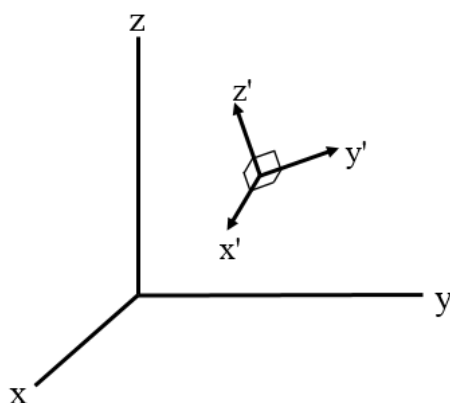
Figure 2.8.: Illustration of the world coordinate system (x, y, z) and the body-fixed coordinate system (x', y', z').

We will put the center of both coordinate systems at the center of mass of the object. The x-axis of the reference frame is pointing towards the vernal equinox, the z-axis in direction of the celestial North Pole and the y-axis is given by the cross product $\boldsymbol{z} \times \boldsymbol{x}$. Meanwhile, the coordinate axes of the spacecraft frame are pointing along the principle axes of inertia of the object.

Euler angles

In 18th century, the Swiss mathematician and physicist Euler[2] observed that the general displacement of a rigid body with one fixed point is a rotation about an axis through that point. This is called *Euler's rotation theorem*. The theorem requires that the displacement of a frame $\mathcal{F}_b$ with respect to another frame $\mathcal{F}_a$ be a rotation about some axis through their common origin as illustrated in Fig. 2.9. The associated angle and axis of this rotation are called Euler angle and Euler axis, respectively. This theorem forms the basis of what we will be discussing in the rest of this chapter.
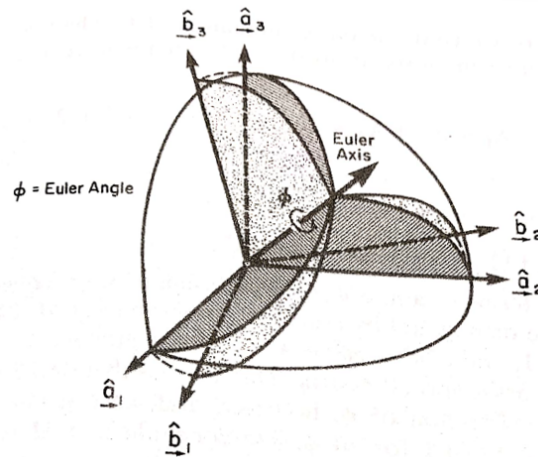
Figure 2.9.: Geometry pertaining to Euler's theorem (*Hughes*, 2004, Section 2.1).

Describing a rotation of a rigid body will involve matrix rotations. For this purpose, a concept of *rotation matrix* is required which is defined as a matrix whose multiplication with a vector rotates the vector while preserving its length (*Diebel*, 2006). All the rotation matrices (also called attitude matrices) in three dimensional space are represented by a *special orthogonal group* called $SO(3)$. Thus, if $R \in SO(3)$, then

$$\det R = \pm 1 \quad \text{and} \quad R^{-1} = R^T. \tag{2.1}$$

For our case, we only use rotation matrices which have determinant of $+1$ since that of other determinant will result in not rigid-body transformations.

We reference the elements of a rotation matrix as follows:

$$R = \begin{bmatrix} \boldsymbol{r}_1 & \boldsymbol{r}_2 & \boldsymbol{r}_3 \end{bmatrix} = \begin{bmatrix} r_{11} & r_{12} & r_{13} \\ r_{21} & r_{22} & r_{23} \\ r_{31} & r_{32} & r_{33} \end{bmatrix}. \tag{2.2}$$

---

[2]The full name is Leonhard Euler. Apart from mathematician and physicist, the world also recognized him as an astronomer, geographer, logician, and engineer.

The rotation matrix that encodes the attitude of a rigid body is the matrix that when pre-multiplied by a vector expressed in the world coordinates yields the same vector expressed in the body-fixed coordinates.[3] That is, if $\boldsymbol{z}$ is a vector in the world coordinates and $\boldsymbol{z}'$ is the same vector expressed in the body-fixed coordinates, then the following relations hold:

$$\boldsymbol{z}' = R\,\boldsymbol{z} \tag{2.3}$$

$$\boldsymbol{z} = R^T\,\boldsymbol{z}'. \tag{2.4}$$

We can also use rotation matrices to describe *coordinate rotations* which are rotations around a single coordinate axis. For a right-handed orthogonal system, with the x-, y- and z-axes enumerated by 1, 2, and 3, the respective coordinate rotations[4] R_1, R_2, and R_3 are

$$R_1(\alpha) = \begin{bmatrix} 1 & 0 & 0 \\ 0 & \cos(\alpha) & \sin(\alpha) \\ 0 & -\sin(\alpha) & \cos(\alpha) \end{bmatrix} \tag{2.5}$$

$$R_2(\alpha) = \begin{bmatrix} \cos(\alpha) & 0 & -\sin(\alpha) \\ 0 & 1 & 0 \\ \sin(\alpha) & 0 & \cos(\alpha) \end{bmatrix} \tag{2.6}$$

$$R_3(\alpha) = \begin{bmatrix} \cos(\alpha) & \sin(\alpha) & 0 \\ -\sin(\alpha) & \cos(\alpha) & 0 \\ 0 & 0 & 1 \end{bmatrix} \tag{2.7}$$

where α is the angle of rotation. A rotation matrix may also be referred to as a *direction cosines matrix* because the elements of this matrix are the cosines of the unsigned angles between the body-fixed axes and the world axes (*Diebel*, 2006).

Three coordinate rotations in sequence can describe any rotation in three dimensional space. But not all sequences (out of 27 possible sequences of three integers in $\{1, 2, 3\}$) that are able to span the space of all three-dimensional rotations. Only 12 satisfy the condition[5] in which two of the most common choices for the study of the attitude motion of a rigid body are the $(3, 1, 3)$ and $(1, 2, 3)$. Using our previous enumeration for the three axes, a rotation described by three successive coordinate

---

[3]In defining *the rotation matrix that encodes the attitude of a rigid body*, one can either write the matrix that maps from the body-fixed coordinates to the world coordinates or write the matrix that maps from the world coordinates to the body-fixed coordinates. Therefore, it is necessary to be sure that two different sources are using the same convention before using results from both sources together (*Diebel*, 2006).

[4]Also called *principal rotations* (*Hughes*, 2004).

[5]They should have no two consecutive numbers that are equal.

rotations, e.g., $R_3(\phi)$, $R_1(\theta)$, and $R_3(\psi)$ in case of $(3, 1, 3)$ sequence, is given by the three-dimensional *Euler angle vector* defined as

$$u := [\phi, \theta, \psi]^T, \tag{2.8}$$

where ϕ, θ, and ψ denote the respective angles of rotation.

The functions that maps the Euler angle vector to its corresponding rotation matrix and vice versa are

$$R_{313}(\phi, \theta, \psi) := R_3(\phi)R_1(\theta)R_3(\psi) \tag{2.9}$$

$$u_{313}(R) = \begin{bmatrix} \phi_{313}(R) \\ \theta_{313}(R) \\ \psi_{313}(R) \end{bmatrix} = \begin{bmatrix} \mathrm{atan2}(r_{13}, r_{23}) \\ \mathrm{acos}(r_{33}) \\ \mathrm{atan2}(r_{31,} - r_{32}) \end{bmatrix}. \tag{2.10}$$

While in case of $(1, 2, 3)$ sequence, the functions are

$$R_{123}(\phi, \theta, \psi) = R_1(\phi)R_2(\theta)R_3(\psi) \tag{2.11}$$

$$u_{123}(R) = \begin{bmatrix} \phi_{123}(R) \\ \theta_{123}(R) \\ \psi_{123}(R) \end{bmatrix} = \begin{bmatrix} \mathrm{atan2}(r_{23}, r_{33}) \\ -\mathrm{asin}(r_{13}) \\ \mathrm{atan2}(r_{12,} - r_{11}) \end{bmatrix}. \tag{2.12}$$

In the study of the gyroscopic motion of a spinning rigid body, the Euler angles, ϕ, θ, and ψ in $(3, 1, 3)$ sequence are known respectively as *spin*, *nutation*, and *precession*. One familiar example of gyroscopic motion is a spinning top where the body-fixed z-axis is aligned with the spin-axis of the top, and the body-fixed x- and y-axes point out the sides of the top. The tilt of the top away from the world z-axis is the nutation angle, and the moment arising from this tilt produces the familiar slow orbiting motion, called precession. Meanwhile, the angles associated with the sequence $(1, 2, 3)$ are sometimes called Cardan angles, Tait-Bryan angles,[6] or nautical angles. These angles are also commonly referred to simply as Euler angles in the aeronautics field, in which ϕ, θ, and ψ are known respectively as *roll*, *pitch*, and *yaw*, or, equivalently, *bank*, *attitude*, and *heading* (*Diebel*, 2006). Fig. 2.10 shows the sequences of the two representations.

In spite of being easy to understand and easy to use, Euler angle representations have mathematical singularities that are said to arise from *gimbal lock* (*Diebel*, 2006). It

---

[6]For Gerolamo Cardano, an Italian Renaissance mathematician, and for Peter Guthrie Tait, a 19th-century Scottish mathematical physicist, respectively.
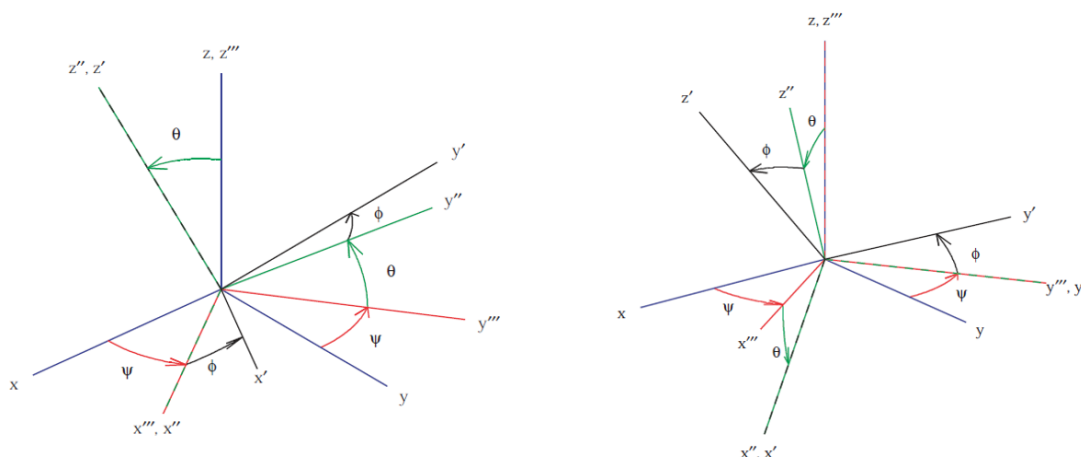
Figure 2.10.: Illustration of Euler angle in $(3, 1, 3)$ sequence (left image) and $(1, 2, 3)$ sequence (right image) as given in *Diebel* (2006).

comes from the indistinguishability of changes in the first and third Euler angles when the second Euler angle is at some critical value. In the case of the $(3, 1, 3)$ sequence, when the nutation angle $\theta = 0°$, changes in the spin angle (ϕ) are the same as changes in the precession angle (ψ). While in the $(1, 2, 3)$ sequence, when the pitch angle $\theta = 90°$, the vehicle is pointing straight up, and roll (ϕ) and yaw (ψ) are indistinguishable. As a result, Euler angles must be used with caution, especially in applications that deal with angles close to the singularity points. A common strategy for dealing with this problem is to change representations whenever an object nears a singularity.

Quaternions

To overcome the problem of Euler angles, we can use quaternions[7] (also called Euler symmetric parameters (*Wertz*, 1978)). Using unit quaternions to represent the attitude of an object will completely avoids the problem of gimbal lock. Other main advantage of using unit quaternions compared with Euler angles is that the representation is well-suited to integrate the angular velocity of a body over time, as the relevant functions are linear and have no singularities (*Diebel*, 2006). But on the other side, unit quaternions are not as easy to understand as Euler angles, because the four quaternion parameters do not have intuitive physical meanings like the former.

A quaternion can be represented by a vector of four components (*Wertz*, 1978):

$$\boldsymbol{q} \equiv [q_1, q_2, q_3, q_4]^T \equiv \begin{bmatrix} \mathbf{q} \\ q_4 \end{bmatrix} \tag{2.13}$$

---

[7]Were first devised by William Rowan Hamilton, a 19th-century Irish mathematician.

where

$$q_1 \equiv e_1 \sin \frac{\alpha}{2}, \ q_2 \equiv e_2 \sin \frac{\alpha}{2}, \ q_3 \equiv e_3 \sin \frac{\alpha}{2}, \ q_4 \equiv \cos \frac{\alpha}{2} \qquad (2.14)$$

with α is the angle of rotation and $\hat{\boldsymbol{e}} = (e_1, e_2, e_3)^{\mathrm{T}}$ is the unit vector along the rotation axis.

To represent an attitude in space, the four components should satisfy the unity norm constraint given by

$$\|\boldsymbol{q}\| = \sqrt{q_1^2 + q_2^2 + q_3^2 + q_4^2} = 1. \qquad (2.15)$$

Only quaternions with unity norm correspond to a pure rotation and can be used to represent the attitude of a rigid body through the following relations:

$$\boldsymbol{z}' = R_q(\boldsymbol{q}) \, \boldsymbol{z} \qquad (2.16)$$

$$\boldsymbol{z} = R_q(\boldsymbol{q})^T \, \boldsymbol{z}' \qquad (2.17)$$

where

$$R_q(\boldsymbol{q}) = \begin{bmatrix} q_1^2 - q_2^2 - q_3^2 + q_4^2 & 2(q_1 q_2 + q_3 q_4) & 2(q_1 q_3 - q_2 q_4) \\ 2(q_1 q_2 - q_3 q_4) & -q_1^2 + q_2^2 - q_3^2 + q_4^2 & 2(q_2 q_3 + q_1 q_4) \\ 2(q_1 q_3 + q_2 q_4) & 2(q_2 q_3 - q_1 q_4) & -q_1^2 - q_2^2 + q_3^2 + q_4^2 \end{bmatrix}. \qquad (2.18)$$

Similar with rotation matrices, sequences of rotations are represented by products of quaternions. That is, for unit quaternions $\boldsymbol{q}$ and $\boldsymbol{p}$, it holds that

$$R_q(\boldsymbol{q} \cdot \boldsymbol{p}) = R_q(\boldsymbol{q}) R_q(\boldsymbol{p}). \qquad (2.19)$$

Switching between different attitude representations is sometimes useful as each parameterization has its own advantages and disadvantages. For this purpose, the complete formulas for transformations between Euler angles and quaternions can be found in *Diebel* (2006).

2.2.2. Rigid body motion

Describing the motion of a rigid body in space requires two sets of equations of motion: the *kinematic equations of motion* and the *dynamic equations of motion* (*Wertz*, 1978). When using the kinematic equations of motion we describe the motion of a rigid body without reference to the causes of motion (i.e. forces). This is in contrast when we are using dynamic equations of motion where we always

consider the relationship between the motion and the forces affecting it. Both kinds of equations must be solved simultaneously.

Kinematic equations of motion

The kinematic equations of motion are a set of first-order differential equations specifying the time evolution of the attitude parameters. Each attitude representation has an associated set of kinematic equations of motion. However, this section will only consider the quaternion parameterization. Kinematic equations of motion for other attitude representations can be found in *Wertz* (1978).

Consider a rigid body with an embedded spacecraft coordinate frame (X, Y, Z) that rotates from time t to $t + \Delta t$ through a rotation axis represented by $\hat{\boldsymbol{e}} = (e_x, e_y, e_z)^{\mathrm{T}}$ with an angular velocity vector $\boldsymbol{\omega} = (\omega_x, \omega_y, \omega_z)^{\mathrm{T}} = \omega \hat{\boldsymbol{e}}$. If quaternion $\boldsymbol{q}$ represents the orientation of the rigid body with respect to the reference frame at time t then Eq. 2.13 can be used to derive its kinematic motion as

$$\frac{\mathrm{d}\boldsymbol{q}}{\mathrm{d}t} = \dot{\boldsymbol{q}} = \frac{1}{2}\Omega\boldsymbol{q} \tag{2.20}$$

where $\Omega = \begin{bmatrix} 0 & \omega_z & -\omega_y & \omega_x \\ -\omega_z & 0 & \omega_x & \omega_y \\ \omega_y & -\omega_x & 0 & \omega_x \\ -\omega_x & -\omega_y & -\omega_z & 0 \end{bmatrix}$.

If Ω is constant, Eq. 2.20 can be integrated to get

$$\boldsymbol{q}(t) = \exp\left(\frac{\Omega t}{2}\right)\boldsymbol{q}(0). \tag{2.21}$$

In case of $\hat{\boldsymbol{e}}$ is constant but ω varies, the integration can still be carried out to obtain

$$\boldsymbol{q}(t) = \exp\left(\frac{1}{2}\int_0^t \Omega(t')\mathrm{d}t'\right)\boldsymbol{q}(0) \tag{2.22}$$

where $t' = t + \Delta t$.

Dynamic equations of motion

The basic equation of attitude dynamics relates the time derivative of the angular momentum vector $\boldsymbol{L}$ to the applied torque $\boldsymbol{N}$ through the following equation *in inertial coordinates*

$$\frac{\mathrm{d}\boldsymbol{L}}{\mathrm{d}t} = \boldsymbol{N} \tag{2.23}$$

where $\boldsymbol{N} \equiv \sum_{i=1}^{n} \boldsymbol{r}_i \times \boldsymbol{F}_i$. Here $\boldsymbol{r}_i$ is the position of the ith point mass and $\boldsymbol{F}_i$ is the force applied to it.

However, since the moment of inertia tensor I of a rigid body[8] is most conveniently expressed along the body-fixed axes (*Wertz*, 1978), we will use the time derivatives of the components of $\boldsymbol{L}$ along these axes which is

$$\frac{\mathrm{d}\boldsymbol{L}}{\mathrm{d}t} = \boldsymbol{N} - \boldsymbol{\omega} \times \boldsymbol{L} = I\frac{\mathrm{d}\boldsymbol{\omega}}{\mathrm{d}t} \tag{2.24}$$

where $\boldsymbol{\omega}$ is the instantaneous angular velocity vector.

Eq. 2.24 is the fundamental equation of rigid body dynamics and is called *Euler's equation of motion*. This equation can be expressed in other forms which are

$$I\frac{\mathrm{d}\omega}{\mathrm{d}t} = \boldsymbol{N} - \boldsymbol{\omega} \times (I\boldsymbol{\omega}) \tag{2.25}$$

or

$$\frac{\mathrm{d}\boldsymbol{L}}{\mathrm{d}t} = \boldsymbol{N} - \left(I^{-1}\boldsymbol{L}\right) \times \boldsymbol{L}. \tag{2.26}$$

If the vector quantities are referred to the spacecraft frame (X, Y, Z) which is aligned with the principal axis of inertia[9] then Eq. 2.25 has the components:

$$\begin{aligned} I_x\dot{\omega}_x &= N_x + (I_y - I_z)\,\omega_y\omega_z \\ I_y\dot{\omega}_y &= N_y + (I_z - I_x)\,\omega_z\omega_x \\ I_z\dot{\omega}_z &= N_z + (I_x - I_y)\,\omega_x\omega_y \end{aligned} \tag{2.27}$$

---

[8]Moment of inertia tensor I is a quantity that determines the torque needed for a desired angular acceleration about a rotation axis. Moment of inertia depends on the body's mass distribution and the axis chosen. Larger moments require more torque to change the body's rate of rotation. I acts on $\boldsymbol{\omega}$ to give $\boldsymbol{L}$.

$\boldsymbol{L} = I\boldsymbol{\omega}$

$$\begin{bmatrix} L_x \\ L_y \\ L_z \end{bmatrix} = \begin{bmatrix} I_{xx} & I_{xy} & I_{xz} \\ I_{yx} & I_{yy} & I_{yz} \\ I_{zx} & I_{zy} & I_{zz} \end{bmatrix} \begin{bmatrix} \omega_x \\ \omega_y \\ \omega_z \end{bmatrix}$$

[9]Principal axis is any axis, $\hat{\boldsymbol{P}}$, such that the resulting angular momentum is parallel to $\hat{\boldsymbol{P}}$ when the spacecraft rotates about $\hat{\boldsymbol{P}}$. Any axis of symmetry is a principal axis. In addition, no matter how asymmetric an object is, it always has three mutually perpendicular principal axes defined by Eq. 2.29.

while Eq. 2.26 has the components:

$$
\begin{aligned}
\dot{L_x} &= N_x + \left(1/I_y - 1/I_z\right) L_y L_z \\
\dot{L_y} &= N_y + \left(1/I_z - 1/I_x\right) L_z L_x \\
\dot{L_z} &= N_z + \left(1/I_x - 1/I_y\right) L_x L_y
\end{aligned}
\tag{2.28}
$$

where $\dot{\boldsymbol{\omega}} = {\mathrm{d}\boldsymbol{\omega}}/{\mathrm{d}t}$ and $\dot{\boldsymbol{L}} = {\mathrm{d}\boldsymbol{L}}/{\mathrm{d}t}$.

Torque-free motion of a rigid spacecraft

Both the kinematic and the dynamics equations of motion must be solved simultaneously since, generally, the torque $\boldsymbol{N}$ depends on the spacecraft attitude.[10] One can employ numerical integration methods for this purpose or like what we are going to discuss now is to use analytical solutions which are available for limited cases.

If the applied torque $\boldsymbol{N}$ is independent of the attitude, the dynamics equations can be solved separately for the instantaneous angular velocity $\boldsymbol{\omega}$, which can then be used to solve the kinematic equations (*Wertz*, 1978, Section 16.2). In a special case where there is no applied torque or $\boldsymbol{N} = \boldsymbol{0}$, analytical solutions are available.

Take a look again at the Eq. 2.24. There, the presence of the $\boldsymbol{\omega} \times \boldsymbol{L}$ means that $\boldsymbol{L}$, and hence $\boldsymbol{\omega}$, is not constant in the spacecraft frame even if $\boldsymbol{N} = 0$. The resulting motion is called *nutation* which obviously will not happen if $\boldsymbol{\omega}$ and $\boldsymbol{L}$ are parallel. The latter occurs only if the rotation is about a principal axis of the rigid body; such is the case of *pure rotation*.[11] Therefore, for rotation about a principal axis, $\boldsymbol{L}$ is parallel to $\boldsymbol{\omega}$, or

$$
\boldsymbol{L} = I_p \boldsymbol{\omega} = I_p \omega \hat{\boldsymbol{P}}
\tag{2.29}
$$

where I_p is a constant of proportionality called the *principal moment of inertia* and $\hat{\boldsymbol{P}}$ is a principal axis. For a principal axis and a collection of masses, it holds that

$$
I_p = \sum_{i=1}^{n} m_i r_i^2
\tag{2.30}
$$

where r_i is the perpendicular distance of m_i from the principal axis.

---

[10]There are two kind of torque: internal torque and external torque. Internal torque is due to forces between individual points in a rigid body while external torque may come from two sources: 1) *disturbance torques* from environmental effects such as aerodynamic drag and solar radiation pressure; 2) deliberately applied *control torques* from devices such as gas jets or magnetic coils *Wertz* (1978).

[11]Pure rotation is also called uniform rotation while non-principal axis rotation is also called tumbling.

Fig. 2.11 shows the geometry of the two types of rotational motion we discussed in the previous paragraph. In pure rotation, rotation axis, a principal axis, a geometrical axis[12] are all parallel or anti parallel. In nutation, the instantaneous rotation axis is not aligned with a principal axis. In this case, the angular momentum vector, which remains fixed in space, will not be aligned with either the rotation axis or the principal axis. Both $\hat{\boldsymbol{P}}$ and $\boldsymbol{\omega}$ rotate about $\boldsymbol{L}$. $\hat{\boldsymbol{P}}$ is fixed in the spacecraft because it is defined by the spacecraft mass distribution irrespective of the object's overall orientation. Neither $\boldsymbol{L}$ nor $\boldsymbol{\omega}$ is fixed in the spacecraft. $\boldsymbol{\omega}$ rotates both in the spacecraft and in inertial space, while $\boldsymbol{L}$ rotates in the spacecraft but is fixed in inertial space. The angle between $\hat{\boldsymbol{P}}$ and $\boldsymbol{L}$ is a measure of the magnitude of the nutation, called the *nutation angle*, θ.
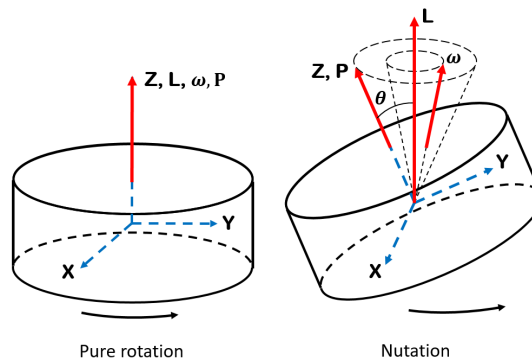
Figure 2.11.: Geometry of two types of rotational motion: pure rotation and nutation. $\boldsymbol{L}$ = angular momentum vector; $\boldsymbol{P}$ = principal axis; $\boldsymbol{\omega}$ = instantaneous rotation axis; $\boldsymbol{Z}$ = geometrical z axis.

A good approximation for many spacecraft which possess some degree of cylindrical symmetry is obtained when two of the three principal moment of inertia are equal $(I_x = I_y \neq I_z)$.[13] In this *axisymmetric case*, the angular momentum vector, $\boldsymbol{L}$, the instantaneous rotation axis, $\boldsymbol{\omega}$, and the $\hat{\boldsymbol{P}}_z$ principal axis are coplanar and the latter two axes rotate uniformly about $\boldsymbol{L}$. The body rotates at a constant velocity about the principal axis, $\hat{\boldsymbol{P}}_z$, as $\hat{\boldsymbol{P}}_z$ rotates about $\boldsymbol{L}$ and the nutation angle remains constant.[14]

The spacecraft *inertial spin rate*, $\boldsymbol{\omega}$, about the instantaneous rotation axis can be

---

[12]Geometrical axes are arbitrarily defined relative to the structure of the spacecraft itself. Thus, the geometrical z axis may be defined by some mark on the spacecraft or by an engineering drawing giving its position relative to the structure. This is the reference system which defines the orientation of attitude determination and control hardware and experiments *Wertz* (1978).

[13]Spacecrafts with this type of structure are also called gyroscopic bodies where rocket bodies which usually can be considered prolated cylinders, are good examples (*Koller*, 2016).

[14]Since $\hat{\boldsymbol{P}}_z$ is a spacecraft-fixed axis and is moving in inertial space, it cannot be the instantaneous rotation axis. *Wertz* (1978)

written in terms of components along $\hat{\boldsymbol{P}}_z$ and $\hat{\boldsymbol{L}}$ as

$$\boldsymbol{\omega} = \boldsymbol{\omega}_p + \boldsymbol{\omega}_l = \omega_p \hat{\boldsymbol{P}}_3 + \omega_l \hat{\boldsymbol{L}}_3 \tag{2.31}$$

where θ is the nutation angle, $\boldsymbol{\omega}_l$ is the *inertial nutation rate* which is the rotation of $\hat{\boldsymbol{P}}_z$ about $\boldsymbol{L}$ relative to an inertial frame of reference, and $\boldsymbol{\omega}_p$ is the *body nutation rate* which is the rotation rate of any point fixed in the body (e.g., a geometrical axis) about $\hat{\boldsymbol{P}}_z$ relative to the orientation of $\boldsymbol{L}$.

The amplitude of $\boldsymbol{\omega}$ is given by

$$\omega^2 = \omega_p^2 + \omega_l^2 + 2\omega_p \omega_l \cos\theta \tag{2.32}$$

The relation between the two components of angular velocity is given by

$$\omega_p = \frac{I_x - I_z}{I_y} \omega_l \cos\theta \tag{2.33}$$

If we denote the angle between $\hat{\boldsymbol{P}}_z$ and $\boldsymbol{\omega}$ as ϕ then it is given by

$$\tan\phi = \frac{\omega_l \sin\theta}{\omega_p + \omega_l \cos\theta} = \frac{I_z}{I_x}\tan\theta \tag{2.34}$$

Left side of Fig. 2.12 illustrates how, in inertial space, $\boldsymbol{\omega}$ rotates about $\boldsymbol{L}$ on a cone of half-cone angle $(\theta - \phi)$ called the *space cone*, for $I_x > I_z$. Meanwhile $\boldsymbol{\omega}$ maintains a fixed angle, ϕ, with $\hat{\boldsymbol{P}}_z$ and, therefore, rotates about $\hat{\boldsymbol{P}}_z$ on a cone called the *body cone*. Because $\boldsymbol{\omega}$ is the instantaneous rotation axis, the body is instantaneously at rest along the $\boldsymbol{\omega}$ axis as $\boldsymbol{\omega}$ moves about $\boldsymbol{L}$. Therefore, we may visualize the motion of the spacecraft as the body cone rolling without slipping on the space cone. The space cone is fixed in space and the body cone is fixed in the spacecraft. The left side of the figure is correct only for prolate objects, e.g. a tall cylinder. For oblate objects, e.g. a thin disk, where $I_z > I_x$, the space cone lies inside the body cone, as shown on the right side of the figure.

Asymmetric case which happens when all the components of the principal moment of inertia are different $(I_x \neq I_y \neq I_z)$ will be discussed in the next subsection.

2.2.3. Stability of rotation for a rigid body

Now we are going to use one of the component forms of Euler's equations (Eq. 2.27) to find conditions for stability[15] of rotation about any principal axis of a rigid

---

[15]The are various definitions of stability in the literature and by far the most successful is due to Liapunov. In simple terms, a solution to a differential equation is said to be *Liapunov stable* if the motion remains always within a specified upper bound. If the disturbances are small
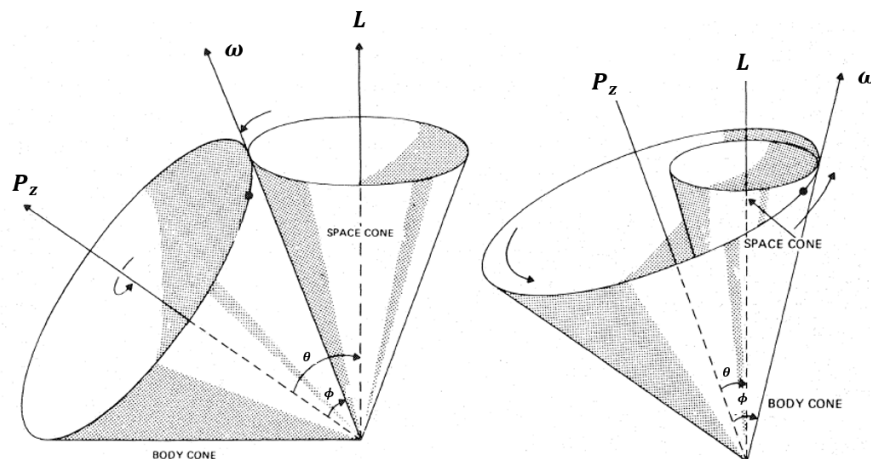
Figure 2.12.: Motion of nutating spacecraft. The body cone rolls on the space cone for $I_x = I_y > I_z$ (left). The body cone rolls on the space cone for $I_x = I_y < I_z$ (right). Images are taken from *Wertz* (1978) with modifications.

spacecraft. In contrast with our previous discussion, here we are considering an asymmetric body where $I_x \neq I_y \neq I_z$.

Let $\hat{\boldsymbol{P}}_z$ be the nominal spin axis, so that ω_x and ω_y are much smaller than ω_z. If the applied torques are negligible, then the right side of the third line of Eq. 2.27 is approximately zero, and ω_z is approximately constant. Taking the time derivative the first line of of Eq. 2.27, multiplying by I_2, and substituting the second line of Eq. 2.27 gives

$$
\begin{aligned}
I_x I_y \frac{\mathrm{d}^2 \omega_x}{\mathrm{d}t^2} &\simeq (I_y - I_z)\, I_y \frac{\mathrm{d}\omega_y}{\mathrm{d}t} \omega_z \\
&\simeq (I_y - I_z)\, (I_z - I_x)\, \omega_z^2 \omega_x
\end{aligned}
\tag{2.35}
$$

If $(I_y - I_z)\,(I_z - I_x) < 0$, then ω_x will be bounded and have sinusoidal time dependence with frequency $\sqrt{(I_y - I_z)\,(I_x - I_z)\,/\,(I_x I_y)}\,\omega_z$. However, if $(I_y - I_z)\,(I_z - I_x) > 0$, then ω_x will increase exponentially.

Therefore the motion is

- **stable** if I_z is either the largest or the smallest of the principal moments of inertia;

- **unstable** if I_z is the intermediate moment of inertia.

Eq. 2.35 only establishes the stability over short time intervals. Over longer time intervals, energy dissipation effects (will be discussed in the next section) cause

---

enough then the disturbed motion will always stay within an arbitrarily low bound (*Hughes*, 2004).

rotational motion about the axis of smallest moment of inertia to be unstable, too.

Internal torques do not change the value of the angular momentum in inertial space but they can affect the behavior of $\boldsymbol{L}$ in spacecraft frame. Additionally, if the internal forces between the components of a spacecraft lead to *energy dissipation* (e.g. through solid or viscous friction or magnetic eddy currents) the rotational kinetic energy of the spacecraft will decrease. Regarding external torques, for a spacecraft which is initially spinning about a principal axis, a torque applied parallel or anti-parallel to the angular momentum vector, $\boldsymbol{L}$, will cause an increase or a decrease in the magnitude of $\boldsymbol{L}$ without affecting its direction. On the other hand, a torque component perpendicular to $\boldsymbol{L}$, will cause the direction of $\boldsymbol{L}$ to change without altering its magnitude (*Wertz*, 1978). The change in direction of the angular momentum vector due to an applied torque is called *precession*.

We are going to explain what happens to the rotational motion in the present of applied torques. But first, we consider the condition in the absence of torques (in this case due to energy dissipation) where the components of $\boldsymbol{L}$ in inertial space are constant. However, the components of $\boldsymbol{L}$ in spacecraft frame are time dependent although its magnitude is constant. Let us use the concept of the *angular momentum sphere* and the *energy ellipsoid*. The locus of points in angular momentum space corresponding to a fixed magnitude, L, is just a sphere of radius L which is the angular momentum sphere as shown in Fig. 2.13. The locus of possible values of L *in the spacecraft frame* is the intersection of the angular momentum sphere and the energy ellipsoid which satisfies the equation

$$\frac{L_x^2}{2I_x E_k} + \frac{L_y^2}{2I_y E_k} + \frac{L_z^2}{2I_z E_k} = 1 \tag{2.36}$$

where E_k is the rotational kinetic energy of a rigid spacecraft.

Fig. 2.13 can be used to explain the stability of motion for asymmetric body without applied torques as we have discussed before. As we can see in the figure, the loci in the neighborhood of the principal axes of largest and smallest moment of inertia (which are P_x and P_z, respectively) are elliptical closed curves which means they are stable, but the loci passing near the third principal axis (P_y) go completely around the angular momentum sphere which means they are unstable. The figure can also be used to explain the case of axisymmetric body ($I_x = I_y < I_z$ and $I_x = I_y > I_z$). For this case, the locus of possible values of angular momentum consists of two circles about P_z which means they are stable. The angular momentum vector in the spacecraft frame moves at a constant rate along one of the circles which denotes a nutation.

When there is a presence of dissipative forces with axial symmetry, the energy ellipsoid will shrink in size while maintaining its shape. On the other side, the angular momentum sphere is unchanged. This will make the circles described by the intersection between the energy ellipsoid and the angular momentum sphere (which indicates the allowed position of the angular momentum vector) are shrinking
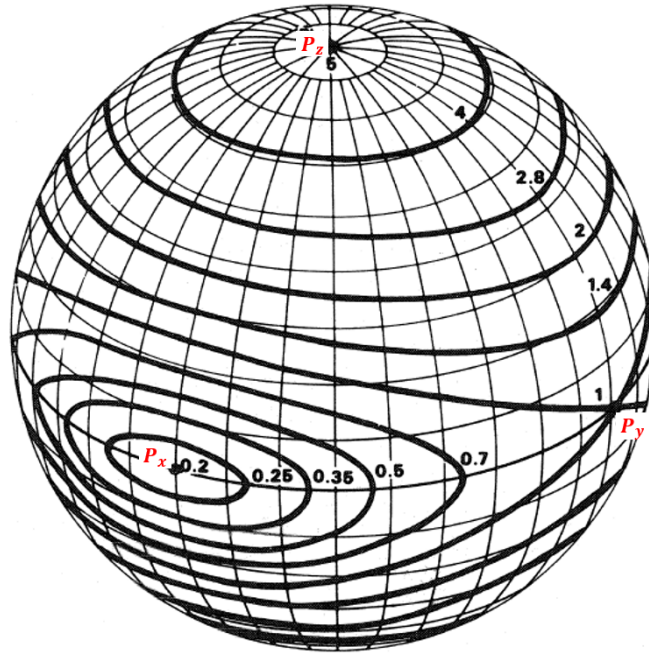
Figure 2.13.: Family of intersections of energy ellipsoid and angular momentum sphere for various energies, with $I_x : I_y : I_z$ in the ratio $25 : 5 : 1$. Each curve is labeled with its value of $2I_y E_k/L^2$. P_x, P_y, and P_z are the principal axes with P_x as the major principal axis. Image is taken from *Wertz* (1978) with modifications.

too. The vector will describe a spiral trajectory as it continues to rotate along the intersection of the shrinking energy ellipsoid and the angular momentum sphere. The shrinking of the energy ellipsoid continues until it lies wholly within, or is tangent to, the angular momentum sphere. For $I_x = I_y < I_z$, this results in $\boldsymbol{L}$ being aligned along the positive or negative P_z. For $I_x = I_y > I_z$, the limit occurs when $\boldsymbol{L}$ lies on the circle $L_x^2 + L_y^2 = L^2$, $L_z = 0$ and it will remain fixed at a point on this circle. Thus, in both cases nutation ceases, and the motion of the body is simple rotation about a fixed axis.

In the case there is no axis of symmetry, the intersections of the energy ellipsoid and the angular momentum sphere are not circles as can be seen in Fig. 2.13. When energy dissipation ceases, the angular momentum vector becomes aligned with the *major principal axis* (the axis corresponding to the largest principal moment of inertia). This will make the rotational kinetic energy minimized. Essentially, if the nominal spacecraft spin axis is the major principal axis, nutation represents excess kinetic energy above that required by the magnitude of the angular momentum. The reduction of this excess kinetic energy and the corresponding alignment of the rotation axis with the principal axis of largest moment of inertia that we have seen is known as *nutation damping*.

If the nominal spacecraft spin axis as we discussed in the previous paragraph is a

principal axis other than the major principal axis, energy dissipation will result in an *increase* in nutation. Eventually, the motion when the energy dissipation ceases is pure rotation about an axis perpendicular to the nominal spin axis, a condition known as *flat spin* where the spacecraft now rotates around the major principal axis. Fig. 29 demonstrates an example of this transition with a prolated cylinder (e.g., a rocket body) which is considered as a rigid body with $I_x = I_y = 1.0 \, \text{kg} \cdot \text{m}^2$ and $I_z = 1.2 \, \text{kg} \cdot \text{m}^2$. It has an initial rotation around the principle axis of minimum inertia (X-axis) with a small deflection in the z-component: $\omega = (10, \, 0, \, 0.1)$. On the left side of the figure we can see that the angular velocity component ω_x is evolving from 10 to 0 rad/sec within about one minute while, in the same time, ω_z is increasing from 0 to a constant value of 8.33 rad/sec. While on the right side of the figure we can see how the angular momentum is transferred on a spiral trajectory starting from a pure rotation around the X-axis ($L_x = 10 \, \text{rad} \cdot \text{kg} \cdot \text{m}^2/\text{s}$) towards a pure rotation around the Z-axis ($L_z = 10 \, \text{rad} \cdot \text{kg} \cdot \text{m}^2/\text{s}$).
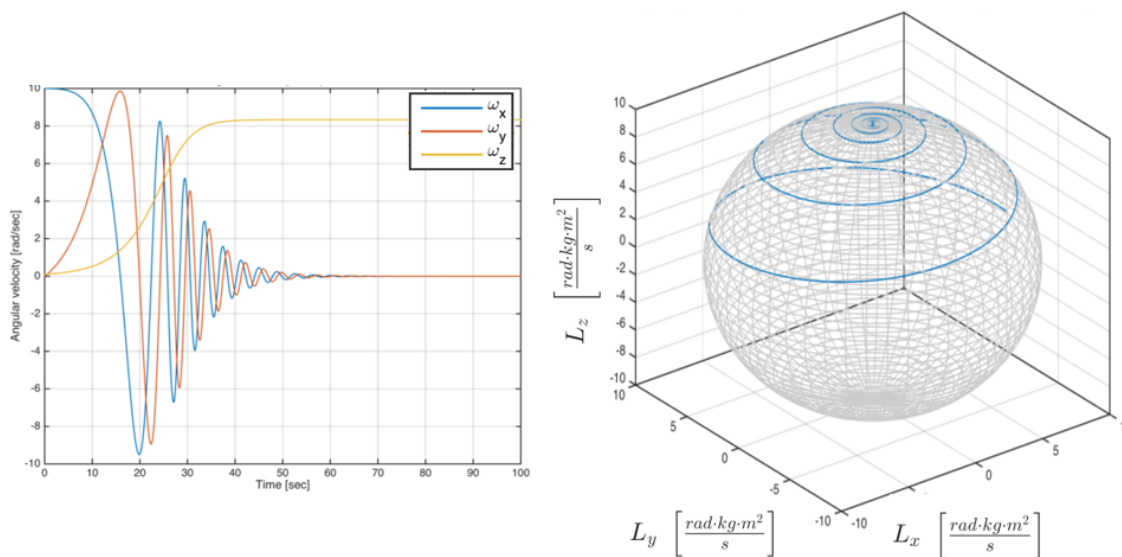
Figure 2.14.: Transfer of the angular momentum from the nominal principle axis of minimum inertia (x-axis) to that of maximum inertia (z-axis) demonstrated using angular velocity (left) and using angular momentum sphere (right) (*Koller*, 2016).

2.3. Torques acting on spacecraft

In this section we are going to describe the torques that are typically encountered by spacecraft. Their origins can come either from outside the spacecraft or from the spacecraft itself. The former is called *external torques* while the latter is called *internal torques*. External torques comes from the interaction of a spacecraft with

space environment which is called environmental torques (also disturbance torques) or from deliberately applied control torques from devices such as gas jets or magnetic coils. Internal torques, on the other hand, are in a sense self-generated (*Hughes*, 2004). Although spacecraft torques is very small in terms of familiar terrestrial experience, models of the disturbance torques acting on the spacecraft are required for an accurate attitude prediction. This is because their cumulative effects after sufficiently long periods may be significant. In this section we will describe most of the torques other than the ones which are deliberately applied.

2.3.1. Environmental torques

Environmental torques are a common source of *attitude drift* which is a special case of slow precession. This is due to a small applied torque which means that the magnitude of the integral of the torque over a spin period is much less than $|\boldsymbol{L}|$ (*Wertz*, 1978). To be able to calculate the effect of external torques to a spacecraft, we need to numerically integrate Euler's equations in which the torques must be modeled as a function of time and the spacecraft's position and attitude (*Wertz*, 1978, Section 17.2). Fig. 2.15 shows a typical comparison of external torques for Earth orbits. It consists of the four dominant sources which are the Earth's gravitational and magnetic fields, solar radiation pressure, and aerodynamics drag. Each of these torques will be discussed in this section. Torques due to meteoroidal and space debris impact also come from space environment but are not covered in this section.

Gravity- gradient torque

This torque arises due to different gravitational field over a material body which prevents the center of mass as the center of gravity. This results in a gravitational torque about the body mass center. Following the explanation given in *Hughes* (2004), one can derive the total gravitational force and the torque which are applied to a body, not necessarily rigid, immersed in a gravitational field. However, multiple integrations embedded in the equations make analytical progress almost impossible without further assumptions. Listed below are four assumptions which greatly simplify the gravitational-torque expressions while in mean time are also excellent assumptions for most spacecraft situations. Fig. 2.16 illustrates the assumptions.

1. Only one celestial primary needs to be considered.

2. The primary possesses a spherically symmetrical mass distributions.

3. The spacecraft is small compared to its distance from the mass center of the primary.

4. The spacecraft consists of a single body.
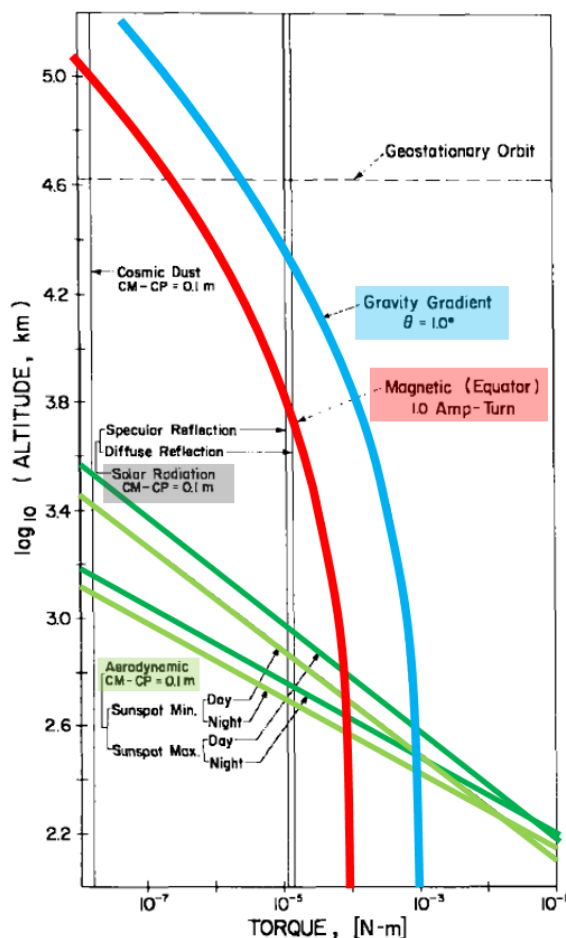
Figure 2.15.: Comparison of several common torques on a typical spacecraft, vs. altitude. Image is taken from *Hughes* (2004) with modifications.

The above assumptions permit simple expressions for the total gravitational force $\boldsymbol{F}$ and the total gravitational torque $\boldsymbol{N}_c$ (about the mass center) on spacecraft to be derived which are

$$\boldsymbol{F} = -\mu \int_{\mathscr{B}} \frac{\boldsymbol{R}\,dm}{\boldsymbol{R}^3} \tag{2.37}$$

$$\boldsymbol{N}_c = -\mu \int_{\mathscr{B}} \frac{\boldsymbol{r} \times \boldsymbol{R}}{R^3} dm \tag{2.38}$$

and

$$\boldsymbol{R} = \boldsymbol{R}_c + \boldsymbol{r}. \tag{2.39}$$

where $\boldsymbol{R}_c$ is the location of the mass center of $\mathscr{B}$ (spacecraft) with respect to the
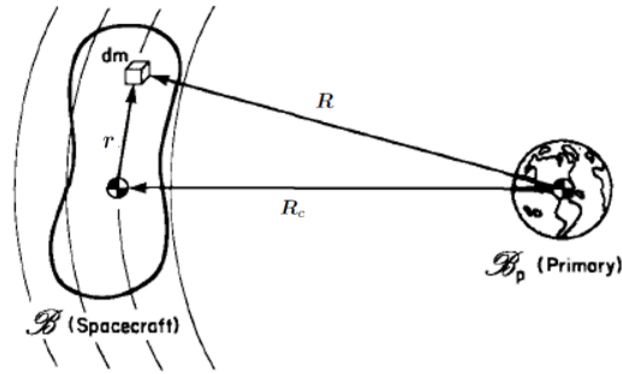
Figure 2.16.: Spacecraft in the gravitational field of one inertially spherical primary.

mass center of $\mathscr{B}_p$ (primary), $\boldsymbol{r}$ locates the mass element dm with respect to the mass center. For Earth, $\mu = 3.986 \times 10^{14}\,\mathrm{N \cdot m^2/kg}$.

Interested readers can find the description when each of the previous assumptions are removed in *Hughes* (2004).

Magnetic Disturbance torque

This torque results from the interaction between the spacecraft's residual magnetic field and the geomagnetic field (*Wertz*, 1978). Its primary sources are spacecraft magnetic moments, eddy currents, and hysteresis (the irreversible magnetization of permeable material) with the first one usually being the dominant source.

The instantaneous magnetic disturbance torque, $\boldsymbol{N}_{\mathrm{mag}}$ (in $\mathrm{N \cdot m}$), due to the spacecraft effective magnetic moment $\boldsymbol{m}$ (in $\mathrm{A \cdot m^2}$) is given by

$$\boldsymbol{N}_{\mathrm{mag}} = \boldsymbol{m} \times \boldsymbol{B} \tag{2.40}$$

where $\boldsymbol{B}$ is the geocentric magnetic flux density (in $\mathrm{Wb/m^2}$) and $\boldsymbol{m}$ is the sum of the individual magnetic moments caused by permanent and induced magnetism and the spacecraft-generated current loops.

The torques caused by the induced eddy currents and hysteresis are due to the spinning motion of the spacecraft. A study has shown that the eddy currents produce a torque which precesses the spin axis and also causes an exponential decay of the spin rate. This torque is given by

$$\boldsymbol{N}_{\mathrm{eddy}} = k_e(\omega \times \boldsymbol{B}) \times \boldsymbol{B} \tag{2.41}$$

where ω is the spacecraft's angular velocity vector and k_e is a constant coefficient which depends on the spacecraft geometry and conductivity. Eddy currents are

appreciable only in structural material that has a permeability nearly equal to that of free space.

The hysteresis effects are appreciable only in very elongated "soft" magnetic material (i.e., materials for which changes in the ambient field cause large changes in the magnetic moment). The torque due to the hysteresis is given by

$$\boldsymbol{N}_{\mathrm{hyst}} = \frac{\omega}{\omega^2}\frac{\Delta E_H}{\Delta t} \tag{2.42}$$

$$\Delta E_H = V \oint \boldsymbol{H} \cdot \mathrm{d}\boldsymbol{B}$$

where Δt is the time over which the torque is being evaluated, V is the volume of the permeable material, $\boldsymbol{H}$ is the magnetic field, and $\mathrm{d}\boldsymbol{B}$ is the induced magnetic induction flux in the material.

Solar radiation torque

Solar radiation is the dominant source of electromagnetic radiation in the Earth's vicinity.[16] When it intercepts a spacecraft's surface, the momentum flux carried out by the photons will exert a corresponding pressure. If the resulting force is not aligned with the body center of mass, a torque will be created. The radiation pressure or force per unit area equals to the vector difference between the incident and reflected momentum flux (*Wertz*, 1978). There are three major factors determining the radiation torque on a spacecraft which are (1) the intensity and spectral distribution of the incident radiation, (2) the geometry of the surface and its optical properties, and (3) the orientation of the Sun vector relative to the spacecraft (*Wertz*, 1978). As can be seen in Fig. 2.15, the solar radiation pressure is essentially altitude independent for spacecraft in Earth orbit.

The mean momentum flux, P, acting on a surface normal to the solar radiation, is given by

$$P = \frac{F_e}{c} \tag{2.43}$$

where F_e is the solar constant[17] and c is the speed of light.

Usually, we can model the forces adequately by assuming that incident radiation is either *absorbed*, *reflected specularly*, *reflected diffusely*, or some combination of these

---

[16]Other sources of electromagnetic radiation pressure are solar radiation reflected by the Earth and its atmosphere (the Earth's albedo), ion emitted from the Earth and its atmosphere (Earth radiation), and the solar wind.

[17]$F_e = \frac{1356}{1.0004+0.0334\cos D}$ W/m^2 where D is the "phase" of year, measured from July 4, the day of Earth aphelion (*Wertz*, 1978).
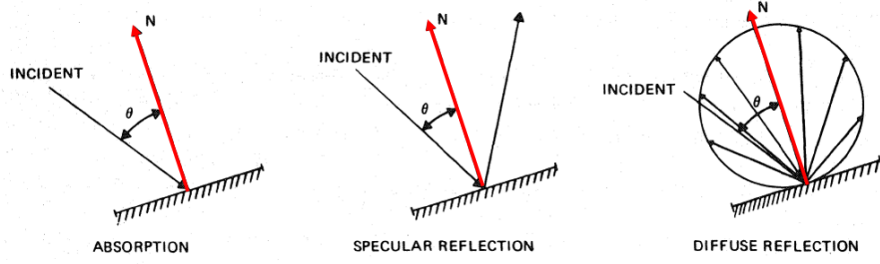
Figure 2.17.: Absorption and Reflection of Incident Radiation. (*Wertz*, 1978).

(see Fig. 2.17). If the momentum flux, P, is incident on an elemental area $\mathrm{d}A$ with unit outward normal $\hat{N}$, then we can find the general expression for the solar radiation torque, $\boldsymbol{N}_{\mathrm{solar}}$, acting on a spacecraft as

$$\boldsymbol{N}_{\mathrm{solar}} = \int \boldsymbol{R} \times \mathrm{d}\boldsymbol{f}_{\mathrm{total}} \tag{2.44}$$

where $\boldsymbol{R}$ is the vector from the spacecraft's center of mass to the elemental area $\mathrm{d}A$, $\mathrm{d}\boldsymbol{f}_{\mathrm{total}}$ is the total differential radiation force (momentum transferred per unit time) given by

$$\mathrm{d}\boldsymbol{f}_{\mathrm{total}} = -P \int \left[(1 - C_s)\, \hat{\boldsymbol{S}} + 2\left(C_s \cos\theta + \tfrac{1}{3} C_d \right) \hat{\boldsymbol{N}} \right] \cos\theta \, \mathrm{d}A \tag{2.45}$$

and the integral is over the spacecraft's irradiated surface.

In Eq. 2.45, C_a is the *absorption coefficient*, C_s is the *coefficient of specular reflection* (the fraction of the incident radiation that is specularly reflected), C_d is the *coefficient of diffuse reflection* (the fraction of the incident radiation that is diffusely reflected), $\hat{\boldsymbol{S}}$ is the unit vector from the spacecraft to the Sun, and θ is the angle between $\hat{\boldsymbol{S}}$ and $\hat{\boldsymbol{N}}$. In this equation it is assumed that absorption, specular reflection, and diffuse reflection all play a part (without any transmission) such that $C_a + C_s + C_d = 1$ (*Wertz*, 1978).

To simplify the calculation of Eq. 2.44, the spacecraft configuration is frequently approximated by a collection of simple geometrical elements such as plane, cylinder, or sphere. Using this approach, the solar radiation torque can be calculated as

$$\boldsymbol{N}_{\mathrm{solar}} = \sum_{i=1}^{n} \boldsymbol{R}_i \times \boldsymbol{F}_i \tag{2.46}$$

where $\boldsymbol{R}_i$ is the vector from the spacecraft center of mass to the center of pressure of the ith element, $\boldsymbol{F}_i$ is the solar radiation force on each element which is calculated by

$$\boldsymbol{F}_i = \int \mathrm{d}\boldsymbol{f}_{\mathrm{total,\,i}}. \tag{2.47}$$

During its orbital life, one part of a spacecraft can cast shadows on another. This phenomenon, which is usually called *self shadows*, reduces the total of solar radiation torques and also shifts the *center of pressure*[18], r_{cp}, which can be obtained from

$$\int r \times \mathrm{d}f = r_{cp} \times F. \tag{2.48}$$

The extent of shadowing is a function of the geometrical design of the spacecraft and the incident Sun angle (*Wertz*, 1978).

Aerodynamic torque

The aerodynamic torque is the dominant environmental disturbance torque for spacecraft below approximately 400 km as can be seen in Fig. 2.15. This is due to the interaction of the upper atmosphere with a satellite's surface which produces a torque about the center of mass (*Wertz*, 1978).

By modeling as if the incident particles lose their entire energy on collision, the aerodynamic torque can be found as

$$
\begin{aligned}
N_{\mathrm{aero}} &= \frac{1}{2}C_D\rho V_0^2 \int \left(\hat{N} \cdot \hat{V}_0\right)\left(\hat{V}_0 \times r_s\right)\mathrm{d}A \\
&\quad + \frac{1}{2}C_D\rho V_0 \int \left\{\hat{N} \cdot (\omega \times r_s)\left(\hat{V}_0 \times r_s\right)\right. \\
&\quad \left. + \left(\hat{N} \cdot \hat{V}_0\right)\left[(\omega \times r_s) \times r_s\right]\right\}\mathrm{d}A
\end{aligned}
\tag{2.49}
$$

where C_D is the drag coefficient, ρ is atmospheric density, V_0 is the velocity of the center of mass relative to the atmosphere, $\mathrm{d}A$ is surface element, $\hat{N}$ is outward normal of the surface element, r_s is the vector from the spacecraft's center of mass to the surface element, ω is angular velocity of the spacecraft, and $\hat{V}$ is the unit vector in the direction of the translational velocity, V, of the surface element relative to the incident stream. The first term in Eq. 2.49 is the torque due to the displacement of the spacecraft's center of pressure from the center of mass. The second term is the dissipation torque due to the spacecraft spin. For a spacecraft in Earth orbit with $\omega r \ll V_0$ the second term is approximately four orders of magnitude smaller than the first and may be neglected.

Shadowing of one part of the spacecraft by another must also be considered in the torque evaluation.

---

[18]Center of pressure is located at the intersection of the line of action of the single force which replaces the resultant radiation force and the plane passing through the center of mass of the spacecraft perpendicular to the line of action.

2.3.2. Internal torques

Internal torques are defined as torques exerted on the main body of a spacecraft by such internal moving parts (*Wertz*, 1978). These could be many things like reaction wheels, flexible booms or solar arrays, scanning or rastering instruments, tape recorder reels, liquids inside partially filled tanks, or astronauts inside a manned space station. In the absence of external torques, the total angular momentum of a spacecraft remains constant. However, internal torques can alter the system's kinetic energy and redistribute the spacecraft's angular momentum among its component parts in ways which can change its dynamic characteristics as has been discussed in Section 2.2.3.

Mass Expulsion Torques

Whenever mass is ejected from a spacecraft, the resulted disturbance torques (which can degrade the control system performance) lead to premature fuel depletion, or cause mission failure. Three design considerations are important in dealing with mass expulsion torques: 1) identification of the sources and assessment of the torque magnitudes; 2) determination of acceptable magnitudes; and 3) control over design and development to ensure that the acceptable magnitudes will not be exceeded. This torque can be grouped into two major categories according to the nature of their sources: 1) unintentional control system torques and 2) torques resulting from sources intended to expel mass.

Propellant slosh loads

Propellant sloshing refers to free surface oscillations of a fluid in a partially filled tank resulting from translational or angular acceleration of the spacecraft. It could be a result from an attitude or orbit control system, elastic deformation of the vehicle, or an environmental disturbance. Once sloshing begins, it may persist for a long time due to the small damping effects of the tank walls unless damping devices, such as baffles, are provided. Propellant sloshing can result in attitude precession or nutation, spacecraft instability, or damage to the propellant tank. The extent of propellant sloshing and the consequent forces on the spacecraft depend on the tank geometry, propellant properties, the effective damping, the height of the propellant in the tank, the acceleration field, and the perturbing motion of the tank.

Crew and internal hardware motions

The effects of crew movements inside a spacecraft can be assumed to be directly proportional to the amplitude of the motion and the ratio of the human's mass to the spacecraft moment of inertia. Regarding internal hardware components, their

motion onboard a space vehicle is normally compensated for, such that the main body experiences no torques. For simple cases, in principle, every rotor can be balanced by an identical rotor moving in the opposite direction.

Studies to understand the effects of crew and internal hardware motions have been conducted using a deterministic or probabilistic approach. One of the results is that an astronaut could rock a space station and cause it to tumble if the period of his motion is in the neighborhood of certain integral multiples of half the space station's spin period. Other result shows that when an astronaut executes a closed path motion onboard a space vehicle, the total angular momentum does not necessarily return to its original value in spacecraft coordinates.

2.4. Attitude studies of inactive satellites

Attitude studies of inactive satellites or space debris can be performed using various instruments and techniques. Some of those which are relevant with this study will be discussed in this section.

Silha et al. (2017) presented a progress report from a collaborative campaign of four priority targets observed with radar, SLR and light curves in order to test and validate a tool named iOTA which was developed as part of an ESA project "Debris Attitude Motion Measurements and Modeling".[19] The validation was conducted by comparing generated synthetic measurements from iOTA's post-processing modules with real measurements obtained from three sensors of different techniques: ZIMLAT optical telescope in Switzerland, TIRA radar in Germany, and Graz SLR station in Austria. The authors selected four defunct satellites which are ENVISAT, ERS 1, ERS 2, and ADEOS 2, and one upper stage which is H-2A R/B. ISAR (Inverse Synthetic Aperture Radar) images have been acquired by TIRA system along with the light curves acquired by ZIMLAT telescope. SLR residuals were able to be measured only for ENVISAT. Analysis of ISAR images have been performed to determine the attitude states of all the targets. Attitude states could be found for ENVISAT, ERS 1 and ERS 2 but not ADEOS 2 which shows quite a tumbling behavior (also observed in the light curves).

Pittet et al. (2018) presented the spin motion determination of ENVISAT which is a non-active satellite equipped with laser retroreflector arrays (LRA) determined from SLR data acquired by a single station which is the Zimmerwald Observatory in Switzerland.[20] The authors selected 31 passes obtained between April 2013 and November 2015 using point-like model and determined parameters describing the orientation of the angular velocity vector $\boldsymbol{\omega}$ both in the inertial and in the body-fixed reference frame for each pass. The authors found that the configuration between

---

[19]We used iOTA in the modeling part of this study in Section 4.2.

[20]The complete name of the observatory is Swiss Optical Ground Station and Geodynamics Observatory Zimmerwald (SwissOGS).

ω and the satellite's orbital plane, seems to be stable during the analyzed period. This is also the case with the angle between the LRA position vector and ω which suggests that the spin axis was aligned with the satellite's principal axis of inertia. They also found that the spin motion of ENVISAT is retrograde and its rotation period is slowly increasing. Basically, the work has shown that SLR can be used to extract a complete information about the spin motion of an object equipped with a LRA within a single pass.

Studies which specifically use spin period evolution (such as this study) have been around since many years ago. *Pontieu* (1997) reported a preliminary study of tumbling period evolutions for discarded third stages. For this purpose, he used data of flashes from a database called Photometric Periods of Artificial Satellites (PPAS) which contains almost 40,000 measurements of spin periods of over 1,300 different objects which include payloads, rocket bodies, and smaller space debris. The observations were conducted between 1962 until 1997 by 140 amateur satellite observers using naked eyes or binoculars. As a result, the author found several non-typical evolutions (e.g., sudden jumps in the tumbling period) of some discarded third stages that can probably be resulted from their collision with space debris. Later, *Papushev et al.* (2009) used a fast photoelectric photometer attached to an optical telescope to analyze the periods and light curves of several uncontrolled artificial satellites. The observation was conducted in 1995–2003 at Sayan Solar Observatory (SSO) in Russia using standard photometric Johnson-Morgan UBVR system. After inspecting spin period evolutions from a number of inactive RADUGA, GORIZONT, and EKRAN satellites, the authors found that some satellites demonstrate spasmodic period change. After having practically constant periods over the long-term observation period, some objects show sharp increase of their period and its subsequent decrease down to initial value. Specifically to RADUGA-14, they found that their light curves exhibited broad features adjacent to features that were thin, sharp, and tall. They attributed the tall, sharp features to specular sunlight reflections (glints) from the large-area solar panels.

Albuja et al. (2015) used the Yarkovsky-O'Keefe-Radzievskii-Paddack (YORP) effect[21] to simulate the observed rotation rates of several GEO satellites. As the background of the research, the authors noticed that observational data of defunct satellites obtained from previous studies shows that rotational period of defunct GEO satellites can vary in time and fast spin rates are often detected. Moreover, observational data shows that some objects experience an interchanging between increasing and decreasing in rotational period. Other observations have a complex light curve from which it is difficult to extract the periodicity as the light curve is

---

[21] The YORP effect is a torque that is created as a result sunlight being reflected or thermal energy being reemitted from the surface of an asymmetric body. The body must have a shape like a propeller for the case of reflection or a certain amount of "windmill" asymmetry for the case of reemission *Rubincam* (2000). This effect is credited for the observed secular change in angular velocity of various asteroids smaller than 10 km, including 54509 YORP (2000 PH5), (1862) Apollo, (1620) Geographos, (3103) Eger and (25143) Itokawa (*Albuja et al.*, 2018).

rapidly changing. Even more, some observations prove difficult to distinguish the true rotation period of the satellite due to symmetry and optical properties. They also noticed through the work of *Ojakangas and Hill* (2011), who analyzed the effects of YORP on small Earth orbiting objects, that solar radiation pressure has a strong effect on the angular momentum of a small Earth orbiting object, leading to a complex, tumbling rotation. Therefore, the purpose of the study is to introduce the theory of the YORP effect in the context of inactive (large) satellites and to understand if this effect could have an observable secular effect on the rotational dynamics of defunct satellites found in Earth orbit.

In their study, *Albuja et al.* (2015) used the YORP theory to obtain an order of magnitude estimate of the evolution of angular velocity and obliquity (equivalently the solar inclination) for a defunct satellite *solely as a result of YORP*. The results obtained with the theory, using both the spin averaged and the year averaged dynamics, are compared to numerical simulations using high-fidelity 6 degree of freedom (DOF) for consistency and with observational data for validation. For the simulation, they used 3D models which are based on two satellite configurations, i.e., BOEING 376 and GORIZONT (Fig. 2.18). The center of mass of the model is adjusted to have significant YORP coefficients due to the geometrical asymmetry. It is also assumed that the body is uniformly rotating about its maximum moment of inertia and it moves in Earth orbit (instead of heliocentric) when studying its rotation. They also assumed that the primary torque affecting the satellite's attitude is SRP and the gravity gradient torques is negligible. In addition, since the study is about long-term evolution of the rotational state and the duration of time in which the satellite is in the Earth's shadow is small for GEO satellites, they can ignore shadowing effects in the analysis.
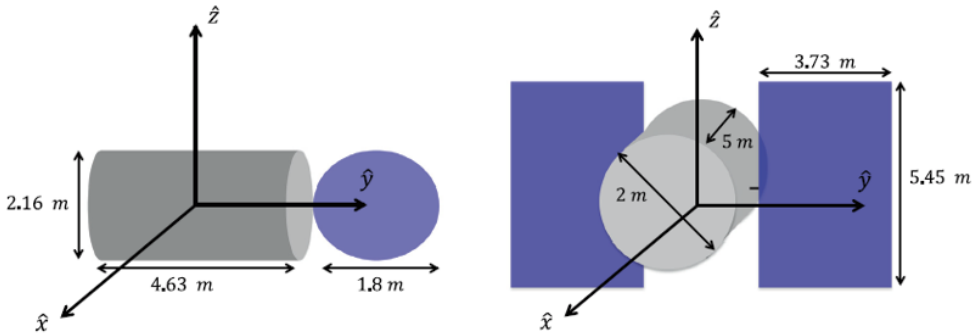
Figure 2.18.: BOEING 376 satellite model (left) and GORIZONT satellite model (right) (*Albuja et al.*, 2015).

As a result, *Albuja et al.* (2015) found that the averaged dynamics using YORP proved to capture the dynamical evolution accurately for the case of BOEING 376 model. They were also computationally much faster than the numerical integration. In addition, the authors also perform simulations for long term evolution over 40 year

time period. For the comparison with observational data, the authors use several three-axis stabilized satellites from GORIZONT and RADUGA family. They found that the results demonstrate that finding the suitable YORP coefficients to match the observations by adjusting the density in-homogeneity or rotating one of the solar panels is within the realm of physical possibility. Adjusting the density in-homogeneity can be applied to any kind of satellite model by shifting the center of mass, while rotating one of the solar panels is only applicable to GORIZONT satellite model. In addition, the authors also analyzed the effect of having a momentum-wheel-transfer angular momentum. They found that the momentum wheels cannot explain the observed behavior therefore they concluded that the inferred coefficients obtained by not incorporating any momentum wheels are a valid measure of the order of magnitude of the normalized inferred YORP coefficients.

Earl (2017, Chapter 5) demonstrated (for the first time), that an inactive box-wing GEO satellite's sidereal spin period can be estimated and that its spin period variation can be simulated, to a first-order approximation, when applying the basic assumptions of its solar panel reflectance and attitude characteristics. As the background of the research, the author realized from previous studies that recent observations of inactive GEO box-wing satellites have revealed rotational motion with diverse spin periods ranging from several seconds to several hours, suggesting complicated attitude dynamics, in general. However, most of those studies did not present models or calculations that verified the hypothesized spin period variation causes or the force magnitude range. Therefore, in his study, *Earl* (2017, Chapter 5) simulated the observed spin period variations of a defunct satellite named ECHOSTAR 2 using SRP torque modeling that was based on numerical analysis. The ECHOSTAR 2 satellite was selected because its light curves suggested the most stable spin axis variation relative to those of other 10 satellites in the previous study *Earl* (2017, Chapter 4).
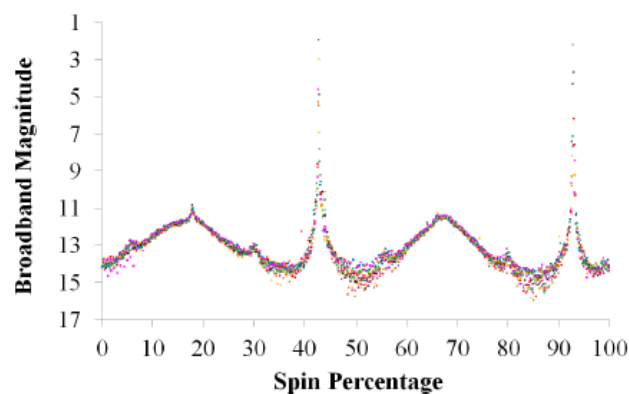
Figure 2.19.: An example of ECHOSTAR 2 folded light curve *Earl* (2017, Chapter 4).

In his dissertation, *Earl* (2017, Chapter 5) first presented the estimated sidereal spin

periods of the ECHOSTAR 2 box-wing GEO satellite, on the dates corresponding to the spin axis orientations estimated in *Earl* (2017, Chapter 4). Reported previously in *Earl* (2017, Chapter 3), all light curves of ECHOSTAR 2 contained four distinct and alternating features over each inferred spin period; two broad (likely diffuse reflection) features and two thin and sharp (likely specular reflection) features as shown in 2.19 which suggested four sides of the box-wing satellite's box portion. The author found that the thin, sharp features appeared similar in shape and amplitude and were consistently separated by 50% of a spin period, suggesting that two reflective surfaces, 180° of a rotation apart, were specularly reflecting sunlight to the observer during each satellite rotation. This further suggested that the two highly reflective mirrored radiators, and not the solar panels, were the sources of the bright specular flares observed in 2012, 2014, and 2015.
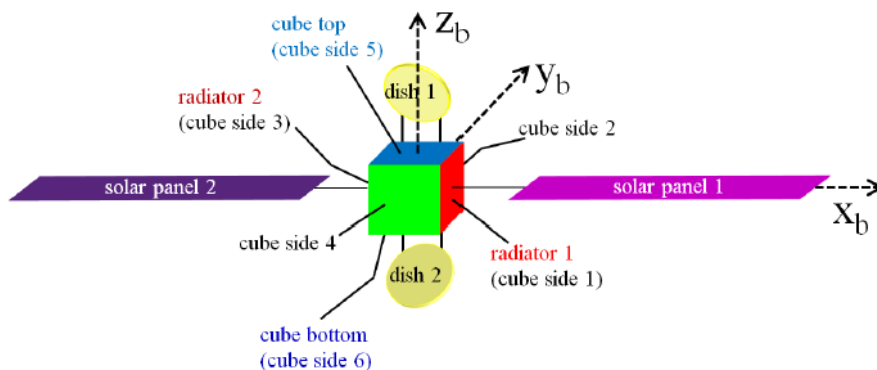
Figure 2.20.: Box-wing satellite model which is used in *Earl* (2017, Chapter 4).

The next part of the *Earl* (2017, Chapter 5) presented simulations of ECHOSTAR 2's spin period variations, based on the spin axis orientations. The free parameters that were considered when conducting the angular velocity variation simulations included each solar panel's body frame orientation (including the *canting angle* between the two panels) and each panel side's reflectivity. The reflectivity parameters of ECHOSTAR 2's solar panels have been assumed because most of the satellite's specifications are proprietary. These simulations were required to determine the likely solar panel orientations that would result in the simulated spin period variations most closely resembling the observed spin period variations. Fig. 2.20 shows the satellite model for ECHOSTAR 2 that was used in the simulations. As a result, Fig. 2.21 demonstrates the similarity between the observed and simulated spin period variation of ECHOSTAR 2 over a nearly four-year and over a ten-year time span, respectively. The simulation successfully predicted the overall decrease of the spin period and the decrease of the spin period amplitude over time. This simulation also successfully predicted the existence of the spin period inflection points where the spin period variation rate decreases momentarily before resuming toward the global maximum or global minimum spin period. These points are around days 160, 370, 480, 1100, and 1230 as can be seen on the left side of Fig. 2.21.
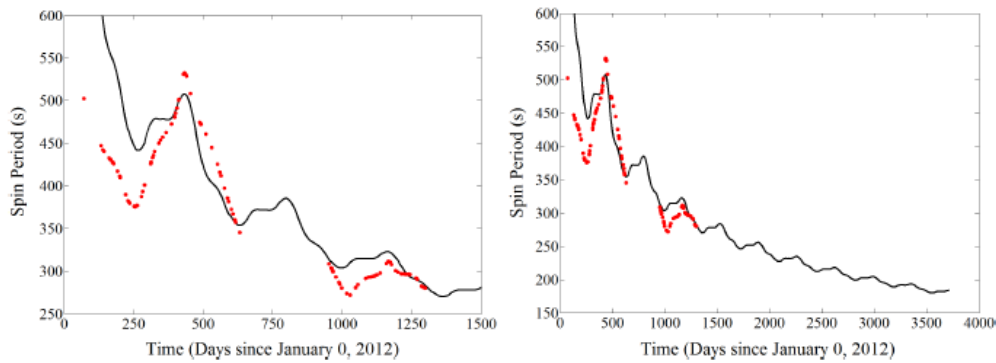
Figure 2.21.: Spin period evolution of ECHOSTAR 2 resulted from a simulation. Dotted line: observational data; solid line: result of simulations (*Earl*, 2017, Chapter 5).

As an attempt to further explores the YORP effect for highly asymmetric inactive satellites, *Albuja et al.* (2018) used the effect to simulate the observed rotation rates of GOES 8 and GOES 10 satellites which are two highly asymmetric defunct geosynchronous satellites. The study wants to highlight the importance of short period variations for highly asymmetric inactive satellites due to the YORP effect. For that purpose, they propagated the angular velocity and obliquity of each satellite using a full attitude integration, spin averaged dynamics and year averaged dynamics. Then, they analyzed the ability of the spin and year averaged dynamics to capture the short period variations obtained with the full attitude integration. Furthermore, they use the YORP theory, accounting for the short period terms, to compare the predicted behavior of the GOES 8 and GOES 10 satellites to observations that have been taken of these satellites over several months. For the simulations, the authors use simple and complex models of both satellites. The latter accounts for all the major components of the satellite which include the solar sail, bus, solar panel and trim tab. The simple satellite model is used to explore the importance of short period terms for highly asymmetric satellites. The complex satellite model is used to compute the instantaneous moment acting on the satellite as a result of the YORP effect. As a result, they found that the year averaged solution accurately captures the secular change in both the angular velocity and obliquity. They conclude that the result strengthens the hypothesis that the YORP effect could be an explanation for the observed changes in defunct satellite rotation period.

In addition to the result in the previous paragraph, *Albuja et al.* (2018) also see that the model which fits the observations for the GOES 8 satellites predicts that it should enter a tumbling state shortly after the last epoch of fit data for the satellite. The authors further hypothesize that there is likely a cyclical process where the satellite repeatedly enters a tumbling state. Their argument is that once the satellite begins to tumble it begins to spin about the minimum moment of inertia, as this is the axis most easily accelerated in the absence of angular momentum. As the satellite

spins faster and faster, energy dissipation (discussed in Section 2.2.3) will become an important factor which will once again cause it to spin about the maximum moment of inertia. Once a stable spin has been reached, the YORP effect will once again be the major torque on the satellite. The authors also notice that more recent observations of GOES 8 satellite show a spin state consistent with the body being in non principal axis rotation.

Motivated by the result of *Albuja et al.* (2018), *Benson et al.* (2018) analyzed several aperiodic light curves (covering several years) of defunct GOES 8 satellite to explore the hypothesis that some satellites cycle between complex and uniform rotation due to the combined influences of YORP and internal energy dissipation. In their work, the authors leveraged torque-free rigid body dynamics and the satellite's known mass properties, geometry, and surface materials, as well as simulated light curve surveys with a high fidelity model to better understand how the fundamental tumbling periods manifest themselves in observations. They later obtained well-fitting rotation states at each observation epoch by using strong trends resulting from the surveys. As a result, they found that the rotation states indicate that after the rapid spin down in early-mid 2014, the satellite went through at least one complete spin cycle between late 2014 and early 2018, with its effective spin period varying between 5 and least 40 minutes over this span. The aperiodic nature of the observations indicates that the satellite remained in at least mildly complex rotation over the period. Overall, the authors found that in terms of GOES 8's dynamical evolution, the observed tumbling light curves are consistent with the hypothesis that the YORP effect creates spin rate cycles and can drive satellites from uniform to complex rotation.

In an effort to further explore YORP effect on RSOs, *Benson et al.* (2020) analyzed light curve observations of five nearly identical defunct GOES 8-12 satellites obtained between 2014 and 2018. Previous observations show large diversity in their evolutionary time histories, with several satellites in consistent slow tumbling, GOES 10 in fast uniform rotation, and GOES 8 transitioning between both. By investigated YORP dynamical models on the satellites, the authors found that YORP driven spin state evolution is strongly dictated by end of life appendage orientations, which differ among the five satellites. They also found that the known end of life configurations are consistent with the observed evolution of GOES 8 and GOES 10. In the case of GOES 9, the authors concluded that the long-term evolution of its tumbling motion (particularly the return to uniform rotation and the nearly constant tumbling) remains unclear due to the lacking of an energy dissipation model. They also concluded that the dynamical modeling to better understand defunct GEO satellite spin state evolution needs to be improved. Also, additional observations of GOES and other defunct GEO satellites are needed to gain further insight into the ongoing satellite spin state evolution.

2.5. Characteristics of GLONASS satellites

In this section, we describe some characteristics of the GLONASS satellites especially those which we assume are relevant to this study. At the end, we also discussed the disposal mechanism for MEO satellites.

GLONASS (*Global'naya Navigatsionnaya Sputnikova Sistema*) is the second group of satellite navigation system in MEO after GPS (Global Positioning System). The first GLONASS was a test satellite named URAGAN (means Hurricane) which was launched by the Soviet Union on 12 October 1982. GLONASS is the second-generation[22] dual-use governmental global satellite navigation system of the Russian Federation. On 24 September 1993, the GLONASS system with initial operational capability of 12 satellites was commissioned for military service. GLONASS with full operational capability (24 satellites) was deployed in 1995 (*Revnivykh et al.*, 2017).

Three generations of GLONASS satellites have been built and operated after nearly 40 years of its history now (Fig. 2.22). The first generation which consists of four type or block (I, IIa, IIb, and IIv[23]) launched firstly in 1982 and were operating until 2008; the second generation which is called GLONASS-M launched since 2003; and the third generation which is called GLONASS-K introduced in 2011. Each new generation of GLONASS satellites extended the satellite capabilities and improved the overall system performance. In parallel to technical improvements, the in-orbit lifetime was also continuously increased. Among those models, only GLONASS IIv and GLONASS-M are relevant to this study since all the inactive GLONASS satellites in the AIUB light curve database are of those types (see Section 3.5).
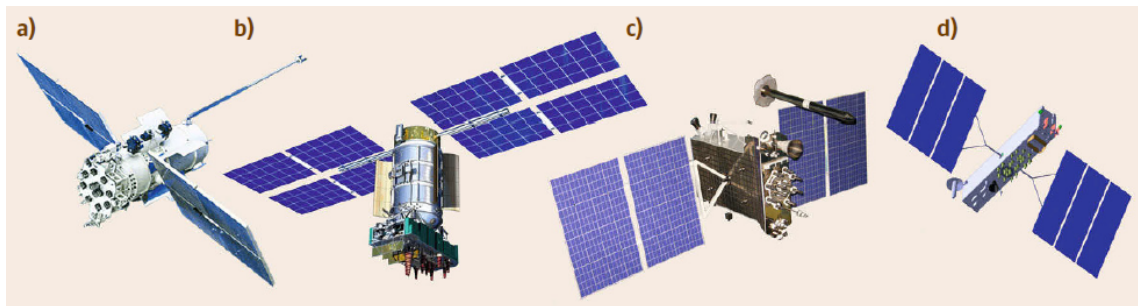
Figure 2.22.: The GLONASS satellites family: (a) GLONASS IIv, (b) GLONASS-M, (c) GLONASS-K1 (d) GLONASS-K2 (*Revnivykh et al.*, 2017).

---

[22]The predecessor of GLONASS is a low-altitude satellite navigation/communication system called Tsyclon/Tsikada which became operational in 1976 (*Revnivykh et al.*, 2017).

[23]Letter v in block IIv is the English transliteration of the Russian alphabet's third letter.

2.5.1. Satellites

GLONASS IIv and GLONASS-M satellites have similarities and differences. As displayed in Fig. 2.22, both types share the same core structure but GLONASS-M satellites are easily distinguished by different placement of the solar panel rotation axis and by the fact that they no longer carry a magnetometer boom. Other characteristics of both types are listed in Table 2.1. We can see in the table that they both employed a pressurized platform design (to protect their payloads against the space environment). They also have similar mass of roughly 1.4 ton (including propellant for orbit maintenance) and are made up of a cylindrical structure (with a length of about 3.5 m). As an improvement to its predecessor, GLONASS-M satellites have a much longer design lifetime and significantly larger solar arrays to deliver much more power (nearly 50% more). Both types carry a laser retroreflector array (LRA) for satellite laser ranging measurements. Furthermore, in both types, heat dissipation was achieved through heat exchangers and four thermal control flaps which are distributed evenly around the bus (as can be seen in Fig. 2.22).[24] The opening angle of these shutters could be varied and allowed the adjustment of the internal temperature with an accuracy of about 5°C (*Revnivykh et al.*, 2017).

Table 2.1.: Some characteristics of GLONASS IIv and GLONASS-M spacecrafts (*Revnivykh et al.*, 2017).

Parameter	GLONASS IIv	GLONASS-M
Platform design	pressurized	pressurized
Mass (kg)	1415	1415
Bus structure	cylinder	cylinder
Design lifetime (yr)	3	7
Solar array size (m^2)	25	32
System power (W)	1000	1450
LRA	yes	yes

2.5.2. Orbits

Each GLONASS satellite orbits the Earth in MEO and is a member of a constellation system. The system nominally consists of 24 operational satellites which are evenly distributed over three orbital planes (which makes them separated by 120° in the equatorial plane). Some of the constellation parameters are summarized in Table 2.2. Given 8 satellites per orbit, we have the argument of latitude difference between the satellites equals to 45°. Each eight days a satellite passes over the same point on the Earth's surface. All the satellites are moving relative to Earth's surface

---

[24]Better images of the flaps can be seen in Appendix D.

practically along the same ground tracks due to shifting in their orbital planes. The higher orbital inclination of GLONASS satellites ($\approx 65°$) compared to other MEO navigation satellites provides improved visibility conditions over the area of the Russian Federation. Worldwide GLONASS users likewise benefit from a good sky coverage with a reduced visibility gap around the celestial pole (*Revnivykh et al.*, 2017).

Table 2.2.: Some of nominal GLONASS constellation parameters (*Revnivykh et al.*, 2017).

Parameter	Value
Number of operational satellites	24
Number of orbital planes	3
Number of satellites in a plane	8
Eccentricity	$e < 0.01$ (orbit near circular)
Inclination	$i = 64.8° \pm 0.3°$
Nominal altitude	$h = 19100$ km
Period of revolution	$T = 11\text{h}\,15\text{min}\,44\text{s} \pm 5\text{s}$

2.5.3. Attitudes

In GLONASS satellites, attitude control was achieved through reaction wheels, which were periodically unloaded using magnetorquers. In the case of GLONASS IIv type, reference measurements of the magnetic fields were provided by a magnetometer, which was mounted on an external boom to avoid magnetic disturbances by the satellite body. The GLONASS satellites were also equipped with a hydrazine propulsion system. It comprised two of 5 N thrusters for orbit correction and 24 of 0.1 N thrusters for orientation changes and despinning after orbit injection. After reaching their assigned orbital slot, the satellites kept their nominal position within an argument-of-latitude deadband of $\pm 5°$ throughout their operational lifetime with no need for further correction maneuvers (*Revnivykh et al.*, 2017).

The nominal orientation of a GLONASS satellite is driven by a small set of requirements (*Revnivykh et al.*, 2017).[25]

Firstly,   the boresight of the antenna must always be directed to the center of the Earth to maintain an optimum coverage and proper strength of the navigation signals.

Secondly,   the solar panels shall be aligned perpendicular to the Sun direction to maximize the projected area and thus the received solar energy. The

---

[25]This requirements are largely independent of the particular system or satellite manufacturer therefore they are also applicable to other global navigation satellite system (GNSS) satellites.

> solar panel rotation axis must therefore be oriented perpendicular to the plane spanned by the Sun and Earth direction.

Finally,   one of the satellite faces perpendicular to the antenna boresight and solar panel rotation axis should permanently point into the hemisphere opposite the Sun to facilitate thermal stabilization of the atomic clocks (mounted close to this cool panel).

The resulting attitude control mode which fulfills the above set of requirements is known as *yaw-steering mode* which is illustrated on the left side of Fig. 2.23.[26] Maintaining the ideal satellite attitude requires two things: a permanent rotation of the spacecraft body about the Earth-pointing $+z$-axis as well as a rotation of the solar panels about the $+y$-axis.
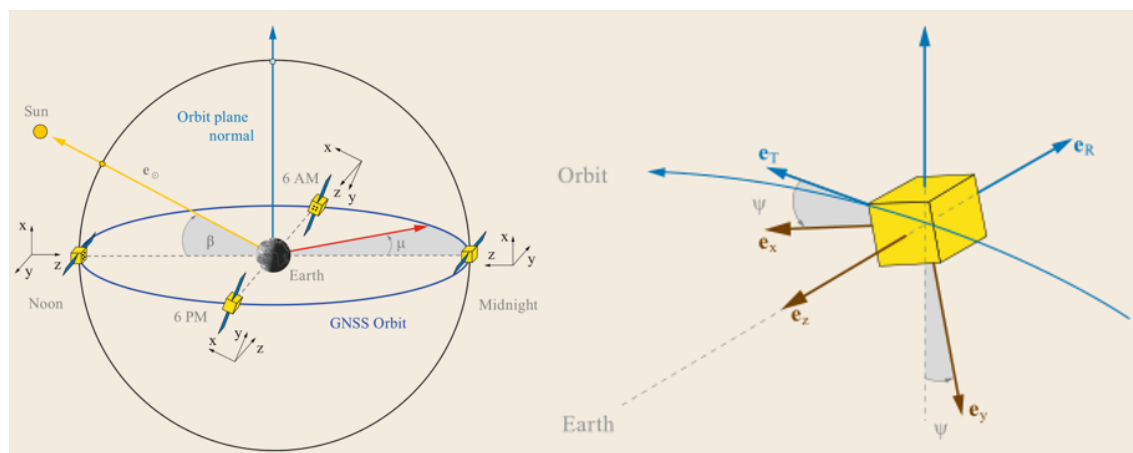
Figure 2.23.: GNSS satellite orientation in yaw-steering mode (left) and definition of yaw-angle (right) (*Revnivykh et al.*, 2017). The symbols are explained in the text.

The required orientation of the spacecraft body is most easily described in an orbital reference frame aligned with the unit vectors

$$\boldsymbol{e}_{\mathrm{R}} = \frac{\boldsymbol{r}}{\|\boldsymbol{r}\|}, \qquad \boldsymbol{e}_{\mathrm{T}} = \boldsymbol{e}_{\mathrm{N}} \times \boldsymbol{e}_{\mathrm{R}}, \qquad \boldsymbol{e}_{\mathrm{N}} = \frac{\boldsymbol{r} \times \boldsymbol{v}}{\|\boldsymbol{r} \times \boldsymbol{v}\|} \qquad (2.50)$$

---

[26]In the figure, the principal spacecraft axes have been labeled in accord with established conventions of the international GNSS service (IGS):

1. The $+x$-, y-, and z-axis form a right-handed coordinate system attached to the satellite body.

2. The $+z$-axis coincides with the antenna boresight direction.

3. The y-axis is parallel to the rotation axis of the solar panels. Furthermore, the $+y$-direction is assigned such that the $+x$-panel is illuminated by the Sun during nominal yaw-steering, while the $-x$-panel is oriented toward deep space.

in the radial, transverse, and normal direction (right side of Fig. 2.23), which are defined by the instantaneous position $\boldsymbol{r}$ and velocity $\boldsymbol{v}$ of the GNSS satellite. The yaw-angle Ψ specifies the angle between the $\boldsymbol{e}_{\mathrm{T}}$- and $\boldsymbol{e}_{\mathrm{x}}$-axes for a right-handed rotation around the $+z/-R$-axis. For $\Psi = 0°$, the spacecraft $+x$-axis is aligned with the transverse direction and $+y$ is oriented antiparallel to the orbital angular momentum. The nominal yaw angle in yaw-steering mode can be expressed as

$$\Psi = \mathrm{atn2}\left(-\tan\beta, \sin\mu\right) \tag{2.51}$$

where β denotes the elevation of the Sun above the orbit plane and μ measures the orbit angle relative to the midnight point (left side of Fig. 2.23). Thus, the nominal attitude of a GNSS satellite is fully determined by its orbital position and the direction of the Sun.

2.5.4. Disposal mechanism

The region where GNSS satellites are located is one of the three regions in the Earth's vicinity with high spatial densities since decades ago (left side of Fig, 2.2). With human depending more and more on the satellite navigation technology, the number keeps on increasing. Currently, four constellations of global navigation satellite system (GNSS) are fully operational[27] which comprise more than 120 satellites in MEO. It is predictable that the region near the constellations will become increasingly crowded in the future since the four constellations have similar altitudes (around 20,000 km) and inclinations (around 60°). Therefore, considering the sensitive applications of the navigation satellites and the absence of any natural sink mechanism, such as the atmospheric drag, a careful debris prevention policy is necessary to preserve MEO environment in order to avoid in the future the problems now already faced by LEO and GEO environments (*Rossi et al.*, 2017).

MEO region does not have an international regulation for end-of-life disposals like LEO and GEO regions which are considered as protected regions. As a result, many decommissioned satellites are left in orbit. In case of GLONASS satellites, no end-of-life disposal maneuvers were performed unlike GPS (*Domınguez-González et al.*, 2013). Therefore, it is interesting to know how RSOs are distributed around the nominal height of the four constellations.

If we define the region around a GNSS constellation as

$$perigee > h - 0.5 \times \Delta h \qquad apogee < h + 0.5 \times \Delta h$$

where h is the nominal altitude of the constellation and Δh is the minimum distance

---

[27]They are the United States' Global Positioning System (GPS), Russia's Global Navigation Satellite System (GLONASS), China's BeiDou Navigation Satellite System, and the European Union's Galileo. BeiDou Navigation Satellite System consists of satellites in MEO, GSO, and IGSO.

between two adjacent constellations, then we can find the minimum perigees and maximum apogees which can be use to define the region around GNSS constellations (Table 2.3[28]).

Table 2.3.: Minimum perigees and maximum apogees that define the region around GNSS constellations. The nominal altitudes h are taken from *Hugentobler and Montenbruck* (2017). The Minimum perigees and maximum apogees were calculated using the minimum distance between two adjacent constellations $\Delta h = 1052$ km.

Constellation	h [km]	Minimum perigee [km]	Maximum apogee [km]
GLONASS	19130	18604	19656
GPS	20180	19656	20708
BeiDou-M	21530	21002	22054
Galileo	23220	22696	23748

Based on orbital data for RSOs from Space-Track website (www.space-track.org)[29] as of January 2023, we can see that the GLONASS constellation region has the highest population (left side of Fig. 2.24). This is followed by the BeiDou-M constellation region, Galileo constellation region, and GPS constellation region. If we also define the whole GNSS region as perigee > 18000 km and apogee < 24000 km then it contains more than 370 objects. The distribution of the objects can be seen on the right side of Fig. 2.24. There, we can see how GLONASS satellites (CIS payloads) are located in a small relatively high density region unlike other GNSS satellites. Overall, Fig. 2.24 shows that GLONASS satellites are located in the highest density region among GNSS satellites.

Previous studies reported that the disposal orbits used by the GNSS in MEO can be unstable, i.e., undergo significant eccentricity growth[30] over several decades (*Jenkin and Gick*, 2001). This is due to resonance conditions from the combined gravitational interaction of geopotential harmonics, Moon and Sun. Consequently, the disposal orbit perigee can penetrate into the region of the operational constellation and producing a collision risk for the operating vehicles. One of those studies was conducted by *Pardini and Anselmo* (2012) in which the authors analyzed the long-term evolution and environmental impact in MEO of disposed GPS and GLONASS satellites as well as the associated upper stages. A newer similar study was performed by *Rossi et al.* (2017).

---

[28]In the table, BeiDou-M means the MEO part of the BeiDou Navigation Satellite System.

[29]The website is owned by the United States Department of Defense and publicly available for registered users.

[30]Which is strongly dependent on the initial eccentricity, argument of perigee, and right ascension of ascending node.
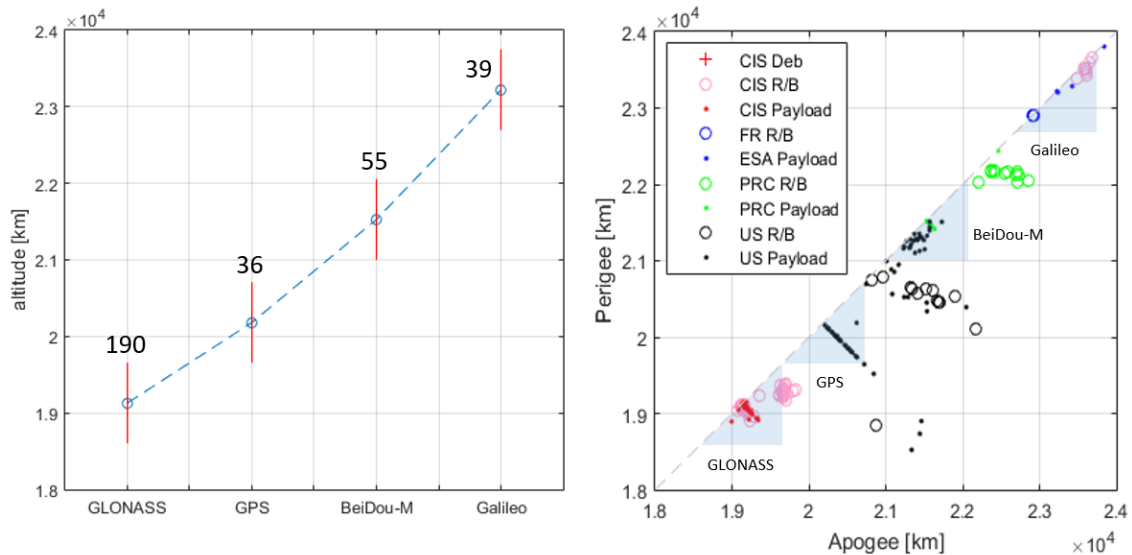
Figure 2.24.: The range of altitudes that define the region of the four GNSS constellation according to Table 2.3 with the number of objects inside (left) and the distribution of the objects inside each region (right). On the left image, the length of each bar is 1052 km. On the right image, CIS represents Russia, FR represents France, ESA means European Space Agency, PRC means Peoples Republic of China, US means United States of America. Deb means debris, R/B means rocket bodies. The shaded triangles represent the area according to Table 2.3.

Pardini and Anselmo (2012) based their study on really disposed - not just simulated - objects in order to investigate the long-term effects of the practices adopted so far. Altogether, the authors used 179 abandoned intact objects associated with GLONASS (including two ETALON satellites) and 33 objects associated with GPS, i.e., 212 objects in total. In their study, the orbits of the objects with apogee higher than 17,000 km, as of 1 May 2011, were propagated for 200 years with a numerical code. The calculation takes into account all relevant perturbations, i.e., the EGM96 Earth's gravity field harmonics, up to the 16th order and degree, luni-solar third body attraction, solar radiation pressure with eclipses and, when applicable (namely below 1000 km), air drag, estimated using the 1976 United States Standard Atmosphere. The radiation pressure and drag coefficients were set, respectively, to 1.4 and 2.2 for all the propagated objects.

Fig. 2.25 and Fig. 2.26 show the result for the disposed satellites. The first figure compares the distribution of the satellites at the initial epoch and after 200 years while the second shows the evolution of the density distribution of disposed GLONASS satellites in a 50-years interval. We can see from the two figures that at present, the GLONASS abandoned spacecraft are concentrated around the constellation operational altitude and this situation will not change for several decades. Finally, the perturbation induced long-term eccentricity growth will lead to the

crossing of the GPS operational altitude, around one century in the future, and, about a further half century later, to the crossing of the BeiDou-M and Galileo altitudes as well. However, the object densities will be approximately 2–3 orders of magnitude less than the present value at the GLONASS height.
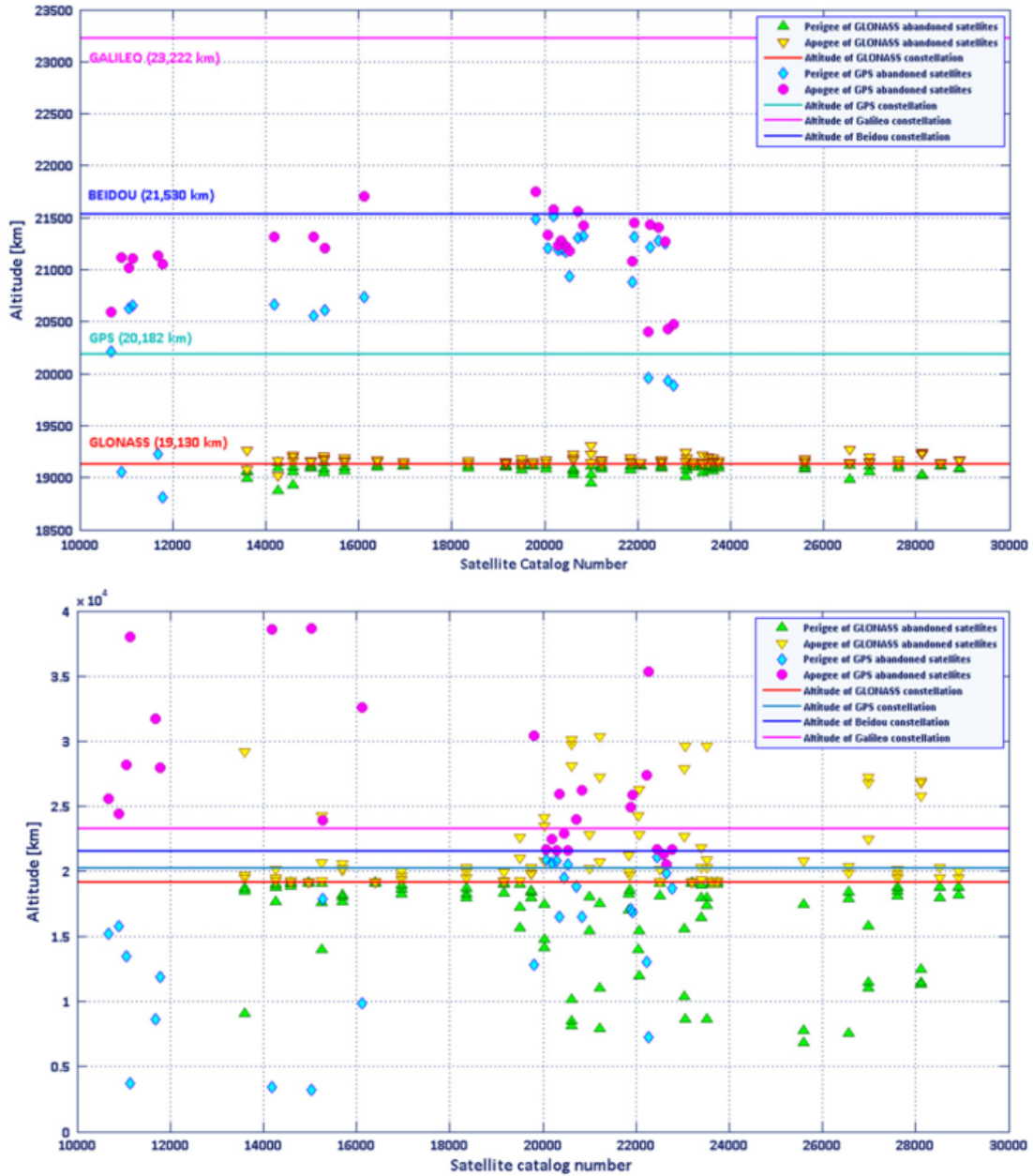
Figure 2.25.: Disposed satellites associated with the GPS and GLONASS constellations at the initial epoch (1 May 2011) (top) and their condition after 200 years (bottom) (*Pardini and Anselmo*, 2012).

51
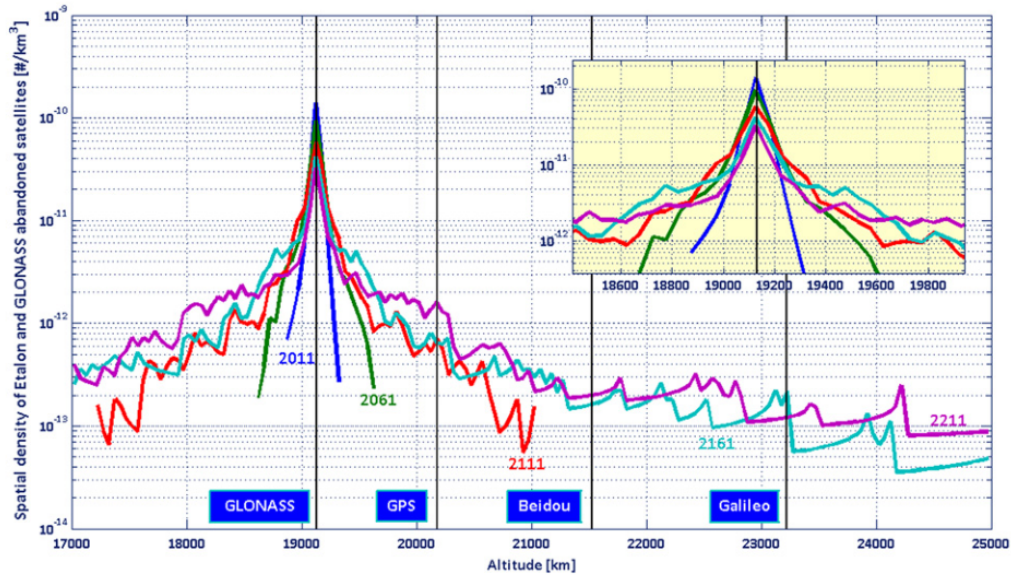
Figure 2.26.: Evolution, over 200 years, of the density distribution of the GLONASS abandoned satellites, as of 1 May 2011 (*Pardini and Anselmo*, 2012). The inset shows the distribution around the constellation operational altitude.

Regarding the environmental impact in MEO, *Pardini and Anselmo* (2012) found that the long-term collision risk posed by the objects abandoned so far is, in general, very low (even not considering conjunction assessment and avoidance maneuvers for the active spacecraft). The GLONASS constellation has the highest probability of collision which is less than 1/300 (integrated over 200 years) while practically negligible for other constellations. Later study conducted by *Rossi et al.* (2017) analyzed different disposal strategies for GNSS satellites using also other objects larger than 5 cm taken from MASTER[31]. The authors found that the most "problematic" constellations are GLONASS and BeiDou-M. The conclusion is driven by the future launch traffic hypothesized for these constellations and, in the case of GLONASS, by the past practices that left already a significant number of large uncontrolled spacecraft in the constellation orbital zone.

2.6. Conclusion

Inactive GLONASS satellites (which are the main objects of this study) were once part of Russian GLONASS constellation satellites in MEO region. This constellation together with, currently, four other constellations are part of global navigation satellite systems (GNSS). Each constellation consists of around 30 satellites which is

---

[31]MASTER is the European model to assess the risk of high velocity impacts of space debris on satellites in Earth orbit.

the reason why GNSS region has relatively high spatial density since decades ago. It is expected that the density will keep on increasing (hence increasing the probability of collision) especially around the operational altitude of GLONASS satellites. This reality is important in the context of long term sustainability of outer space activity. Coupling this with the fact that all inactive GLONASS satellites are equipped with LRA which will benefit the observational aspect of future research, makes attitude studies of inactive GLONASS satellites exciting. Furthermore, light curves data and their inferred period for the inactive satellites are available in AIUB light curves database which is the topic of the next chapter. Section 2.2 and 2.3 of this chapter will be the basics for modeling the spin period evolution of the inactive satellites which will be carried out in Chapter 4.

3. AIUB Light Curve Database

The AIUB light curve database is a collection of space debris light curves and their related information (e.g. apparent spin period) produced and maintained by the institute. The data is obtained at the Swiss Optical Ground Station and Geodynamics Observatory Zimmerwald (SwissOGS) or Zimmerwald Observatory for short, which is owned by the institute. The observatory is located about 10 km to the south of Bern in Switzerland and has been taking photometric data routinely since January 2007. Until November 2020, the database contains more than 4,500 light curves from more than 500 *selected space objects* which cover all orbital regions and different types of objects. The words "selected space objects" is emphasized to prevent people from regarding the database as a result of a survey. The light curve itself is the variation of magnitude as a function of time with duration spans from 3 until 20 minutes and sampling interval of about twice the exposure time. Related information in the database includes the classification of the light curves and the corresponding phase diagrams.

This chapter begins by explaining how the AIUB light curve database is produced, maintained, and improved during the time of this study. The planning of the observation is described in Section 3.1. The observation itself is discussed in Section 3.2. The processing of the observation's result is described in Section 3.3. After that, Section 3.4 describes the latest status of the database using statistics. Finally, Section 3.5 describes the database collection regarding inactive GLONASS satellites which will be the main topic of the next chapter. Again, the statistics presented in this chapter will be informing more about the nature of the database itself rather than that of our space environment.

3.1. Planning

Planning for the photometric observations is performed on a daily basis using AIUB's internal tools (*Silha et al.*, 2018). One of their primary tasks is collecting the data for calculating the pointing of the telescope during observations. This data is obtained from publicly available two-line elements (TLE) and that from AIUB internal catalog of space objects. The data is then processed using Simplified General Perturbation (SGP) model to calculate the visibility and to get the ephemerides of the objects. Other tools are used to organize the targets where they are classified into several campaigns according to their orbital regime which covers from low Earth orbit to

geosynchronous orbit. Each campaign can have its own setting that constrains the visibility of its members and each member can have its own setting for further constraints. Overall, due to weather condition and the telescope system status, on average, one planning is created every two days in the last four years. Currently, around 160 space debris objects are monitored.

For a specific object, additional settings which are evaluated based on previous observation results are also defined. These include default exposure time, camera filter, the minimum and maximum duration of observations, and the so called *nominal observation return time* (NORT) which is measured in days. NORT is a critical factor in term of AIUB light curve database since it further limits the visibility of an object regardless of its orbital motion relative to the station. An object should not be observed if the last observation time is less than the object's current NORT value. In this case, the object is considered not visible. So, basically, NORT is the ideal (real) number of days we want to have between two successful observations. By specifying the NORT value for an object, we can prevent its unnecessary high observing run which will affect other objects. Another factor which is also able to further limit a "visibility" of an object is the interference of the so called SLR priority targets into the visibility windows of the object. In this case, SLR priority targets will get the priority to be observed unless stated otherwise.

One important factor that has to be considered in the planning is the photometry time. Due to the reason that the main telescope used for the photometry also performs laser and astrometric observations in the same night, photometry time usually never exceeds 2 hours per night. Fig. 3.1 shows how the photometry time varies in a year. There are two periods with length of 2 hours each: January 1st until April 18th and August 24th until December 31st; two periods with length of 1.5 hours each: April 19th until May 23rd and July 19th until August 23rd; and one period of 1 hour length: May 24th until July 18th. Currently, maximum of 10 objects can be observed in a single night regardless of the photometry time. Another factor which is also affected by the two aforementioned modes of observations is the maximum duration of observation per object per night. This value is currently set to be 20 minutes.

The way the planning is created has evolved through time. Prior to 2015, the only way to create a photometric planning was through command line interface (CLI) to access several scripts and then since 2016 this was simplified by the addition of a couple of Java programs. At the end of 2016, we began creating a computer program with Windows graphical user interface (GUI) to simplify the process further. This was done by encapsulating nearly all available scripts and programs for doing routine photometry planning and data processing at AIUB with a single tool while also adding some useful features. The program was not designed as a replacement of the CLI method but rather as an alternative. Fig. 3.2 shows the main window for the planning phase of the program which is called AIUB Phototool. By the encapsulation, the current interface also adds some levels of security by preventing planners from (accidentally) modifying the scripts and the database beyond what
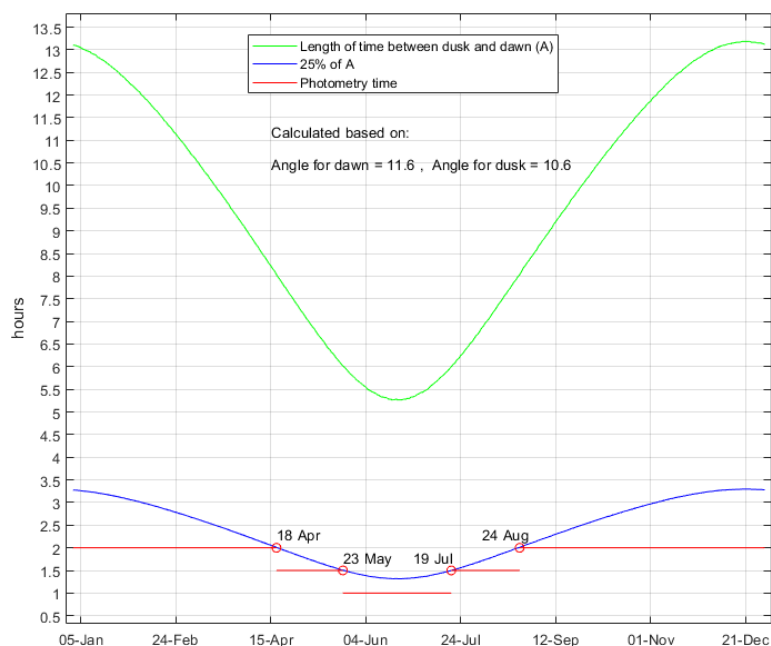
Figure 3.1.: Variation of photometry time used currently in the planning phase of AIUB photometry activity. Angles are expressed in degrees.

is necessary. Nevertheless, planners still have a lot of flexibility in adjusting the planning as the tool still allows experience planners to even interfere with the on-going process of the planning. In addition to the planning, the program is also designed to ease the processing of light curve data which will be discussed in Section 3.3.

AIUB Phototool comes in four modes: 1) daily mode which is used to do a planning and to process a single night observation data; 2) monthly mode which is used to process a month of observation data; 3) checkout mode which is used to process any light curve; and 4) investigation mode which is used to process all light curve of a single object. Therefore, a planning can only be performed in the daily mode. Appendix C gives a more complete introduction to AIUB Phototool.

Several useful features in terms of planning are now available. One of them is the ability to automatically show the observational setting of the selected object and the special groups where the object belongs to (Fig. 3.3). Being able to show immediately the observational setting of the selected object while doing the planning is important since creating the best setting of an object is an iterative process. This is true not only for newly observed objects but also for some objects which change their attitude behavior significantly during their lifetime. The information in which special groups the object belongs to is also useful since this can help the planner in
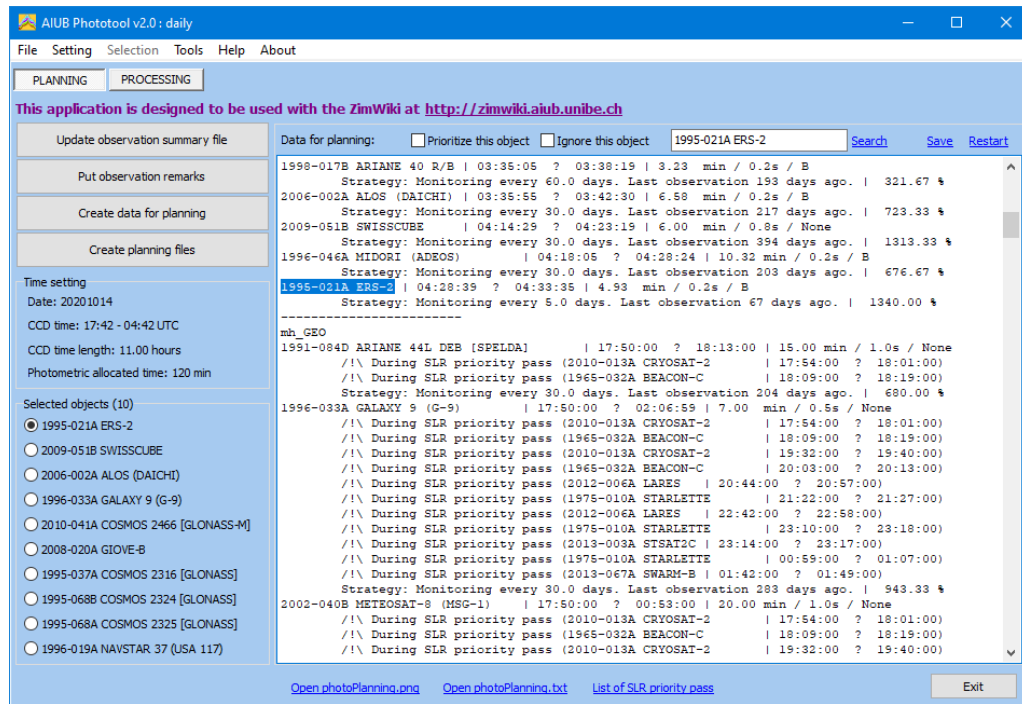
Figure 3.2.: User interface for the planning phase in AIUB Phototool.

refining the level of priority of the objects to be observed (beyond what is possible by the automatic process). Another useful feature is the ability to easily inspect previous results of a selected object since the program also acts as an interface to the database.
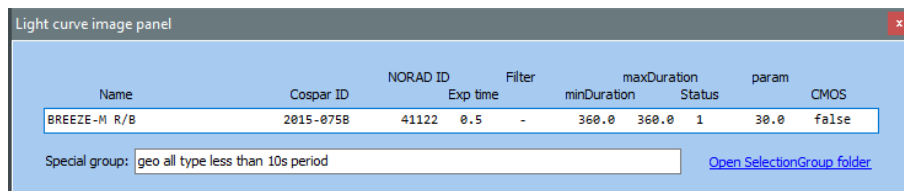
Figure 3.3.: An example of an object setting in AIUB Phototool.

The output of the planning is a schedule chart which shows the available observation windows for the objects to be observed during the subsequent night (Fig. 3.4). The chart is sent to the night observer together with a form containing a list of all targets for the observer to write down his/her comments regarding their observation. All objects in the chart are grouped by their campaign and labeled with their duration of observation, exposure time, and the filter to be used. Using the chart, the observers can organize their best time to observe each of the targets. By using other computer programs, the planner can put additional notes into the chart to help the observer select the optimum time or to do additional tasks which could not be created automatically. AIUB Phototool also allows the planners to use a

publicly available satellite orbit program (Orbitron) to display the selected object passes or to use a website with similar features (`www.heavens-above.com`). This can significantly help them in creating additional notes which could be critical for improving the quality of the planning.
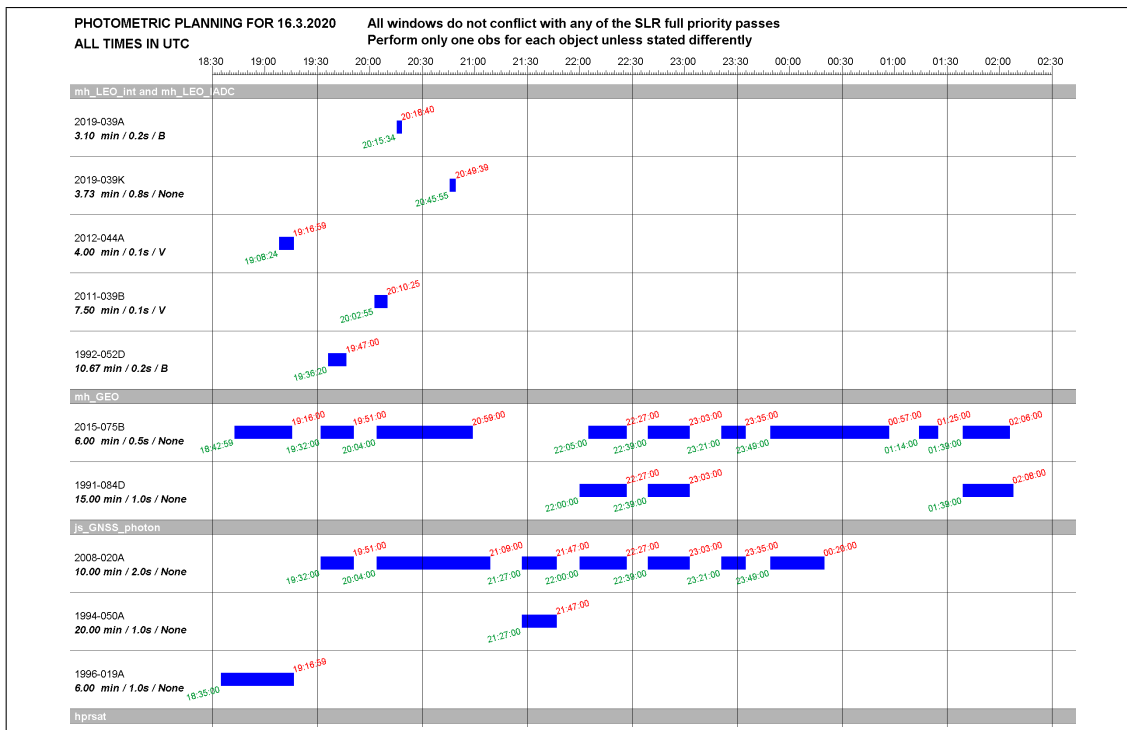
Figure 3.4.: An example of a planning chart for photometric observations. Typically, several windows of observations (the blue bars) are available for GEO and GNSS objects. By examining those available windows, the observers can organize their best time to observe each of the targets.

The concept of NORT is implemented further in AIUB Phototool by the so called *observation necessity factor* (ONF). It is a ratio (expressed in percentage) between the time since last successful observation (in days) and the NORT of an object. The distribution of ONF for all currently monitored objects in the database can be used to assess how up-to-date the database is. Fig. 3.5 shows the planning status of the database on 29 November 2020. We can see from the figure that the status can be considered fair since for all monitored objects in the database (chart a), in general, the profile increases to the left (to the smaller ONF). The high count for the ONF class larger than 1000 is due to the high number of LEO and GEO objects within the category. The reason for this is that some of the objects in those regions have not been visible from the station for a while due to the characteristic of their orbit. Therefore, if we consider only objects that are visible from the station on the date of the observation, the profile is better as shown in Fig. 3.6. Within the tool, member of high ONF class can be easily identified and be put into a higher priority to be

observed.
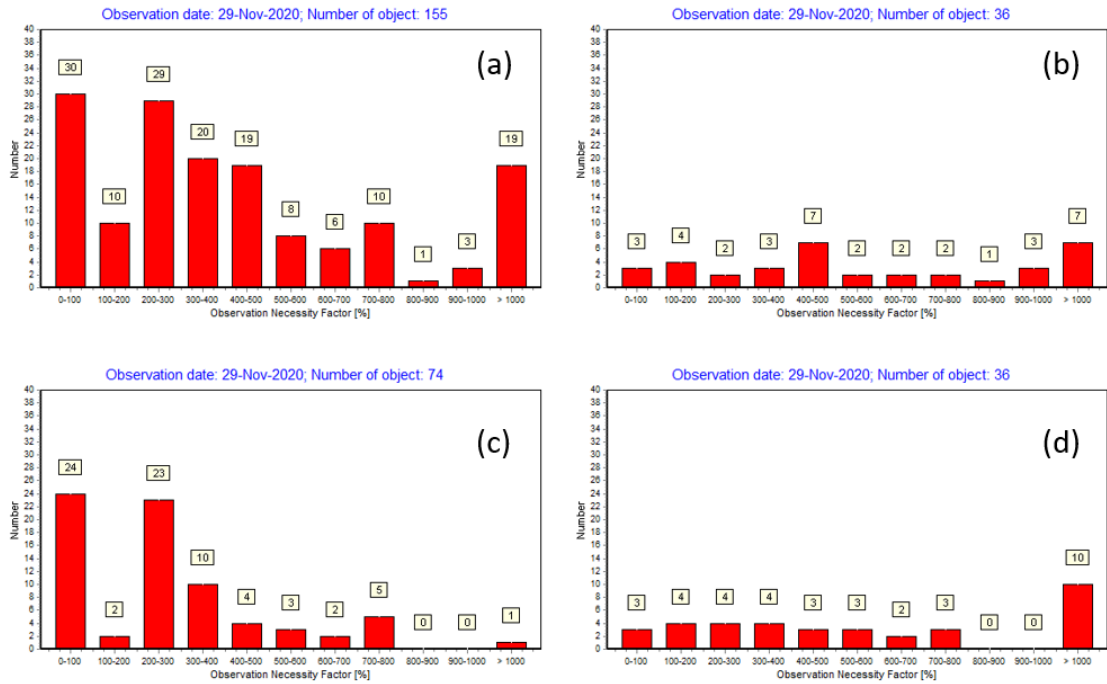
Figure 3.5.: ONF chart on 29 November 2020 for all monitored objects (a); only for monitored LEO objects (b); only for monitored MEO objects (c); and only for monitored GEO objects (d).
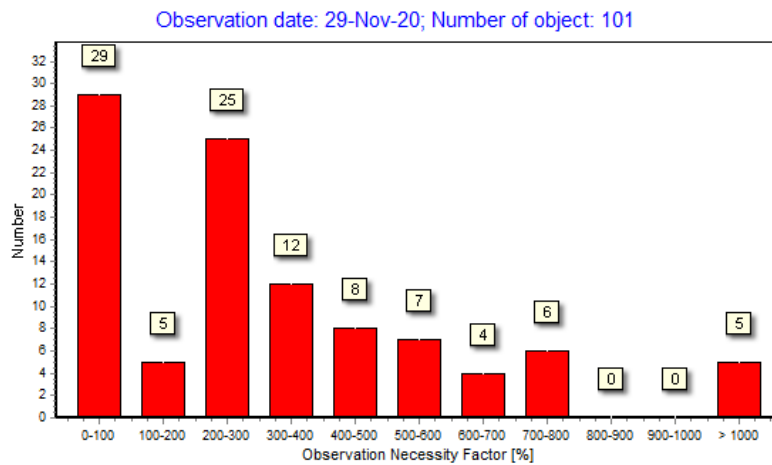
Figure 3.6.: ONF chart on 29 November 2020 for all monitored objects that are visible on the date of the observation.

3.2. Observation

The main telescope for the AIUB light curve database is the Zimmerwald Laser and Astrometry Telescope (ZIMLAT) (Fig. 3.7). It is a Ritchey-Chrètien type of telescope using Alt-Azimuth mount. ZIMLAT is a 1 m aperture telescope with 4 m focal length located at Zimmerwald Observatory (46.8771° N, 7.4652° E, 898 m above sea level). The telescope is equipped with a back-illuminated CCD camera of 2064×2048 pixels which results in a field of view of $26' \times 26'$. The limiting magnitude of the optical system is 19 mag. ZIMLAT has been taking photometry observations routinely since 2007 using Johnson-Cousins B, V, R, I photometric system for very bright objects. ZIMLAT is also used to observe high area-to-mass ratio (AMR) objects without any filter (*Schildknecht et al.*, 2008). Fig. 3.8 shows ZIMLAT system efficiency which considers the telescope and filters transmittance as well as the CCD chip quantum efficiency. In addition to CCD observations, occasionally CMOS observations are performed when higher time resolutions are required. Currently, the photometry observations is normally performed every night weather permitting and if the planning is available. Overall, in the last four years, on average, five light curves are produced every four days.

Figure 3.7.: ZIMLAT telescope which is used as the main telescope for photometry observations at Zimmerwald Observatory.

Photometry observations are performed semi-manually. During one session, the observer should decide when to observe the targets according to the available observation window in the planning chart. Several factors should be considered to get the "ideal time" like the presence of clouds and the effect of the moonlight (in case they are necessary). During the acquisition time, object tracking mode is used based on the obtained ephemerides. Using active tracking, the targets are kept at the center of the subframe. Therefore in the images they appear as a point and
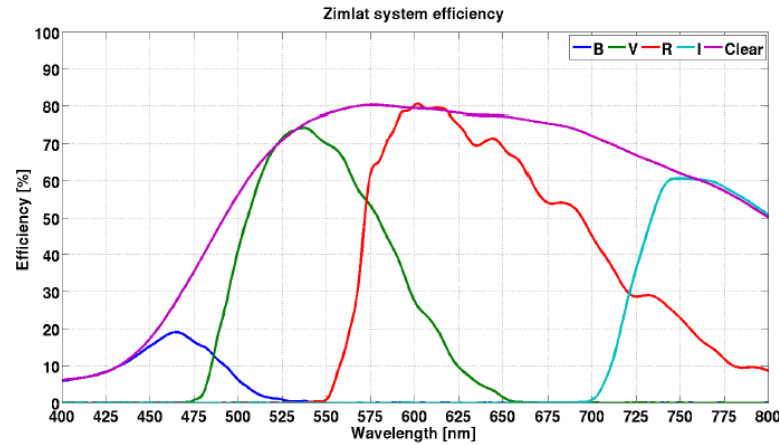
Figure 3.8.: ZIMLAT system efficiency.

the surrounding stars as streaks as shown in Fig. 3.9. In the figure we can see the targets at the center of the images and some star streaks whose length is a function of the target's apparent angular speed on the frame and the exposure time. The left image in the figure was taken with 0.5 s of exposure time while it was 1.0 sec for the right image. Much longer streaks are evident on the left image which is an image for a LEO object compared with that on the right image which is for a MEO object.
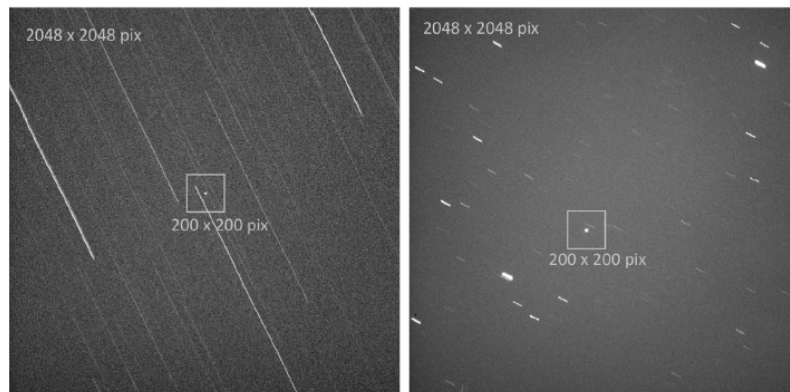
Figure 3.9.: Examples of full frames acquired by ZIMLAT for a LEO satellite (left image) and for a MEO satellite (right image). Shown at the center of the images as boxes are the related subframes and the targets as dots. The images are taken from *Silha et al.* (2018).

The image acquisition process starts with the taking of a full frame image (2064×2048 pixels) centered at the coordinate given by the ephemeris at the beginning of each series. The observer uses this image to find and mark the object on the frame manually. Utilizing this user interaction, the system performs the subsequent acquisitions on subframes of 200×200 pixels ($2.60' \times 2.60'$) to increase the light curve

sampling and actively tracks the object in the subframe throughout the observation. This results to about 1.0 sec of readout time that later translates to frame rate ranges from around 1 frame/s to 0.17 frame/s depending on the exposure time. The exposure time itself depends on the target size and its orbital regime. LEO objects are usually observed using less than 1 sec exposure time while MEO and GEO with at least 1 sec exposure time. Overall, the sampling interval is about twice the exposure time. During the acquisition, the object centroid in the subframe and its total intensity are extracted by an automatic real-time procedure and the results are screened for contamination by background stars or, e.g., over- or underexposures. This way, most of the outliers, like bright star passing close to the object, are removed. After acquiring 500 sub-frames, a full frame is acquired for photometric calibration purposes, resulting in a gap of around 20s between every two series of 500 sub-frames (*Schildknecht et al.*, 2015). After combining with the time tag obtained in each frame header, the light curve is produced which provides the relative intensity over time. No image calibration is performed on the subframes, therefore the main output of the whole process is a light curve in the form of non-calibrated intensity.

3.3. Processing

The light curve data is manually processed using several scripts (*Silha et al.*, 2018). Fig. 3.10 shows the flow of the routine analysis for the light curve processing. Basically, after ignoring the cases with less than sufficient data quantity (the threshold is usually around 30 data points), there are two groups of cases. The first group is the one that clearly shows no repeating pattern visually while the other group shows the opposite (an indication of a repeating pattern). A light curve that shows no indication of visual repetition in the pattern could mean two things. First, the pattern is so simple that it is probably just a function of the object's orbital motion around the Earth as seen from the station. In other words, the object was not rotating relative to the station during the acquisition time. Second, the pattern is not as simple as the first so that it is probably also a function of object's attitude behavior (in addition to its orbital motion) but the spin period is larger than the duration of the observation. The first light curve is called a *stable light curve* and is labeled 6000 while the second is called a *slow rotator light curve* and is labeled 7000. Light curves which show repetition will be further processed after removing the leftover outliers and trends. Since it is constrained by the associated maximum duration of observation which could be too short with respect to the attitude behavior of an object, one light curve obviously is not enough to represent the object's attitude.

The processing of light curves which show an indication of repetition in the pattern could be finished successfully or not. If the spin period could be extracted than the case is considered successfully finished (a *rotator light curve* is found) and the light curve is called *normal* (see the bottom of Fig. 3.10). In the case that it is very difficult to get the period or there is not enough time to finish the process-
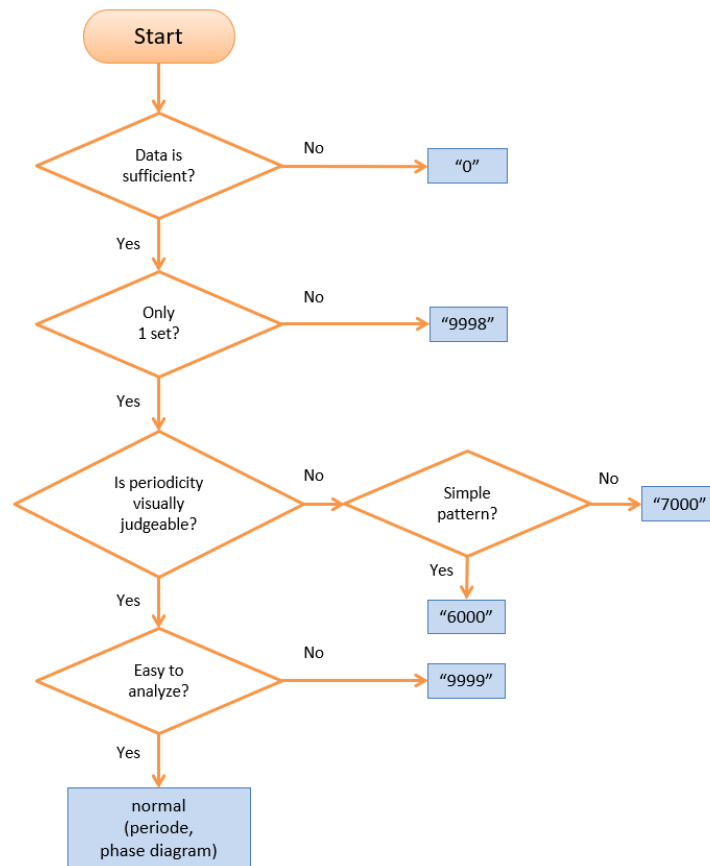
Figure 3.10.: Routine analysis of light curve data at AIUB.

ing than the case is labeled 9999 (means *unfinished*). Basically, how to extract a period of a light curve depends on the object historical attitude data. If the previous period data is not available then a set of parametric methods (which assume a specific distribution or parameters) are used to get the initial period value. In the case that previous period data is available, those data is used as the initial period value. The initial period value is subsequently used in one of the available non-parametric methods (which do not require any distribution) to get the final period. In addition to the apparent (synodic) spin period, a phase diagram[1] which is a plot constructed by folding the light curve using the obtained period value is also produced. The diagram can be used to study the morphology of the associated light curve. *Linder et al.* (2015) discusses advantages and disadvantages of several methods implemented at AIUB which are Fast Fourier Transformation (FFT), Periodogram analysis, Welch's method, Epoch folding, Lomb-Scargle periodogram, and Phase-diagram Reconstruction Method (PRM).

Since the photometric planning is performed on a daily basis so is the processing.

---

[1]The shape of phase diagram is a direct function of the object geometrical shape, its surface reflectivity properties, its alignment according to observer and the Sun (phase angle), and its orientation with respect to the observer.

This way, any necessary change in the planning due to a significant change in the attitude behavior as indicated by the last observation result can be immediately applied to the next observation. The daily processing will also notify the planner if there was a problem with the last observations so one or more observations should be repeated in the subsequent night. A problem could be insufficient data points or other things including the possibility that a wrong object has been observed. In addition, a processing of a whole night of an observation (typically consists of no less than 5 light curves) does not necessarily take too much time. Sometimes, it is no more than 5 minutes. We modified the existing main MATLAB script that is used to process the data to accommodate the flow of the routine analysis. However, processing a light curve also means taking care of its observer's remarks and consulting any unusual things that may happen regarding the observation. This activity can contribute significant time to the whole process.
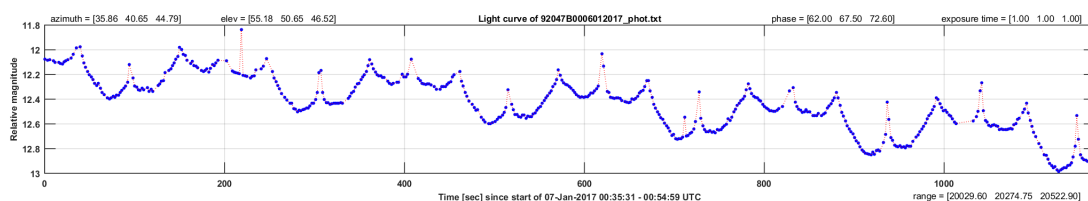
Figure 3.11.: An example of a light curve. The parameters embedded in the figure are explained in the text.

Fig. 3.11 shows an example of a light curve. Beside the object's relative magnitude as the main data, the figure also contains values of several parameters during the acquisition. All the parameters are given in three values: their value at the beginning, at the middle, and at the end of the observation. The azimuth, the elevation, and the phase angle are given in degree, the exposure time in second, while the range in km. A visual inspection can easily indicate that there is a repetition in the pattern with a period around 200 seconds. In fact, folding the light curve with time interval of 210.65 sec will nicely demonstrate that the object is currently rotating around its rotational axis with a periodicity of about that value (left side of Fig. 3.12). A complete process of the light curve which includes detrending by applying a second-order polynomial trend fit (see *Linder et al.* (2015)) will give the final phase diagram as shown on the right side of Fig. 3.12. This final result is obtained by using PRM which is always used to confirm all the processing results of light curves in the database (*Silha et al.*, 2018). The method is basically an iterative process that tries to find a period which gives the smallest dispersion points of a phase diagram starting with a specified value for the initial period. This method works on an interval of test periods centered at the initial period (obtained from other methods) and a step value which is designed to get smaller and smaller after each series of iteration. The step value will be used as an indicator of the accuracy. The type of phase reconstruction method implemented at AIUB is the one that uses image pixel value analysis. An example of the result using this technique is given in Fig. 3.13

which uses an inverted dispersion factor. A good result will show a profile with a nice symmetry around the abscissa of the peak as shown in the figure. The value of the abscissa represents the extracted spin period value.
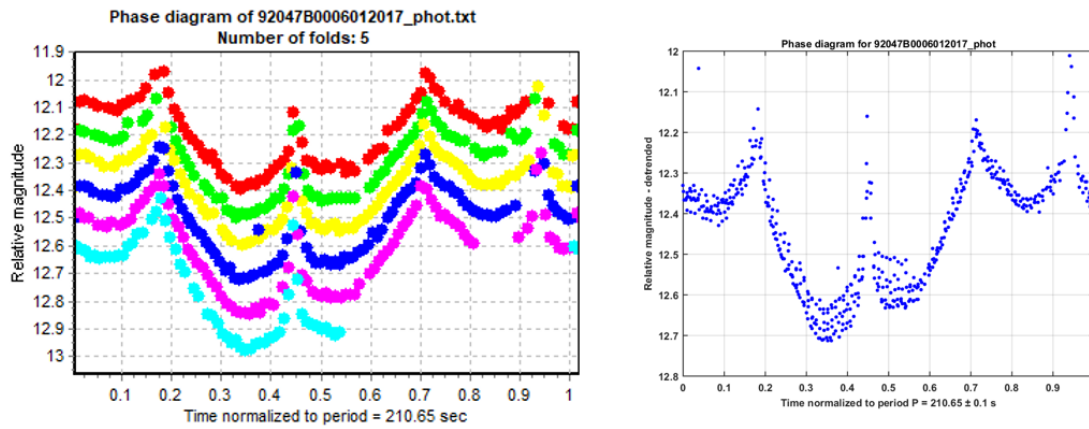
Figure 3.12.: An example of a provisional phase diagram (left image) and final phase diagram (right image) for the light curve given in Fig. 3.11 with minimum dispersion period of 210.65 ± 0.1s.
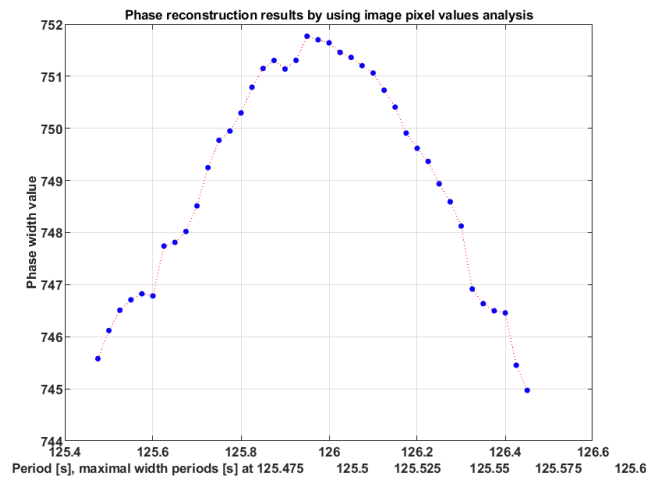
Figure 3.13.: An example of a phase reconstruction result with an extracted spin period around 126 sec. The vertical axis is given in pixel unit.

Sometimes a light curve consists of more than one set (or series) of data. Such light curves are labeled 9998 (Fig. 3.10) which will be decomposed first into several sets before each set is subsequently processed individually. Fig. 3.14 shows a light curve with two series of data. A light curve of several series opens a possibility to gain more insight into the attitude behavior of an object since it basically allows us to study several light curves of the same object which are only separated by a couple

of hours. From the figure we can see how the magnitude gets brighter during the acquisition (with constant exposure time of 1 sec) as the object moves closer (as indicated by the range parameter) and the phase angle gets smaller (as indicated by the phase parameter). By analyzing both the series and inspecting the resulted phase diagram, we can see that they are different in shape in which one tends to have sharper peaks while the spin period are basically the same. This indicates that the orientation of the object relative to the observer has been changed. Having more than one series in a light curve can also be useful in finding the period of a slow rotator (since individual series is limited to 20 min). The database contains more than 170 light curves with 9998-label which come from 108 different objects. The median of observation length of the whole set is around 2 hours.
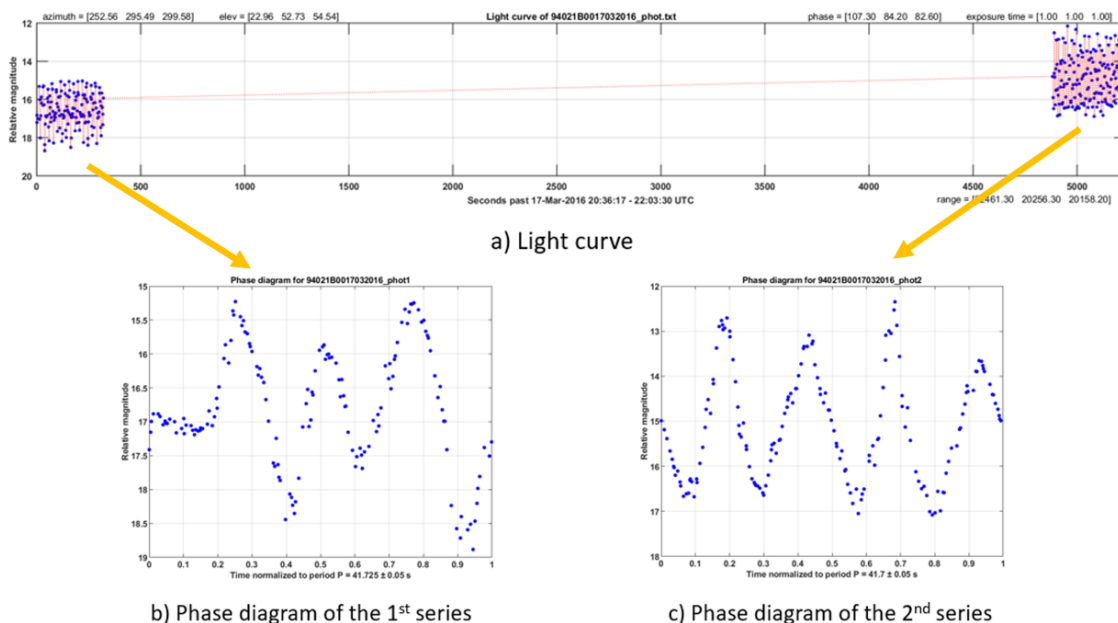
Figure 3.14.: An example of light curve with more than one series (top) and the associated phase diagrams (bottom).

Each object in the database that has been observed long enough will have a historical evolution of spin period as shown in Fig. 3.15. A spin period evolution is not only useful in allowing us to see how the spin period changes over time but also sometimes to correct or confirm a period value which is ambiguous. Through the latter, spin period evolution graphs sometimes have been used to complete previously unfinished light curve processes (the ones with 9999-label) by providing better initial periods, which is obtained from interpolation, for the PRM process. A feat that even a new method of extraction may not be able to achieve. We noticed that some objects in the database have spin period evolution that is so regular which opens a possibility to predict future periods through extrapolation based on the objects' historical data. In fact, the object in Fig. 3.15 is one of them. This will be discussed more in Section

3.5 when we are focusing on the spin rate evolution of inactive GLONASS satellites. In addition, spin period evolution graphs can also be used to estimate the period of slow rotator light curves by comparison with adjacent period values.
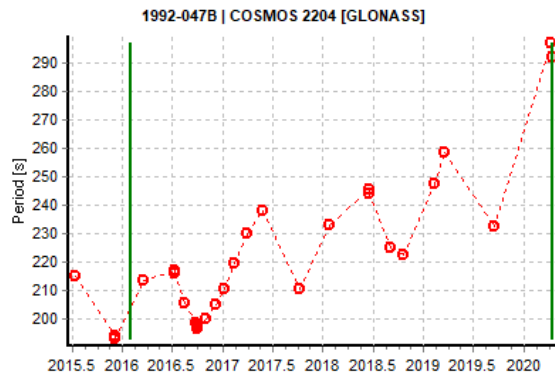
Figure 3.15.: An example of a spin period evolution graph. Red circles indicate periods, green lines indicate unfinished light curves.
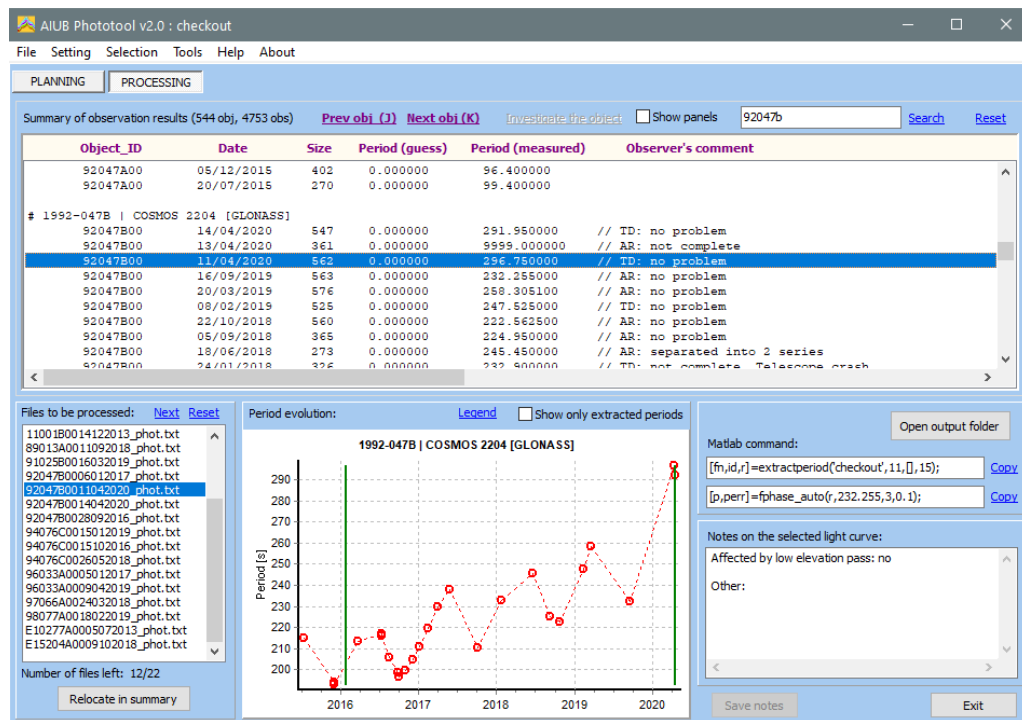
Figure 3.16.: User interface for the processing phase in AIUB Phototool (in checkout mode).

Similarly to the planning, AIUB Phototool is also used to simplify the processing of light curves while providing some useful features (Fig. 3.16). Since it provides

an interface to the database, an analyst who is processing a light curve can easily access previous processing results of the same object (including the provisional phase diagrams which can be created interactively and the final version) and the object's observation setting. The processing interface comes in four modes: 1) daily mode (used to process a single night observation data); 2) monthly mode (used to process a month of observation data); 3) checkout mode (used to process any light curve); and 4) investigation mode (used to process all light curve of a single object). The last mode is especially useful when analyzing the attitude behavior of an object in depth. A feature to calculate spin rate and statistics of a selected object and statistics of the current summary of observation results is also available (Fig. 3.17). The figure shows the range of spin rate for COSMOS 1988 based on its light curves in the database and some basic statistics. It also shows the statistics of the current summary which for this case contains all the 42 oscillating rotators in the database. Another feature which is also available is a feature to create a selection among objects and observations. A selection can be created by applying some filters or by defining a list. The list can be specified as a special group which is crucial in the planning phase.
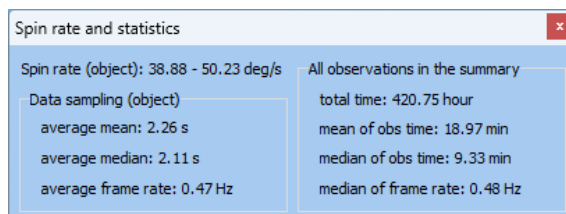
Figure 3.17.: A feature in AIUB Phototool to calculate spin rate and statistics of a selected object and statistics of current summary of observation results.

Fig. 3.18 shows an example of how to use the selection feature of AIUB Phototool to select only MEO oscillating payload rotators that meet some criteria. The left side of the figure shows that the example uses a file called summaryTable.txt which is created in advance (using the main menu View | summaryTable and statistics) based on a list of oscillating rotators. The list itself can be obtained by extracting only the oscillating rotators from the master summary table which consists of all objects in the database. The process starts by selecting the MEO payload cell and clicking the Apply button to run the first filter. The next step is selecting only the objects which contain periods from 10 until 50 seconds (this means that the objects can also possess other period values) while also limits to only objects which are still observed within the last one year and have minimum 30 observations. All these constraints are applied after the second Apply button is clicked. The last filter is selecting only observations of the previously selected objects which have minimum 20 data points and period value within 0 until 9999. The last constraint basically means that we want to display all the suitable observations of the previously selected objects except the ones that do not have sufficient data points (-1 label). Both the constraints are

applied after the third Apply button is clicked. The right side of the figure shows the list resulted from the filtering (8 objects with 383 observations). The list is given a group name ("Selected MEO oscillating rotators") and is labeled as a special group which will be displayed in the Light curve image panel window (as seen in Fig. 3.3) whenever a member of the group is selected (manually or automatically). The information can be used to manually put the selected object to a higher priority in the observation schedule if necessary when doing a planning.
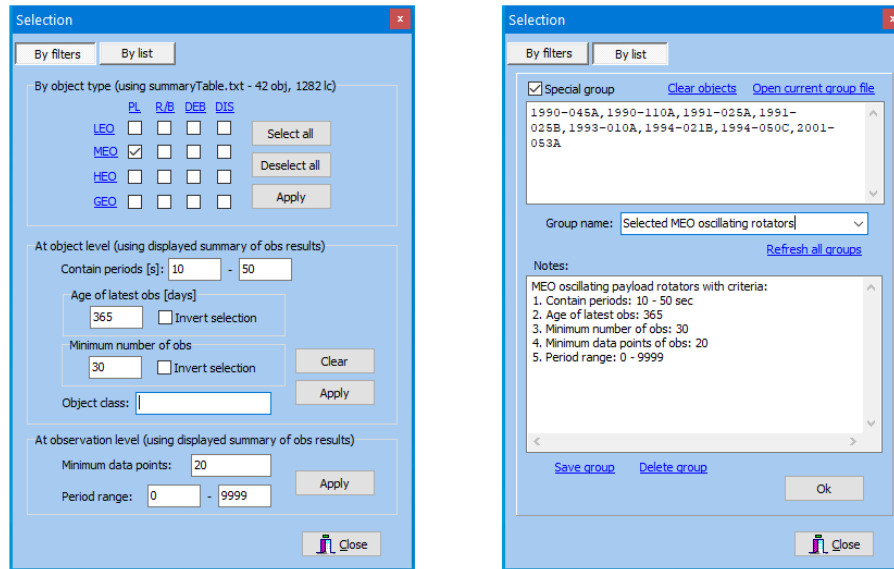
Figure 3.18.: An example of how to use the selection feature of AIUB Phototool. A list of objects can be written manually (right image) or created by using several filters (left image).

Another feature which is also supported in AIUB Phototool is the manual iteration to get the extracted spin period from a light curve. The automatic iteration to find the best spin period using PRM which is implemented in the MATLAB script occasionally fails in delivering the best period. This could happen with light curves with less data points due to short time series lengths such as the one shown in Fig. 3.19. In this case, the time series length is only 5 minutes which is actually the typical value for the object. Therefore, with a frame rate of 0.46 Hz the observation only produces 140 data points. However, with the period value around 32 sec, PRM can still give 9 folds which is usually enough. Unfortunately for this case, the method was unable to produce a nice phase diagram as can be seen in Fig. 3.20. We can also judge how bad the original result by inspecting the phase reconstruction result whose profile is far from a symmetry around the extracted period. The figure also illustrates how to get a solution for such cases by using the manual iteration with the *connector lines* displayed. For this case, manual iterations using arrow keys in the keyboard (for higher precision) successfully produced a much better phase diagram in which the extracted period differs almost 0.2 sec from the original.

Figure 3.19.: An example of light curve for the manual iteration supported in AIUB Phototool.
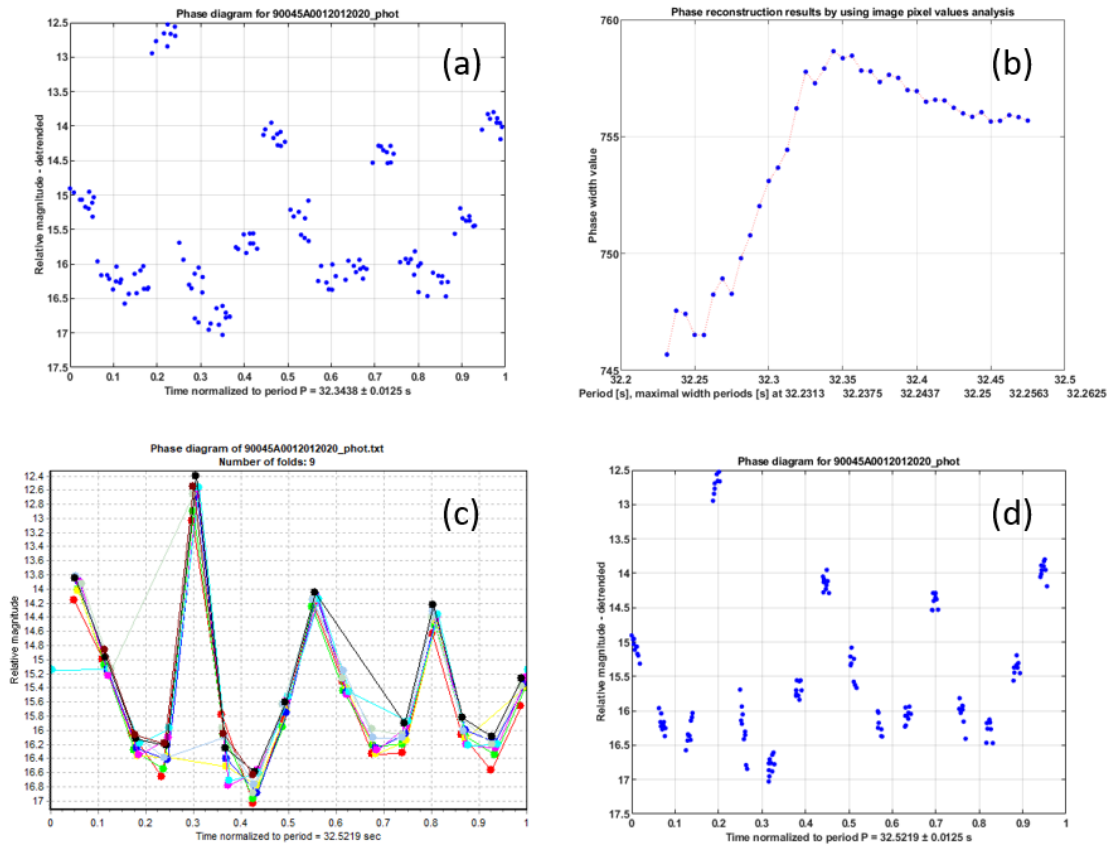
Figure 3.20.: An example of how the manual iteration supported in AIUB Phototool helps in getting better extracted periods. a) The original phase diagram; b) The phase reconstruction result; c) The result of manual iteration using connector line; d) The final phase diagram.

3.4. Current state of the database

The AIUB light curve database currently (per November 2020) contains around 4,800 light curves from 544 *selected space objects* from all orbital regions around

the Earth and different types of objects. Therefore the statistics presenting here is intended to describe the nature of the database itself instead of that of our space environment. The method used for classifying the attitude behavior of the members and its evolution follows that in *Rachman et al.* (2017). However, here we first skipped out light curves which have less than 10 data points so we only need to process 492 objects with a total of 4315 light curves. This approach may increase the quality of the analysis as it will decrease the number of unknown objects in terms of attitude behavior due to insufficient data points. While nearly 500 objects exist in the database, more than 50% of them were only observed for less than one year as can be seen on the right side of Fig. 3.21 where we can see that there are 249 objects that have been observed within one year.[2] Furthermore as the left side of the figure shows, if we consider only objects which have more than 30 observations then there are only 23 objects which satisfy the condition. All these suggest that doing satellite attitude evolution study which should consist of several years with the database is rather limited.[3]
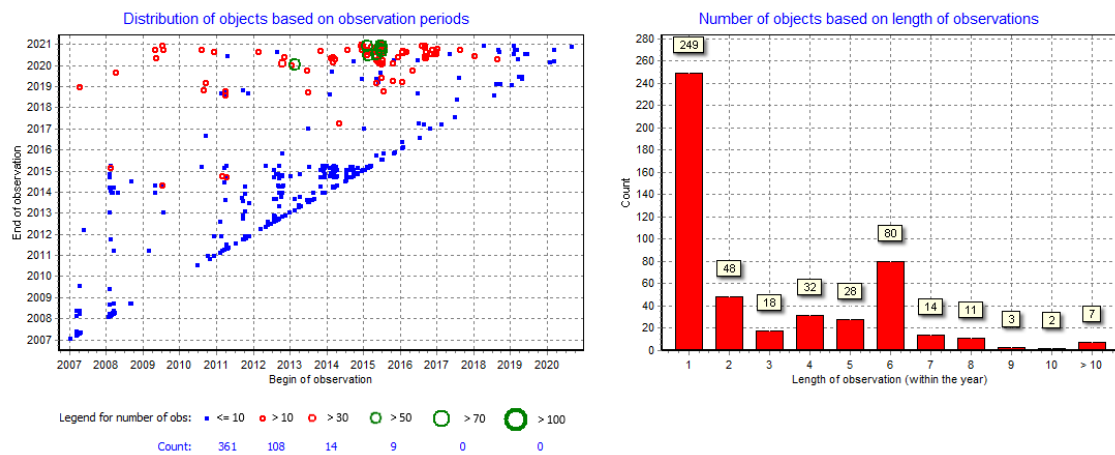
Figure 3.21.: Temporal distribution of observations based on observation periods (left image) and based on length of observations (right image).

The database is divided into four orbital groups and four object groups. The first orbital group is the low Earth orbit (LEO) which has a mean altitude below 2000 km from the Earth's surface and a low eccentricity. The second is the medium Earth orbit (MEO) which is located at around 20,000 km altitude and has a low eccentricity. This orbit is typically used by navigation satellites such as GLONASS and GPS constellation. The third is the high eccentric orbit (HEO) which has an eccentricity above 0.2. The last one is the geosynchronous Earth orbit and other orbits which are any type of orbits not covered by any of the previous three groups

---

[2]Another example of how to read the chart is that 80 objects have been observed within 5 and 6 years.

[3]This issue will be further discussed in Section 3.5.

(GEO/other). The first object group is the payload (PL) which is usually a box-wing type of object with one or two solar panels attached to the main bus. The second is the rocket body (R/B) which typically has a cylindrical-like shape. The third is the debris which is either mission-related or fragmentation debris. The last one is the DIS group for objects discovered during ESA's GEO, GTO, and Molniya surveys. Origin of DIS, compared with the other groups, is unknown.
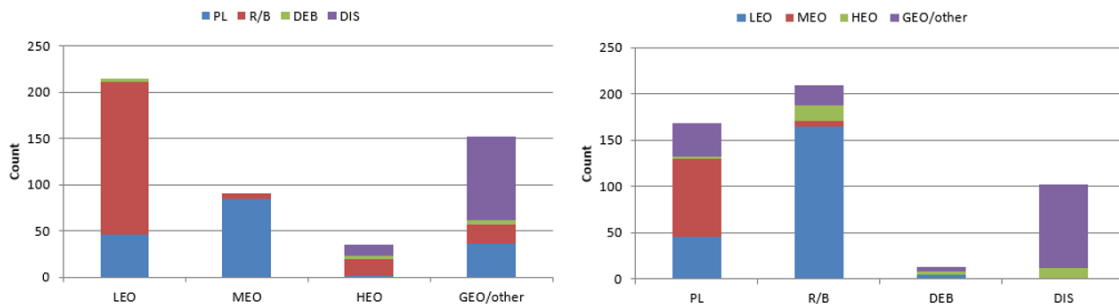
Figure 3.22.: Current number of objects in the AIUB light curve database based primarily on their orbit type and object type (left image) and primarily on object type and orbit type (right image).

Left side of Fig. 3.22 shows that LEO objects are the biggest constituent of the database (43.7%) followed by GEO/other object (30.9%) then MEO and HEO objects (18.3% and 7.1% respectively). The right side of the figure shows that most of the observed objects are rocket bodies followed by payloads, discovered objects, and debris. In fact, from the left side of the figure we can see that most of the LEO objects in the database are rocket bodies (76.7%), most of MEO objects are payloads (93.3%), most of HEO objects are rocket bodies (48.6%), and most of GEO/other objects are discovered objects (59.2%). The figure also shows that payloads and rocket bodies are observed in all orbital regimes while debris are only in LEO, HEO, and GEO; discovered objects are only in HEO and GEO/other. Regarding debris, we can see from the figure that its portion in the database is only a small fraction of the others.

To assess an object's attitude state evolution, we visually inspected its history of light curve processing results recorded in the database. Based on the assessment, we decided whether the object belongs to one of four attitude groups: *rotator group* (R), *slow rotator group* (SR), *stable group* (S), or *unknown group* (U). In general, an object which has at least one rotator light curve in its history is considered as a rotator. It is still a rotator even if it has several slow rotator light curves and even stable light curves within its lifetime (e.g. see Fig. 3.23). The slow rotator normally takes precedence over the stable which means that if the number of *slow rotating light curves* is the same as that of *stable light curves* for an object, then the object will be considered as a slow rotator. Only if an object has considerably large percentage of stable light curves than slow rotator light curves than it is considered

as a stable object. Unknown attitude state evolution of an object could be the result of three factors: 1) low quality data (not enough data available from observations); 2) light curves need further processing; 3) light curves are not yet processed.
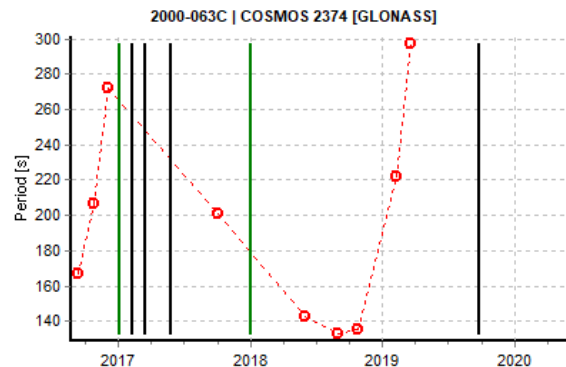
Figure 3.23.: An example of a rotator with several slow rotator light curves within its lifetime. Red circles indicate periods, black lines indicate slow rotator light curves, and green lines indicates unfinished light curves.

Rotators possessed the biggest portion in the database compared with other attitude groups. We found that 187 out of the 492 objects which means 38% are rotators. These objects are located in all orbital groups together with slow rotators and unknown attitude objects while stable objects were not found in HEO as shown on the left side of Fig. 3.24. The portion of slow rotators and stable objects were pretty much the same which are 24.2% and 26.6% respectively while the unknown group had the smallest portion (11.2%). The largest number of rotators is located in the GEO/other which is 78 (out of 152 rotators which means 51.3%) but the largest percentage was located in the MEO which is 80% (72 out of 90 rotators). The right side of the figure shows that most of the rotators are payloads (54%) while slow rotators and stable objects are mainly rocket bodies (50.4% and 75.6% respectively). It also shows that most of the unknown attitude objects are discovered objects (61.8%). The reason for the latter is because 40% of them (42 out of 102 DIS objects) only were observed a couple of times (less than 3 light curves available) which makes it difficult for the assessment.

Better insights into the database can be obtained by showing how all the objects are distributed according to their attitude type, orbit type, and object type as shown in Fig. 3.25. Overall, we can see that rotator is indeed the biggest contributor of the database even though the highest count of specific orbit and type is not from the group. Moreover, it can be clearly seen that payload in MEO is the main contributor of the rotator group (35.8%), rocket-body in LEO is that of the slow rotator group (47.9%), rocket-body in LEO is also that of the stable group (75.6%), and discovered objects in GEO is that of the unknown group (45.5%). The high number of slow rotator and stable LEO rocket bodies in contrast with the general trend (which is dominated by rotator), somehow reflects the idea that rocket bodies
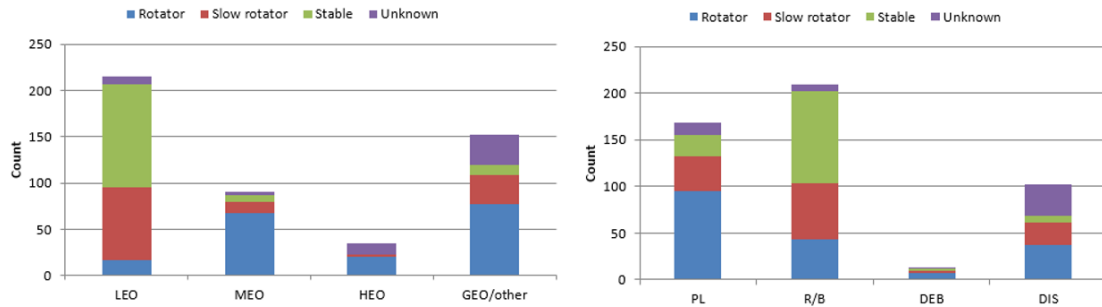
Figure 3.24.: Current number of objects in the AIUB light curve database based primarily on orbit type and attitude type (left image) and primarily on object type and attitude type (right image).

in LEO experience a decay in their spin period (which is mainly due to eddy current torque (*Lin et al.*, 2019)).

		LEO	MEO	HEO	GEO	LEO	MEO	HEO	GEO	LEO	MEO	HEO	GEO	LEO	MEO	HEO	GEO
		ROTATOR				SLOW ROTATOR				STABLE				UNKNOWN			
■	PL	11	67	1	22	20	8	0	4	11	7	0	4	4	2	1	6
■	R/B	5	5	14	19	57	0	1	2	99	0	0	0	4	1	2	0
■	DEB	0	0	3	3	1	0	1	1	3	0	0	0	0	0	0	1
■	DIS	0	0	3	34	0	0	0	24	0	0	0	7	0	0	9	25
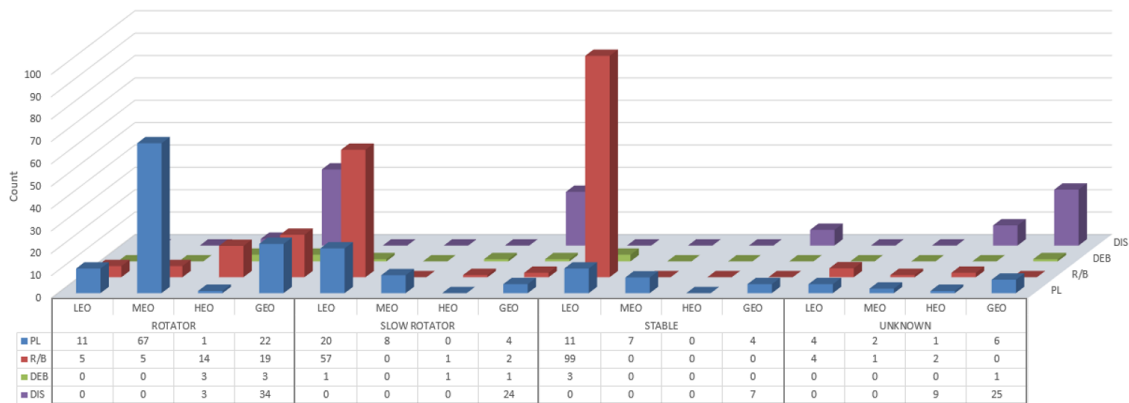
Figure 3.25.: Distribution of objects in the AIUB light curve database based on their attitude type, orbit type, and object type.

Perhaps the most notable feature we can see from Fig. 3.25 is the significantly high count of stable LEO rocket bodies. However, we found out that the median duration of observation of all light curves from this 99 objects is only 3.86 min which is significantly lower than that of slow rotator rocket bodies which is 4.32 min. Therefore, some of the stable objects are probably just slow rotators but appear stable due to the shorter duration of observation. Other notable feature is the high count of rotating MEO payloads. Most of the member of this group are GLONASS satellites (70 out of 84 objects which is 83%). Further investigation on MEO objects in the database revealed that nearly all of them are rotating. In fact, out of seven "stable" MEO payloads (see the table in Fig. 3.25) only one object is really stable by the definition used in the database.

We performed another visual inspection to assess the pattern in the period evolution

of the rotating objects. The result shows us that there are three general patterns: *oscillating*, *increasing*, and *decreasing* (*Rachman et al.*, 2017). Therefore we classified four groups: three for each of the identified patterns and one group which is called *common rotators* to accommodate the rest of rotating objects with unknown trends. Unknown trends can be resulted from insufficient number of observations or insufficient number of successful period extractions. Inside the database, there are 42 oscillating rotators, 12 increasing rotators, 26 decreasing rotators, and 107 common rotators. Fig. 3.26 shows an example of each of the rotator groups. Notice that for the case of common rotator, the figure demonstrate an example where the number of successful period extractions is too small even though the number of observations (which is 41) is moderate. Oscillating rotators appear to display a similar pattern which consists of linear segments and abrupt changes (to some degree) in its spin period evolution that form a series of triangular shapes as shown in the figure.
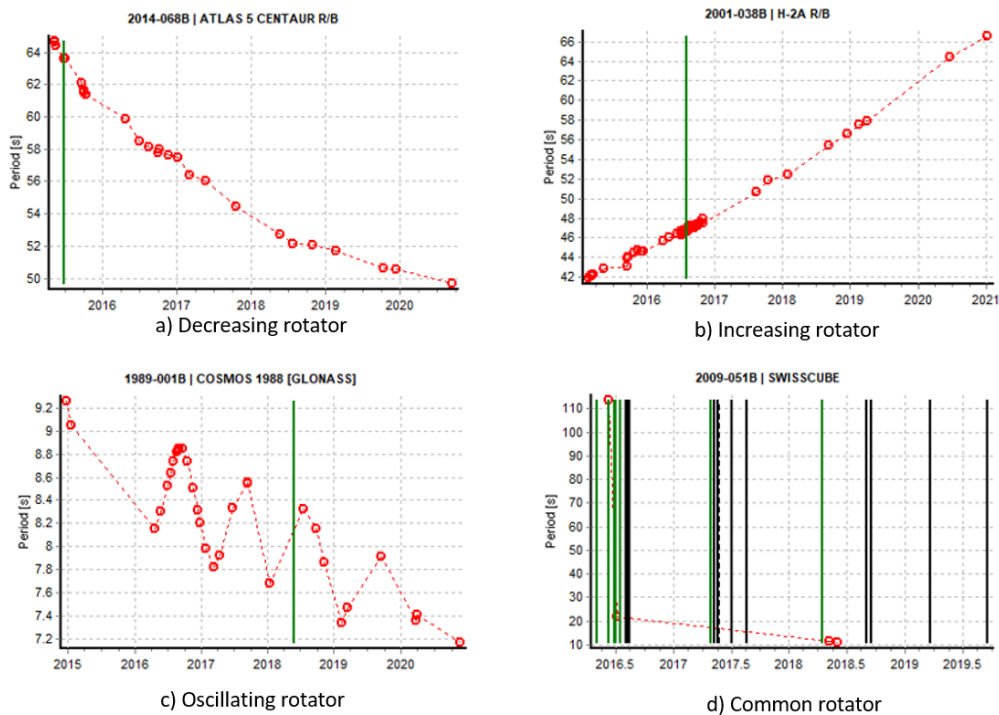
Figure 3.26.: An example of each of the rotator groups in the AIUB light curve database. Red circles indicate periods, black lines indicate slow rotator light curves, black dash lines indicate stable light curves, and green lines indicates unfinished light curves.

Almost all of the oscillating rotators (42 objects) are found in MEO payloads while other groups shows no such preferences as Fig. 3.27 shows. *Rachman et al.* (2018) also found out that all the MEO payload oscillating rotators are GLONASS satellites while the other oscillating rotator is a BREEZE-M rocket body which is located in GEO. Comparatively, increasing rotators are 4 payloads and 8 rocket bodies while

decreasing rotators are 13 payloads, 5 rocket bodies, and 8 discovered objects. The increasing and decreasing rotators are located in various orbital regions. It is also clear from the right side of the figure that most of rotators in the database are payloads followed by rocket bodies, discovered objects, and debris. Most of them are located in GEO and MEO regions as can be seen on left side of the figure. *Rachman et al.* (2018) also found that, generally, the change of angular velocity per year of all the oscillating, increasing, and decreasing rotators are within 1°/s and there is no correlation between the change of angular velocity and the average of periods. Overall, we found it difficult to find the pattern in the database since usually there are not enough data points to reveal it. If we consider only rotators which have minimum 20 observations then in GEO there are only 6 of them (out of 78 rotators); in HEO only 8 (out of 21); in MEO only 52 (out of 72); and in LEO only 6 (out of 16).
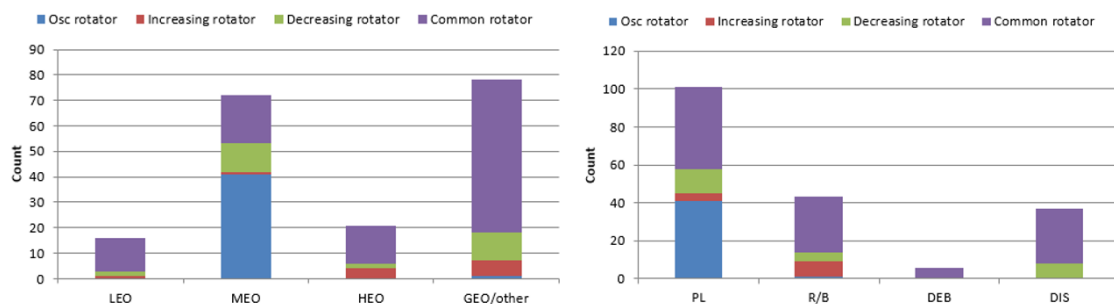
Figure 3.27.: Current number of rotator in the AIUB light curve database based primarily on orbit type and attitude evolution type (left image) and object type and attitude evolution type (right image).

Fig. 3.28 shows how all the rotators distributed according to their attitude evolution type, orbital region, and object type. It is clear from the figure (especially if we ignore the substantially high count of oscillating MEO rotators) that most of them are common rotators with GEO region being the most favorable location. The reason for this seems mainly because there is not enough data to identify their period evolution pattern due to the small number of observations per object and the short period of observations. Almost all common rotators (95%) have less than 30 observations and more than 65% of them have less than 5 years of observation time. As a comparison, only 64% of oscillating rotators have less than 30 observations and 90% of them have been observed for at least 6 years. Again, as we have noticed before, the most significant feature that we can see from the figure is the number of oscillating MEO payload rotators with 41 objects.

Further investigation revealed that if we consider only payloads, all the 36 GEO payloads have less than 30 observations, 100% of that for HEO (2 objects), 81% of that for MEO (84 objects), and 93% of that for LEO (46 objects). If we consider only rocket bodies, all the 21 GEO payloads have less than 30 observations, 76% of that for HEO (17 objects), similar with that for MEO and LEO (6 objects and 165 objects,
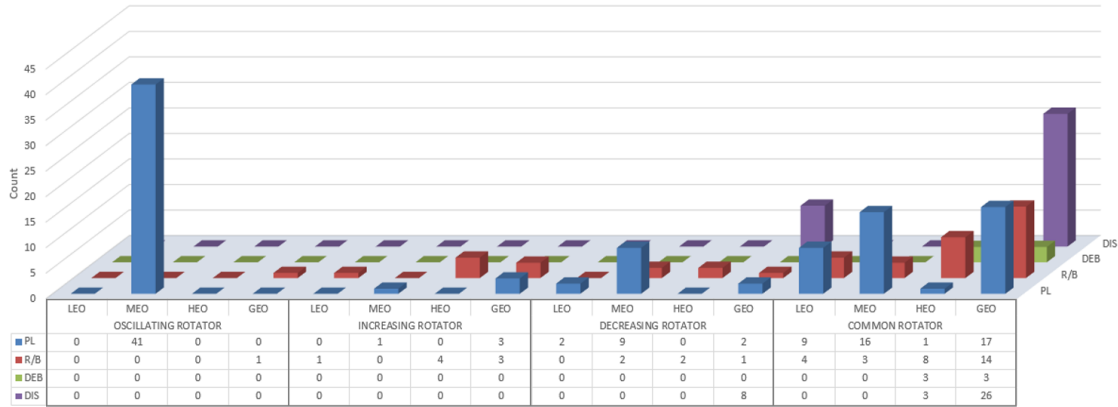
Figure 3.28.: Current number of objects in the AIUB light curve database based on their attitude evolution type, orbit type, and object type.

respectively). All debris and discovered objects have less than 30 observations. Therefore, in terms of number of observations per object, generally MEO payloads and HEO rocket bodies have better observability in the database.

Table 3.1 summarizes the attitude state dominance in terms of orbital regions and object types in the database. We have already noticed some of the content of the table in the previous paragraphs, e.g. rotator dominates all orbital regions in the database except the LEO region in which slow rotator dominates payloads and stable object dominates rocket bodies. In addition to show us the general situation of the database, the table also provides us information on the availability of rotating RSOs in the database as a factor of orbital region and orbit type. For example, it let us know that per November 2020, only 5 rotating LEO rocket bodies are available in the database, the same number for rotating MEO rocket bodies, however, 67 rotating MEO payloads and 34 rotating discovered objects are available. This kind of information can benefit anybody who wants to use the database for studying the attitude behavior of RSOs.

Table 3.1.: Attitude state dominance as a function of object type and orbital region in the AIUB light curve database. Here R means rotator, SR slow rotator, and S stable object. The ones with an asterisk mean that they are also the dominance attitude state within the specified orbital region. Numbers in brackets are the number of rotators for the specified object type and orbital region.

Type	LEO	MEO	HEO	GEO
PL	SR (11)	R* (67)	-	R (22)
R/B	S* (5)	R (5)	R* (14)	R (19)
DEB	-	-	R (3)	R (3)
DIS	-	-	R (3)	R* (34)

Within the database, objects' spin periods vary from less than 1 sec to nearly 1500 sec (25 min) as can be seen in Table 3.2. We found that the fastest spin rate belongs to a rocket body named BREEZE-M R/B (COSPAR ID 2015-075B) with a period of 0.88 sec (spin rate equals 410.26°/s) while the slowest belongs to a payload named COSMOS 2473 (COSPAR ID 2011-048A) with a period of 1480.51 sec (spin rate equals 0.24°/s). Both these objects are located in GEO. The BREEZE-M R/B is a small rocket body based on its radar cross section in Space-Track website (`www.space-track.org`) which has been observed since 2016. While COSMOS 2473 is a large payload which was only recently observed.

Table 3.2.: Minimum and maximum apparent spin periods ($P_{a, min}$, $P_{a, max}$) of rotating objects in the AIUB light curve database based on orbital region and object type. Each value is marked with object type or orbital region.

	Region			Type	
	$P_{a, min}$ [s]	$P_{a, max}$ [s]		$P_{a, min}$ [s]	$P_{a, max}$ [s]
LEO	5.09 (R/B)	191.00 (PL)	PL	1.55 (GEO)	1480.51 (GEO)
MEO	1.52 (R/B)	782.65 (PL)	R/B	0.88 (GEO)	209.28 (HEO)
HEO	1.28 (R/B)	859.35 (PL)	DEB	9.99 (GEO)	340.30 (HEO)
GEO	0.88 (R/B)	1480.51 (PL)	DIS	1.22 (GEO)	850.50 (GEO)

In LEO region, the minimum spin period belongs to a rocket body named N-1 R/B (COSPAR ID 1978-018B) which is 5.09 sec (Table 3.2). Its observations since 2014 until 2020 yield 17 light curves with an average median of data sampling of 1.45 sec and an average frame rate of 0.33 Hz. Spin rate of this increasing rotator is ranging from 55.05°/s to 70.7°/s. The maximum spin period in the orbital region belongs to a payload named ENVISAT (COSPAR ID 2002-009A)[4] which is 191.00 sec. Its observations since 2014 until 2017 yield 25 light curves with an average median of data sampling of 1.19 sec and an average frame rate of 0.65 Hz. Spin rate of this sun-synchronous rotator is ranging from 1.88°/s to 1.96°/s.

In MEO region, the minimum spin period belongs to a rocket body named FREGAT R/B (COSPAR ID 2014-032B) which is 1.52 sec (Table 3.2). Its observations since 2014 until 2020 yield 28 light curves with an average median of data sampling of 1.69 sec and an average frame rate of 0.55 Hz. Spin rate of this rotator is ranging from 232.74°/s to 236.59°/s. The maximum spin period in the orbital region belongs to a GLONASS satellite named COSMOS 2275 (COSPAR ID 1994-021C) which is 782.65 sec (Table 3.2). Its observations since 2015 until 2020 yield 54 light curves with an average median of data sampling of 2.03 sec and an average frame rate of 0.44 Hz. Spin rate of this oscillating rotator is ranging from 0.46°/s to 5.42°/s.

---

[4]This object is one of ESA's main target for its future active debris removal mission due to its enormous size and mass.

In HEO region, the minimum spin period belongs to a rocket body named BREEZE-M R/B (COSPAR ID 2015-060B) which is 1.28 sec (Table 3.2). Its observations since 2016 until 2020 yield 33 light curves with an average median of data sampling of 1.69 sec and an average frame rate of 0.52 Hz. Spin rate of this increasing rotator is ranging from 277.56°/s to 280.83°/s. The maximum spin period in the orbital region belongs to a payload named MAQSAT H (COSPAR ID 1997-066A) which is 859.35 sec (Table 3.2). Its observations since 2018 until 2020 yield 11 light curves with an average median of data sampling of 2.00 sec and an average frame rate of 0.48 Hz. Spin rate of this rotator is ranging from 0.40°/s to 0.44°/s.

In GEO region, the minimum spin period belongs to a rocket body named BREEZE-M R/B (COSPAR ID 2015-075B) which is 0.88 sec (Table 3.2). This is the lowest spin period in the database as mentioned before. Its observations since 2016 until 2019 yield 28 light curves with an average median of data sampling of 1.72 sec and an average frame rate of 0.55 Hz. Spin rate of this oscillating rotator is ranging from 394.33°/s to 410.26°/s and it is the only oscillating rotator we found in GEO. The maximum spin period in the orbital region belongs to a satellite named COSMOS 2473 (COSPAR ID 2011-048A) which is 1480.51 sec (Table 3.2). This is the highest spin period in the database as also mentioned before. Observations of this object were only performed in 2020 which yield 4 light curves with an average median of data sampling of 2.00 sec and an average frame rate of 0.39 Hz. For this object, so far, we don't have the range of spin rate since there are only one value available which is 0.24°/s obtained from a special (much longer) observation. Normally for this object, all of its light curves are labeled 7000 for slow rotators. However, in one of the night of September 2020 we decided to take three series of 20 minutes each of observation to allow us to get the period. Fig. 3.29 shows the associated light curve.
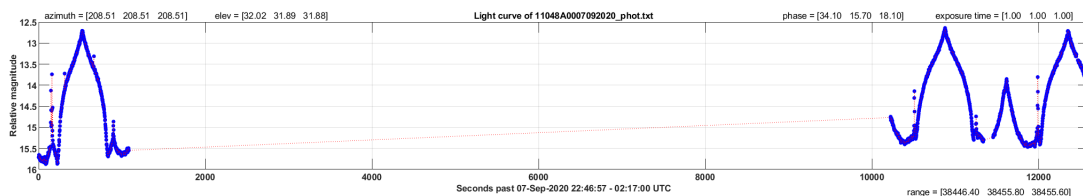
Figure 3.29.: A light curve of COSMOS 2473.

Details regarding minimum and maximum apparent spin periods in each orbital region based on object type are provided in Table 3.3 and Table 3.4. By comparing median values of spin periods in the table we can see that most of rocket bodies (in the database) are very fast rotators. In all regions except HEO, their spin periods are less than 7 sec (spin rates are more than 51.4°/s). In HEO region, rocket bodies are also the fastest among objects of different types with a median periods of 43.10 sec. On the other hand, payloads are more distributed in terms of spin period. Fastest payloads are mostly found in LEO with a median periods of 11.58 sec (median value of spin rates is 31.09°/s) while the slower ones are mostly found in MEO and GEO.

Although we see from the table that the highest median value for payloads is found in HEO with 820 sec, actually it originates from only one object (which is MAQSAT H with COSPAR ID 1997-066A).

Table 3.3.: Minimum and maximum apparent spin periods ($P_{a, min}$,$P_{a, max}$) of rotating LEO and MEO objects in the AIUB light curve database based on object type. Numbers in brackets in the last column are the number of light curves for the specified object type.

	LEO			MEO		
Type	$P_{a, min}$ [s]	$P_{a, max}$ [s]	Median [s]	$P_{a, min}$ [s]	$P_{a, max}$ [s]	Median [s]
PL	9.74	191.00	11.58 (97)	2.22	782.65	80.40 (1457)
R/B	5.09	73.60	6.39 (16)	1.52	64.70	6.41 (96)
DEB	-	-	-	-	-	-
DIS	-	-	-	-	-	-

Table 3.4.: Minimum and maximum apparent spin periods ($P_{a, min}$,$P_{a, max}$) of rotating HEO and GEO objects in the AIUB light curve database based on object type. Numbers in brackets in the last column are the number of light curves for the specified object type.

	HEO			GEO		
Type	$P_{a, min}$ [s]	$P_{a, max}$ [s]	Median [s]	$P_{a, min}$ [s]	$P_{a, max}$ [s]	Median [s]
PL	810.68	859.35	820.33 (4)	1.55	1480.51	97.70 (91)
R/B	1.28	209.28	43.10 (243)	0.88	131.50	6.56 (142)
DEB	89.50	340.30	112.28 (27)	9.99	12.95	9.99 (4)
DIS	45.80	224.18	80.07 (8)	1.22	850.50	62.32 (139)

3.5. Inactive GLONASS satellites

This section will specifically discuss about inactive GLONASS satellites as the main subject of this study.

The first successful observation of inactive GLONASS satellites by AIUB was conducted in 2009. However, the majority of the data available now in the AIUB light curve database is obtained only after 2015 as shown on the left side of Fig. 3.30. The reason is simply because the special campaign for inactive GLONASS satellites was started during the spring and summer 2015. The campaign was performed after the

CODE (Center for Orbit Determination in Europe) center identified 70 GLONASS satellites from GLONASS global navigation system that are already decommissioned (*Linder et al.*, 2015). There are only two light curves before 2014 which mark the start of the observation for the two objects we see in the figure (in 2009 and 2012) and they are basically of insufficient data points. Inspecting further into the chart, we can see that most of the objects have less than 50 observations. There are even three objects that have 10 observations in maximum (two of them are not visible in the chart). In fact, only five objects have more than 50 observations. Given that most of the 70 objects have been observed for at least five years (as shown on the right side of Fig. 3.30, this means that ideally, on average, each object should have at least 60 observations (to have one observation per month which is considered as an ideal situation).
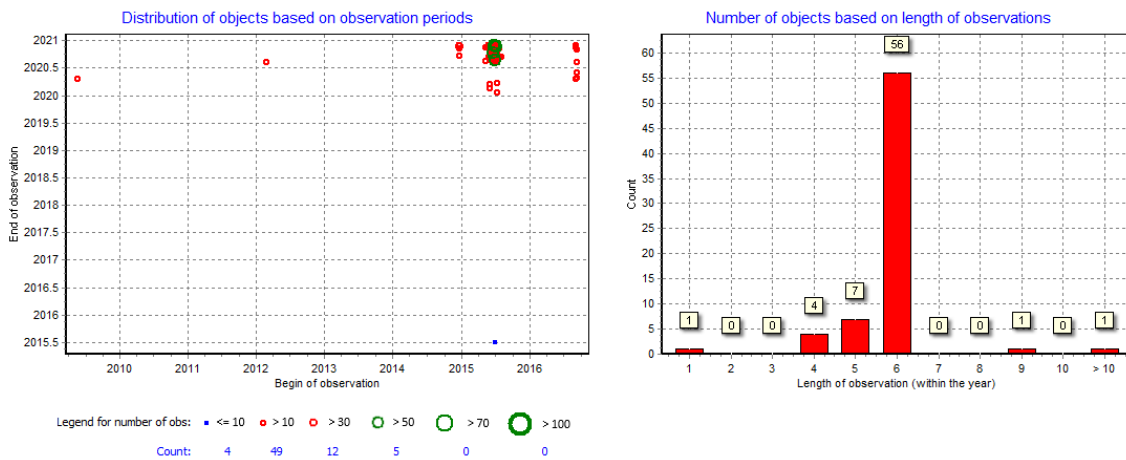
Figure 3.30.: Temporal distribution of observations of inactive GLONASS satellites in the AIUB light curve database based on observation periods (left image) and based on length of observations (right image).

During data acquisition, GLONASS satellites are typically observed using an exposure time of 1 second and no filter. As of November 2020, the database contains over 1800 light curves representing 70 members of the group. These light curves collectively amount to more than 540 hours of observations, with a median duration of 9.59 minutes per observation. The median frame rate for these observations is 0.48 Hz. Using the year of 2015 as the effective start of the observations, we can calculate that, on average, 10 inactive GLONASS satellites were observed every 13 days in the last 6 years. By comparing the total time of observations which has been spent specially for inactive GLONASS satellites and that of the whole member of the database, we found out that the group occupies around 25% of the whole observation time. Regarding the satellites themselves, fifty one of them (75%) are first generation GLONASS (block IIv) while the rest are GLONASS-M satellites. The satellites were launched between 1989 until 2011. On average, they have become debris for more than 10 years when they were first observed by AIUB (more than

20 years among 20% of the group).

The result of processing all the light curves reveals many things. About 83% of them are normal light curves (whose periods can be obtained "relatively easy" and, as a result, their phase diagrams are available) (Fig. 3.31), about 3% are stable light curves (Fig. 3.32), about 10% are slow rotator light curves (Fig. 3.33), and about 4% are unfinished light curves (due to complex attitude motions of the associated objects or other reasons) (Fig. 3.34). Interchanging between light curve types during a satellite's orbital lifetime happens many times especially between normal and slow rotator light curves when the periods are becoming too large for a successful extraction. On the other side, we found only one object which has *justifiable* stable light curves after normal. By *justifiable* we mean that the light curves are produced from relatively long duration of observation with enough data points to represent a stable behavior (at least during the acquisition time). We also only found one object which is stable although it has become a debris for at least 7 years. These three interesting cases will be discussed more at the end of this section. In addition, we found that 21 light curves which come from 14 different objects have more than one series. The median of observation length of the whole set is nearly 1.5 hours.
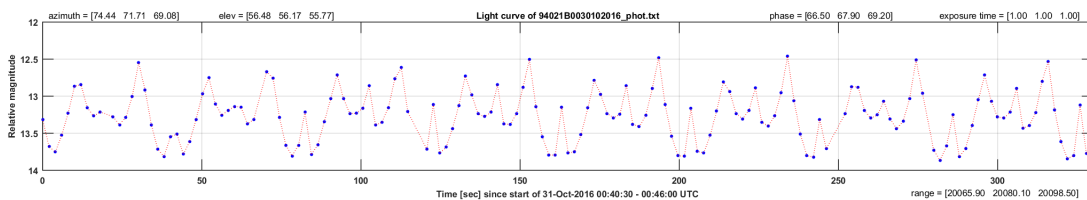
Figure 3.31.: An example of simple GLONASS light curve.
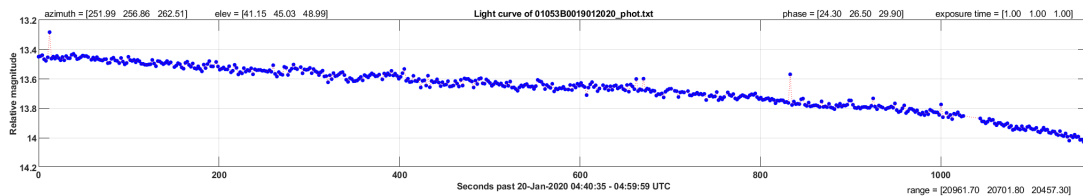
Figure 3.32.: An example of stable GLONASS light curve.
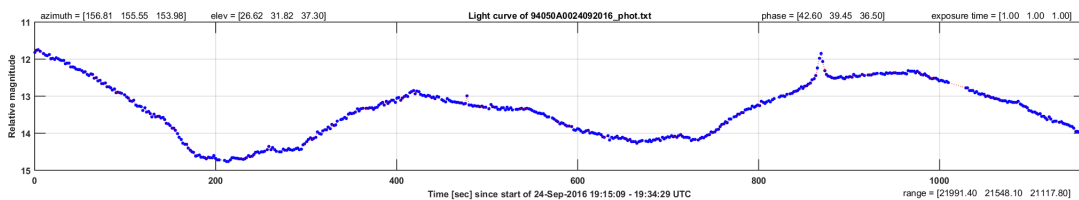
Figure 3.33.: An example of slow rotator GLONASS light curve.
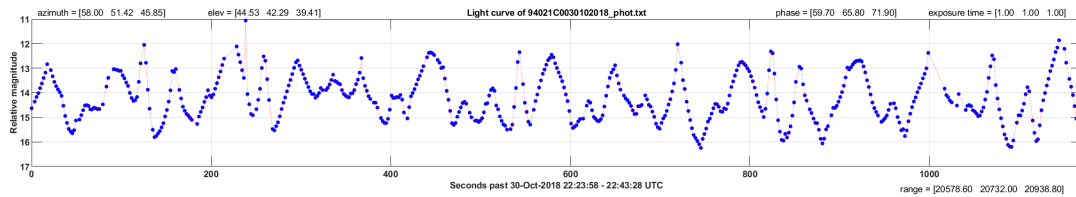
Figure 3.34.: An example of unfinished GLONASS light curve.

Fig. 3.34 shows an example of unfinished GLONASS light curve due to a complex attitude motion. Even though labeled as unfinished since the period cannot normally be extracted, we can estimate that the period is around 698 sec by manual iteration (conveniently supported in AIUB Phototool). A period with greater precision cannot be obtained since the length of observation is less than 20 min while the assumed period is around 11 min. The resulting phase diagram which is shown in Fig. 3.35 clearly demonstrates the repetition in the pattern despite the fact that it is not enough for a confirmed result. A high number of peaks (more than 10) for a light curve of a residence space object has also been found by *Benson et al.* (2018) when investigating the attitude behavior of GOES 8 satellite observed on 19 April 2018.[5] By selecting only observations with 9999-label with minimum 200 data points, candidates for such complex light curves can be found in the database which are 12 in number (for GLONASS satellites).
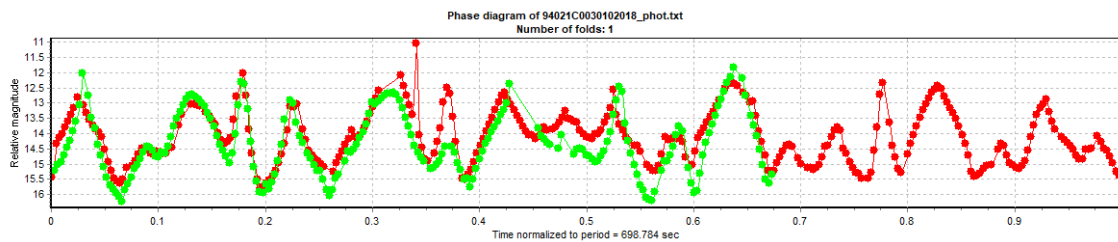
Figure 3.35.: Phase diagram of a complex GLONASS light curve given in Fig. 3.34.

From the previous section we know that all the MEO payload oscillating rotators (41 objects) are GLONASS satellites (see left side of Fig. 3.27). Special processing on inactive GLONASS satellites gives their complete distribution according to attitude state as given in Fig. 3.36. However, further investigation to each of the stable objects reveals that only one which is COSMOS 2449 (COSPAR ID 2008-067B) is really stable (at least during the 20 min of maximum acquisition time). The other two were actually observed when they were still operational.[6] COSMOS 2449 has 12 light curves in the database and nearly all of them were observed for almost 20

---

[5]The study of *Benson et al.* (2018) is reviewed in Section 2.4 of this study.

[6]These objects are COSMOS 2457 (COSPAR ID 2009-070B) and COSMOS 2464 (COSPAR ID 2010-041C).

min. The object was observed from June 2015 until March 2020. All the light curves are stable ones except the first one which is a slow rotator. It is important to note that after inspecting the whole group especially having at least 40 observations, we found an indication that the increasing, decreasing, and common inactive GLONASS satellites may also posses the oscillating pattern (not necessarily triangular) albeit subtle (very small in amplitude).
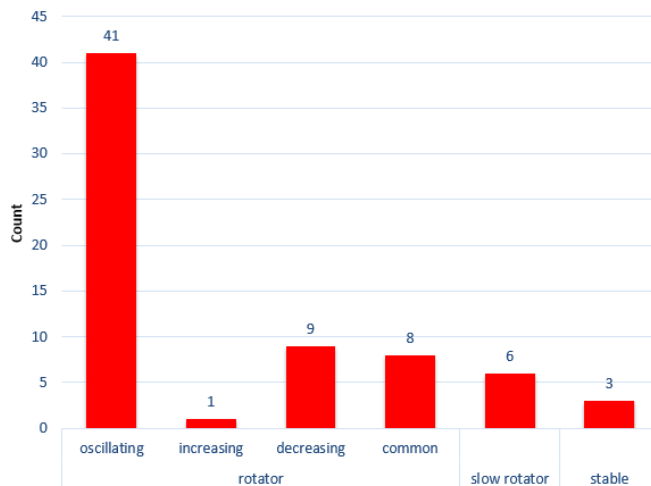
Figure 3.36.: Current number of inactive GLONASS satellites based on their attitude state.

Regarding the oscillating rotators, not all of the them clearly show the repeating triangular pattern which mostly due to lack of sufficient data points. *Rachman et al.* (2018) found that only 26 of GLONASS satellites in the database possess the feature. As already mentioned in the previous section, the oscillating rotators of GLONASS appear to display a similar pattern which consists of linear segments and abrupt changes (to some degrees) in its spin period evolution that form a series of triangular shapes. *Rachman et al.* (2018) also found that the absolute value for the slope (gradient) of all the segments of an oscillating rotator is roughly similar. In other words, in average, an object spin period rate of change is always the same during the repeated increasing or decreasing phase. In terms of angular velocity, this means that, on average, the value of its rate of change (which is the angular acceleration) is always the same during the two phases. Using this evidence, the latest analysis using updated data until November 2020 reveals that 18 out of the 26 objects maintain their triangular pattern (with different levels of confidence due to the number of observations available). Fig. 3.37 shows one example where the pattern obtained previously (*Rachman et al.*, 2018) can be successfully implemented until the last observational data. More on this will be discussed in the next chapter.

Cyclic patterns in spin period evolutions of inactive satellites have been found before and reported for example in *Earl* (2017) and *Kirchner et al.* (2017). However, we found that only a few of them show consistent series of peaks with triangular shape
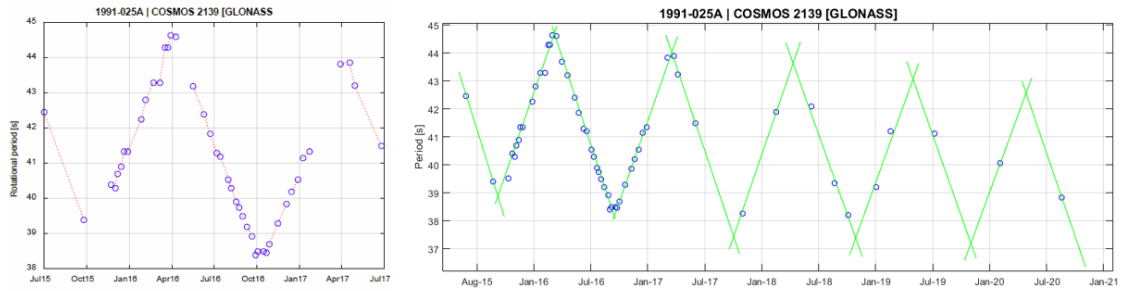
Figure 3.37.: An example of a spin period evolution of GLONASS satellites. The left image (taken from *Rachman et al.* (2018)) is the base for the empirical model which is used in the updated image on the right.

similar to that in the 18 cases of inactive GLONASS satellites from AIUB database. The period evolution for the latter group consistently shows linear segments with roughly abrupt changes at the peaks which contribute to the triangular shape. One object that demonstrates a similar fashion is TELSTAR 401 which is a GEO satellite whose spin period evolution is shown in Fig. 3.38. In the 18 cases of inactive GLONASS satellites, secular trends also exist.
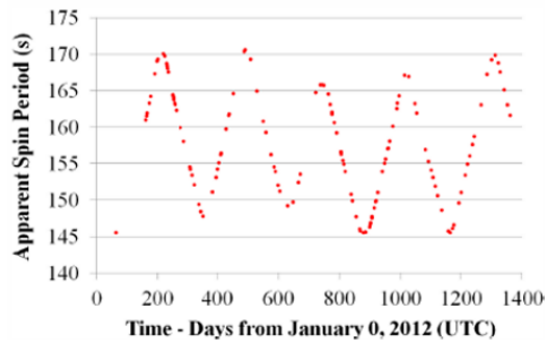
Figure 3.38.: TELSTAR 401's cyclic spin period evolution which is taken from *Earl* (2017).

Typically four peaks (bright reflections) are present in a phase diagram of GLONASS satellites despite different shapes of the diagrams. This evidence which resembles *the four sides* of the satellites was also found previously by *Linder et al.* (2015). Many of the light curves come in 2 pairs of (more or less) similar shape but different size as can be seen in Fig. 3.39. In many occasions, one pair is significantly smaller than the other as can be seen on the right part of the figure. Within one pair, the distance between the peaks is usually around 180°. Most of the light curves have sharp peaks. The exception is for the light curves which belong to COSMOS 1988 (COSPAR ID 1989-001B) and COSMOS 2288 (COSPAR ID 1994-050C). The light curves of these two objects look blunt and do not come in pairs. The sharp profile

of the light curves indicate that they are a result of specular reflection. While a specular reflection can also come from solar panels, they are not likely to be the reason for the light curve morphology we saw where the two peaks within one pair (which are separated around 180°) usually have similar reflection features such as brightness and shape. According to *Earl et al.* (2018) when analyzing the light curve morphology of ECHOSTAR 2 satellite, such characteristic does not likely come from the two sides of a solar panel which are significantly different as they are designed such that one side contains the power generating solar cells while the opposite side is painted with white or black paint. Moreover, as we said before, typically four sharp peaks are present in a phase diagram of a GLONASS satellite which cannot be facilitated by solar panels which only have 2 sides. Those two rationales led us to presume that the morphology of the inactive GLONASS satellites are caused by the four thermal control flaps or radiators (Section 2.5). More detail explanation about the morphology can be found in Appendix D.
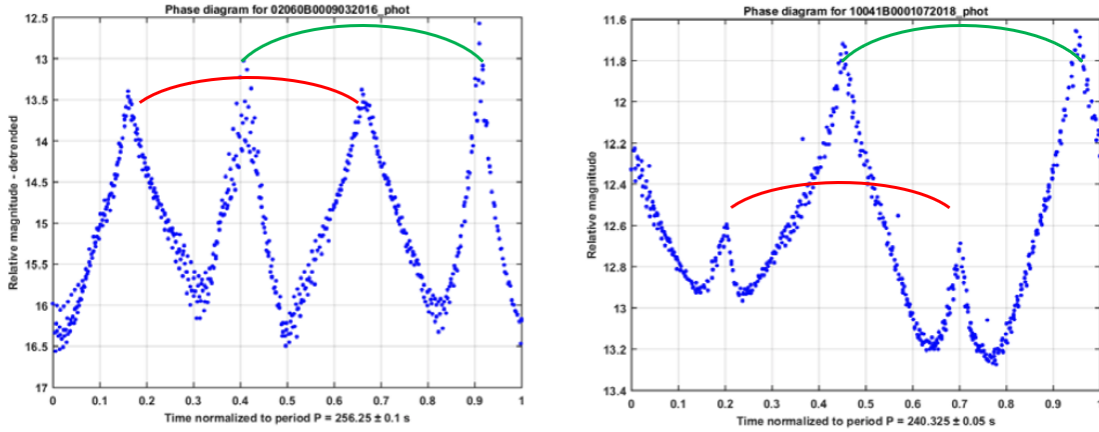
Figure 3.39.: Examples of phase diagrams from two inactive GLONASS satellites. The left belongs to COSMOS 2396 (COSPAR ID 2002-060B) which was observed on 9 March 2016 while the right belongs to 2010-041B which was observed on 1 July 2018. The images are taken from *Rachman et al.* (2018). The two pairs of peaks are identified by two arcs of different color.

Inactive satellites which possess many stable or slow rotator light curves in their history are interesting for further discussion. In the case that the stable or slow rotator light curves are located at the beginning of a spin period evolution then it may indicate an opportunity to witness the beginning of the normal rotator phase of the objects after the decommissioning date. This happened to COSMOS 2465 (COSPAR ID 2010-041B) which was retired on 21 November 2016 (unfortunately, the data points are sparse since we only have 12 observations of this object). Similar things supposedly happened to COSMOS 2431 (COSPAR ID 2007-052C), COSMOS 2442 (COSPAR ID 2008-046A), COSMOS 2447 (COSPAR ID 2008-067A), and COSMOS 2448 (COSPAR ID 2008-067C). In the case of COSMOS 2465, we

found that it reached the rotator state only two months after the retirement which is much faster than the rest of the group. If the slow rotator light curves come in the middle of spin period evolution then it could indicate that the objects cycle between phases of uniform (normal rotation) and tumbling motion (complex rotation) as some GEO satellites do (*Albuja et al.*, 2018). Three objects which clearly demonstrate this feature are COSMOS 2236 (COSPAR ID 1993-010B), COSMOS 2275 (COSPAR ID 1994-021C), and COSMOS 2411 (COSPAR ID 2004-053A). More on this is discussed in Appendix E. Stable light curves can also come after normal light curves. As has been mentioned at the beginning of this section, we found one object with this behavior which is COSMOS 2478 (COSPAR ID 2011-071A). We also found one object which is stable although it has become a debris for at least 7 years which is COSMOS 2449 (COSPAR ID 2008-067B). The object was retired in September 2012.

3.6. Conclusion

The current status of AIUB light curve database is a result of years of planning, observation, and data processing of light curves conducted by the Astronomical Institute of the University of Bern in Switzerland. A large quantity of light curve data and the result of its processing is available now in the database. Therefore, the database can be used to support any studies regarding attitudes of space debris objects circling the Earth. Especially for inactive GLONASS satellites which is the subject of this study, 18 objects with a unique oscillating pattern are available. Each member of the group has spin period rate of change which is always the same (on average) during the repeated increasing or decreasing phase. In terms of angular velocity, this means that, on average, the value of its rate of change (which is the angular acceleration) is always the same during the two phases. The 18 objects are found able to maintain their triangular pattern until at least November 2020 and they will be the main objects discussed in the next chapter.

4. Spin Period Evolution of Inactive GLONASS Satellites

This chapter specifically discusses the 18 inactive GLONASS satellites which demonstrate a triangular pattern in their spin period evolution as introduced in the previous chapter. It starts with the discussion of the observational data in Section 4.1 and derives some characteristics of the group. For the purpose, we created an empirical model of the observational data for each object and defined some parameters. We then calculated some statistics and performed a correlation study between the parameters. After that, in Section 4.2, we created a satellite model to represent the group and performed a simulation using several computer programs. The result was compared to the observational data from a selected member of the group. Finally, Section 4.3 discusses the possibility to perform a prediction of the spin period values using the empirical model which have been created in the first Section.

4.1. Data from observations

Table 4.1 displays basic data of all the 18 inactive GLONASS satellites which are called (for simplicity) *the main objects* from now on. In the table, debris age is defined as the difference between the decommissioned date and the date of the first observation. The decommissioning date is taken from `ftp://ftp.aiub.unibe.ch/BSWUSER52/GEN/SATELLIT.I14` while the first observation date is the first successful observation as recorded in the AIUB light curve database. Most of the main objects are of type IIv or IIc (16 out of 18). Only two of them are of type M. All satellites were launched before 2004 and all the type IIv have become debris for more than 10 years when first observed.

All of the main objects have more than 10 observational data as can be seen on the left side of Fig. 4.1 (in fact, the minimum number of observations is 23). The figure also shows that three objects possess more than 50 observational data. In addition, it also shows that most of the objects were first observed around mid-2015 which is the start of the AIUB inactive GLONASS satellites campaign. Right side of the figure indicates that all objects have been observed between five and six years. In total, 652 light curves of the main objects are available in the database which represent more than 154 hours of observations. The median of the observation time and the median of frame rate are 6.91 min and 0.48 Hz, respectively. As already

Table 4.1.: Selected inactive GLONASS satellites in this study (also called the main objects).

No	COSPAR ID	Type	Launch date	Decommissioned date	First observation date	Debris age [yr]
1	1989-001B	IIv	1989-01-10	1992-02-16	2014-12-22	22.85
2	1990-045A	IIv	1990-05-19	1994-04-23	2015-07-06	21.20
3	1990-110A	IIv	1990-12-08	1994-03-17	2015-07-01	21.29
4	1990-110C	IIv	1990-12-08	1996-06-09	2015-07-11	19.09
5	1991-025A	IIv	1991-04-04	1994-09-29	2015-07-01	20.75
6	1991-025B	IIv	1991-04-04	1992-01-06	2015-07-03	23.49
7	1991-025C	IIv	1991-04-04	1992-02-26	2015-07-03	23.35
8	1992-005C	IIv	1992-01-29	1996-10-25	2015-07-06	18.69
9	1992-047B	IIv	1992-07-30	1997-06-27	2015-07-14	18.05
10	1992-047C	IIv	1992-07-30	1994-06-29	2015-07-06	21.02
11	1994-050C	IIv	1994-08-11	1999-08-24	2015-06-28	15.84
12	1995-009A	IIv	1995-03-07	1999-09-10	2015-06-19	15.77
13	1995-037B	IIv	1995-07-24	2001-01-24	2015-06-17	14.39
14	1998-077A	IIv	1998-12-30	2002-07-08	2015-05-12	12.84
15	1998-077B	IIv	1998-12-30	2003-12-19	2015-07-13	11.56
16	1998-077C	IIv	1998-12-30	2003-10-20	2015-07-16	11.74
17	2002-060C	M	2002-12-25	2008-01-12	2015-06-23	7.44
18	2003-056A	M	2003-12-10	2009-06-18	2015-07-16	6.08

mentioned in Section 3.5, all satellites are usually observed using 1 sec of exposure time with no filter.
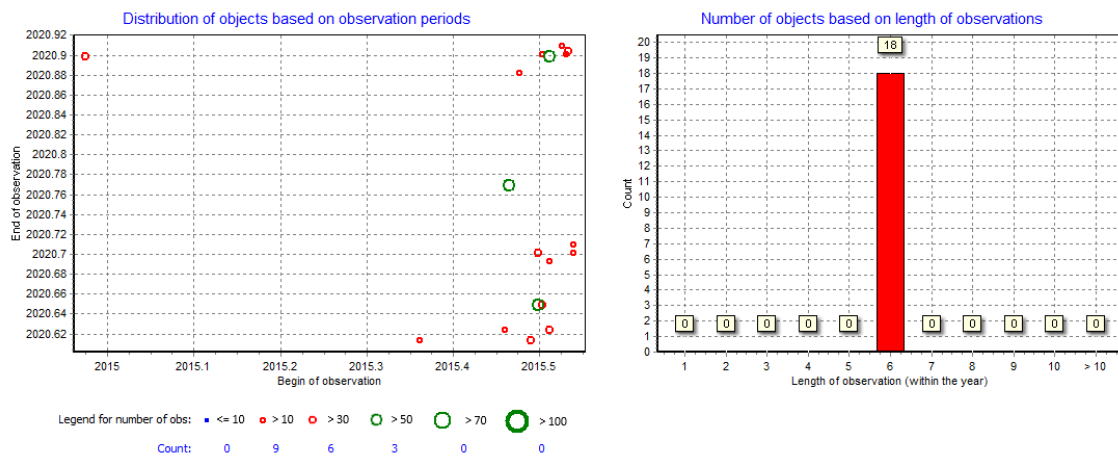
Figure 4.1.: Temporal distribution of observations of the main objects based on observation periods (left) and based on length of observations (right).

In characterizing the oscillating pattern of the main objects' spin period evolution, we use the assumption that the variations in the evolution can be modeled by a series of triangular shapes having similar slopes for the left and right segments (*Rachman et al.*, 2018). Fig. 4.2 illustrates the basic model for the simplest case where all the triangular shapes are similar and the secular evolution trend is linear. For each of the triangular shapes, we identify the peaks (or local extremes) of the oscillation. These are located at the intersection between two adjacent segments. We then calculate the mean spin period by averaging the ordinate of all peaks to get *the average spin period*. We define the amplitude of a cycle as $A = 2c$ where c is the vertical distance between a peak to the local trend line which is created by joining the center of two adjacent segments. Then we calculate the mean amplitude of all cycles to get the *average cycle amplitude*. The periodicity of a cycle P is the time difference between two adjacent top peaks or two adjacent bottom peaks. In the figure, $P = a + b$. We calculate the average of this parameter to get the *average cycle period*. We also calculate the *secular trend change of angular velocity* (ω) *per year* and the *average segment change of angular velocity per month*. To create the whole series of the triangular shapes, we first begin by creating a *principal triangular shape*. It is created using two adjacent segments which possess the largest number of data points. This principal shape serves as a base for creating the rest of the series.
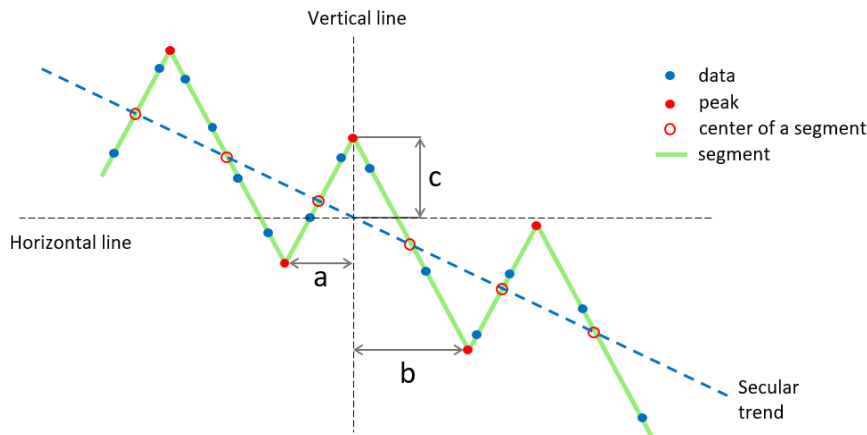
Figure 4.2.: Basic model of spin period evolution for the main objects in this study. a, b, and c are parameters within the triangular shape which are used in characterizing the model of a specific object.

Figure 4.3 shows a comparison between observational data of one of the main objects and the empirical model based on the given data. For this case, we select segment 4 and segment 5 to create the *principal triangular shape*. As can be seen on the left side of the figure, the two segments are the only segments with sufficient data points to create the base. Despite this shortage, the right side of the figure shows how the

resulting model nicely fits the whole data. The figure also shows that the average dynamics trend is more or less linear. Appendix A displays all the comparisons of spin period evolution based on observational data and its empirical model for the main objects.
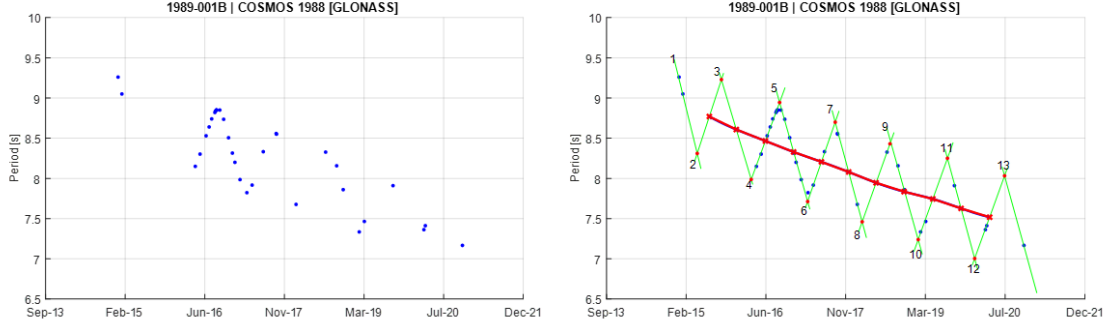
Figure 4.3.: Comparison of a spin period evolution based on observational data (left) and its empirical model (right) of a sample object. The red line runs through each center of all applicable segments to represent the average dynamics of the evolution. Each segment is labeled with a number. Red dots represent peaks.

Table 4.2 shows the result of characterizing all the main objects. The statistics of all the parameters listed in the table are presented in Table 4.3. The table shows that the average spin period of the main objects varies greatly from 8.11 sec to 469.58 sec. This is similar to the average cycle amplitude which varies from 1.10 sec to 513.24 sec. On the contrary, the average cycle period only varies slightly from 0.78 years (285.10 days) to 1.35 years (494.22 days) and its mean and median values are close to 1 year (365.25 days). The last column which is the average segment change of ω per month is basically the value of angular acceleration (which was found to be relatively constant for each of the main objects). This value also varies greatly from 0.021°/s to 2.680°/s.

Fig. 4.4 shows the long term variation of the average spin period evolution of the main objects. We can see that most of the objects have diminishing trend. To be more specific, all of the variations which are less than 100 sec have a diminishing trend. This is in contrast with the ones with values more than 100 sec which seems are not constrained to any specific trend. Overall, this means that the main objects tend to get faster during their lifetime.

After trying to find a relation between all the parameters given in Table 4.2, we found only two cases which apparently show some correlations. The two relationships are the average cycle amplitude versus average spin period (Fig. 4.5) and the secular trend change of ω per year versus average spin period (Fig. 4.6) with coefficient of correlation equals to 0.84 and −0.45, respectively. Other relationships between parameters are given in Appendix B. However, by using angular velocity instead of spin period, we found a stronger correlation with the secular trend change of ω per

Table 4.2.: The result of characterizing the spin period evolution of the main objects. ω is angular velocity.

No	COSPAR ID	Average spin period [s]	Average velocity [°/s]	Average cycle amplitude [s]	Average cycle period [yr]	Secular trend change of ω per year [°/s]	Average segment change of ω per month [°/s]
1	1989-001B	8.11	44.68	1.10	0.95	1.408	1.040
2	1990-045A	37.00	9.77	2.71	1.13	0.340	0.111
3	1990-110A	50.17	7.19	4.26	1.11	0.120	0.089
4	1990-110C	136.81	3.59	108.43	1.25	0.359	0.394
5	1991-025A	40.71	8.89	6.05	1.02	0.095	0.212
6	1991-025B	46.62	7.83	8.56	1.35	0.300	0.179
7	1991-025C	193.41	1.86	18.06	1.09	0.001	0.028
8	1992-005C	127.80	2.84	12.95	0.90	−0.143	0.056
9	1992-047B	232.31	1.58	49.73	0.97	−0.093	0.060
10	1992-047C	58.82	6.13	2.84	0.78	0.059	0.068
11	1994-050C	11.94	32.05	5.52	0.96	0.634	2.680
12	1995-009A	79.92	4.56	16.74	0.87	0.083	0.182
13	1995-037B	469.58	1.17	513.24	0.98	0.028	0.243
14	1998-077A	66.55	5.42	2.10	0.95	0.109	0.033
15	1998-077B	58.76	6.14	1.51	0.94	0.165	0.034
16	1998-077C	72.38	5.02	8.76	0.98	0.181	0.109
17	2002-060C	127.90	3.05	52.56	0.79	0.140	0.304
18	2003-056A	235.17	1.53	18.32	0.96	−0.046	0.021
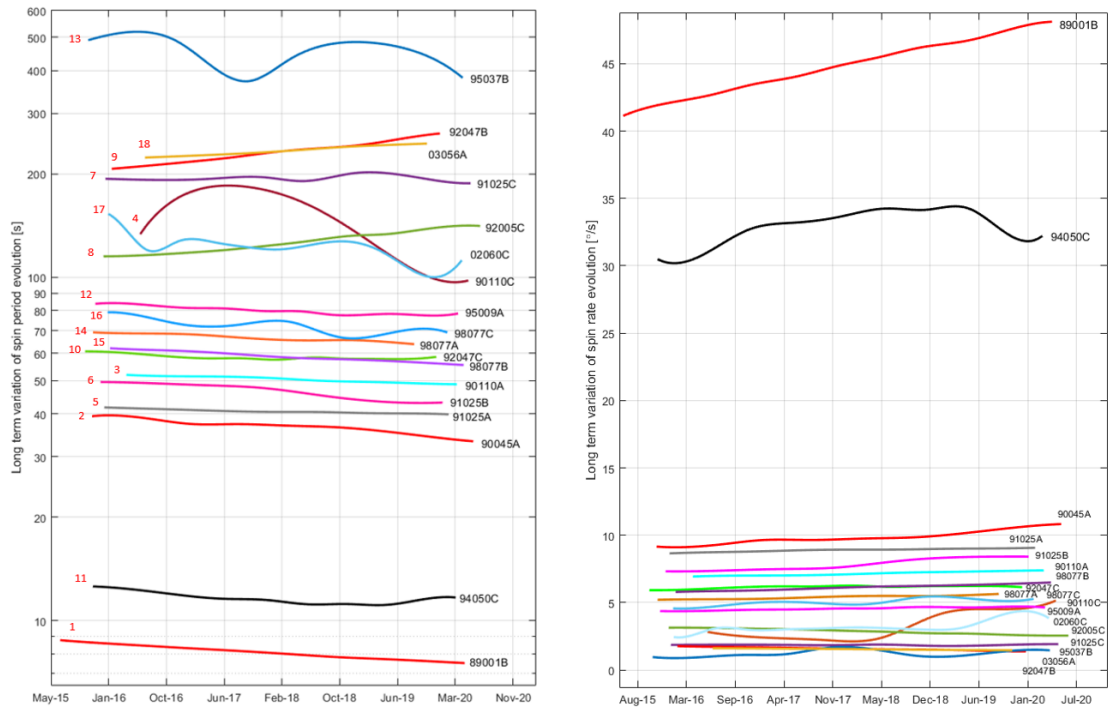
Figure 4.4.: Long term variation of the average spin period evolution of the main objects (left) and that for their spin rate (right). Here, cubic splines are used to represent average dynamics of the evolution. Each line is labeled with the corresponding COSPAR ID on the right. On the left graph, the object's number in Table 4.1 is also available.

Table 4.3.: Statistics of the result of characterizing the spin period evolution of the main objects. ω is angular velocity.

Statistics	Average spin period [s]	Average velocity [°/s]	Average cycle amplitude [s]	Average cycle period [yr]	Absolute value of secular trend change of ω per year [°/s]	Average segment change of ω per month [°/s]
Maximum	469.58	44.68	513.24	1.35	1.408	2.680
Minimum	8.11	1.17	1.10	0.78	0.001	0.021
Mean	132.82	8.13	70.88	1.01	0.227	0.395
Median	69.47	5.22	8.66	0.96	0.130	0.110

year in which the coefficient of correlation equals to 0.93. Moreover, we also found a strong correlation with the average segment change of ω per month in which the coefficient of correlation equals to 0.75. This means that main objects with higher spin rate tend to have higher *secular trend change of rate per year* and also higher *average segment change of rate per month*. Since *change of rate* means *acceleration* then, in other words, we found that objects with higher spin rate tend to accelerate more. We currently do not have any explanation on this.
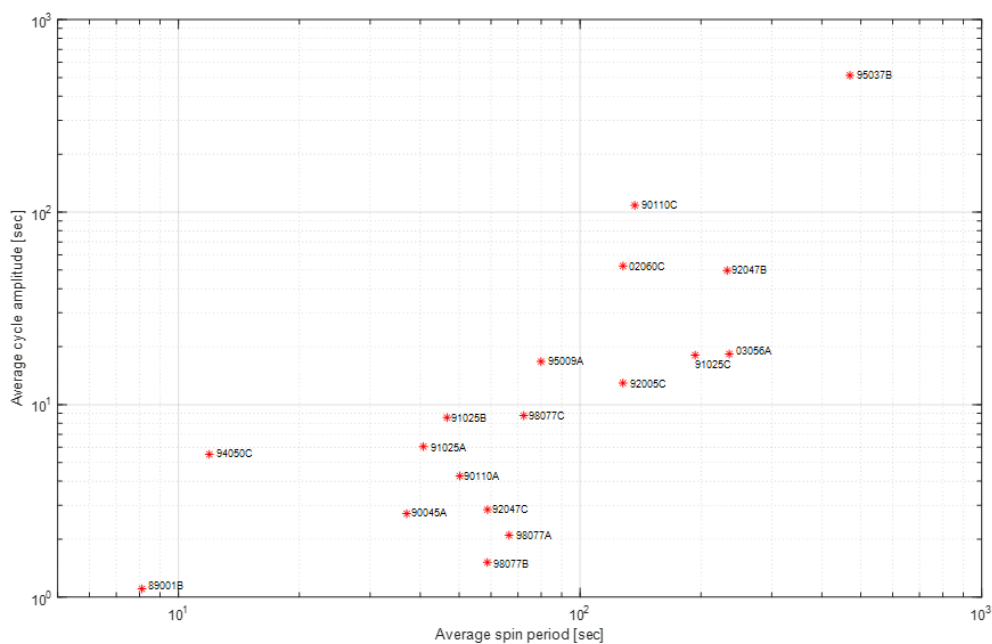
Figure 4.5.: Relationship between average cycle amplitude and average spin period of the main objects. Each star is labeled with its object's COSPAR ID.
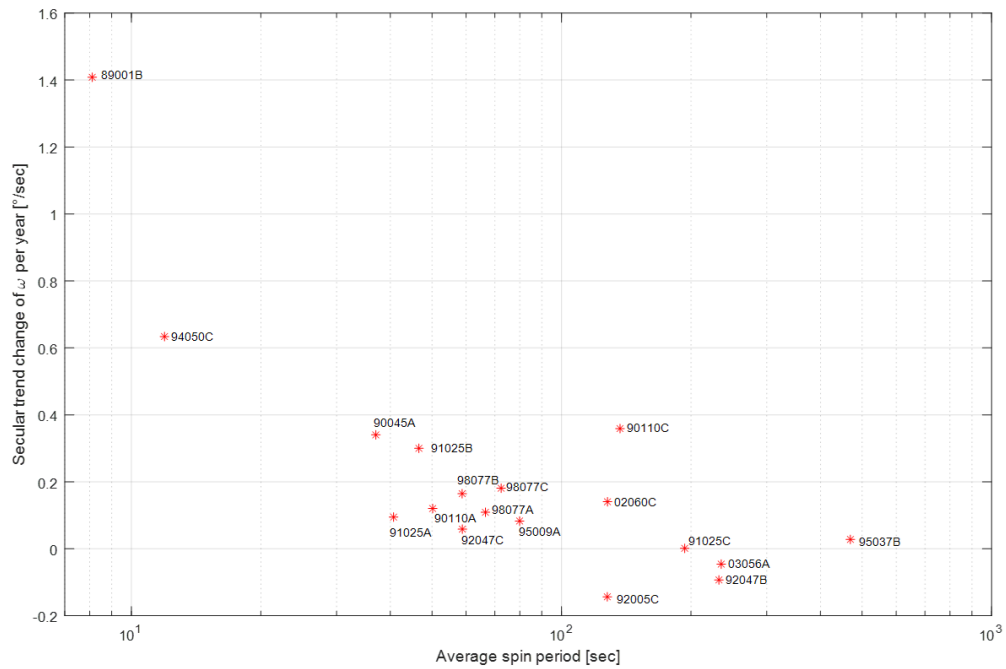
Figure 4.6.: Relationship between secular trend change of angular velocity ω per year and average spin period of the main objects. Each star is labeled with its object's COSPAR ID.

4.2. Modeling and simulation

This section describes how the aforementioned rotation pattern of some of the inactive GLONASS satellites could be explained. This is done by creating a satellite model to represent the group and simulating the rotation rate of the model under different conditions. Most of the part is taken from *Rachman et al.* (2020).

The idea of the simulation is to be able to roughly replicate the pattern of spin rate evolution from one of the main objects. Since most of the main objects are of type IIv of GLONASS satellites, we built our model based on the type. An iterative process was performed until we obtained a similar pattern.[1] We picked (rather arbitrarily) one satellite from the main objects as the reference. The satellite is COSMOS 2140 (COSPAR ID 1991-025B) which was launched on April 4, 1991 and retired on January 6, 1992 (23 yrs of debris age). Apparent spin periods from the database are available from July 3, 2015. The data was obtained with the ZIMLAT telescope and a CCD camera with no color filter at AIUB's Observatory in Zimmerwald as discussed in Section 3.5.

For the modeling and simulation, several assumptions are necessary to be taken.

---

[1]More accurate replication is beyond the scope of this study.

First of all, we assumed that the object is a rigid body (Section 2.2) so that the distance between any two given points on it remains constant in time. We also assumed that there is no effects from attitude control system activation, tank sloshing, and specific impact or leakage events. Since simulations covering a period of several years are necessary as this is a study of evolution, first simulations only considered solar radiation pressure (SRP) torque as the environmental torque to speed up the computation. This approach is reasonable since typically solar-pressure torques (Section 2.3) are significant for a satellite with relatively large solar panels at medium orbit.

Considering the similarity between type IIv GLONASS satellites with GORIZONT satellites, we adopted a simple model of GORIZONT satellite as our model (Fig. 4.7). The model was used before in *Albuja et al.* (2015).[2] As we can see in the figure, the model has a cylinder shape for the bus and two rectangular plates as wings for the solar panels. We can also see that the model is ideally symmetric and should experience no torque if its center of mass were at its center of figure.
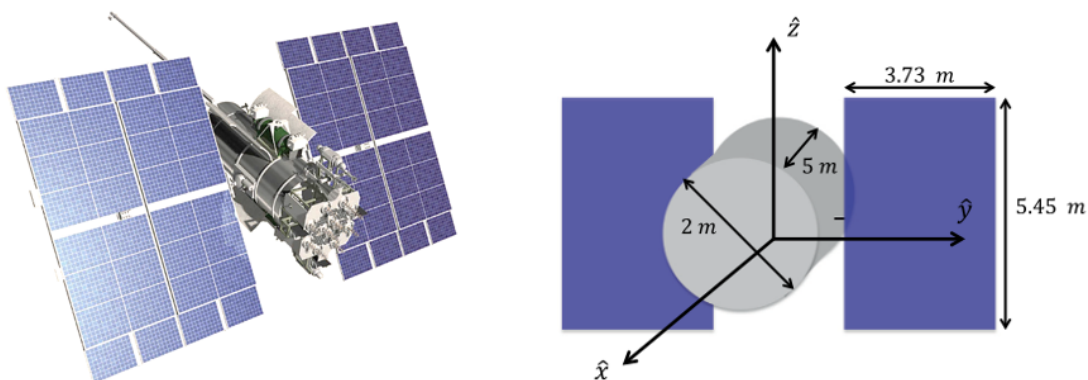
Figure 4.7.: Illustration of a GLONASS IIv satellite (*Revnivykh et al.*, 2017) (left) and GORIZONT satellite model (*Albuja et al.*, 2015) adopted in this study for GLONASS satellite model (right).

Table 4.4 shows the basic physical properties of the model. Next, we created a 3D model using Blender, which is a free and open-source 3D computer graphics toolset. The bus is assumed as a solid cylinder and the solar panels are assumed as thin plates. We also assumed that the axis of solar panels run exactly through the center of the bus across the long axis as seen in Fig. 4.8. The 3D model shown in the figure is the basic model which means that both the solar panels are aligned to each other and they are orthogonal to the long axis of the body. The output of Blender is the surface geometry file (in `obj` format for this study) which was used in the subsequent processes.

---

[2]Using similar satellite model for simulations allows us to compare our results with that from *Albuja et al.* (2015) to some extent.

Table 4.4.: Basic physical properties of the satellite model used in this study.

Property	Value
Mass	2110 kg
Bus length	5 m
Bus diameter	2 m
Solar panel length (one side)	5.45 m
Solar panel width (one side)	3.73 m
Solar panel depth	5 cm
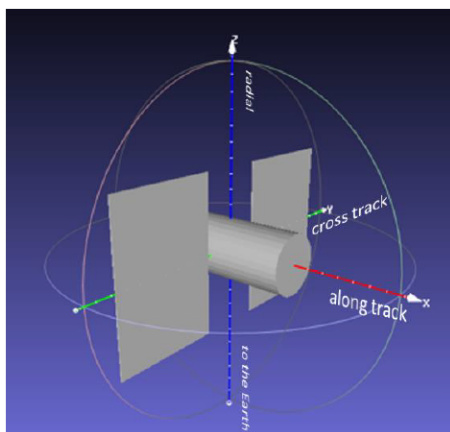
Figure 4.8.: Basic 3D model of GLONASS satellite used in this study and its default orientation with respect to the orbital frame.

Simulations of the rotation rate under different conditions were performed using iOTA (in Orbit Tumbling Analysis) (*Kanzler et al.*, 2014). It is a software to perform short- (days), medium- (months) and long-term (years) propagation of the orbit and attitude motion (six degrees-of-freedom) of spacecraft in Earth orbit.[3] For our purpose, iOTA reads the resulting surface geometry file (as mentioned in the previous paragraph) together with other input parameters like mass, center of mass, moments of inertia, radiation absorption factor (the difference to 1 is reflection), and diffuse reflection factor (the difference to 1 is specular reflection) of the satellite model. In this study, the center of mass and moments of inertia were calculated using another free and open-source software called MeshLab.[4] We used the default value of absorption factor and diffuse reflection factor given by iOTA which are 0.7

---

[3]Beside the ability to perform orbit and attitude propagation of a spacecraft, iOTA's post-processing modules will generate synthetic measurements, e.g. light curves, Satellite Laser Ranging (SLR) residuals and Inverse Synthetic Aperture Radar (ISAR) images that can be compared with the real ones.

[4]MeshLab uses unity density in the calculation of inertia tensor. Consequently, after using the tool to find the inertia tensor, we used the formula below to get the moment of inertia of the

and 0.6, respectively in the first iterations. This means 30% of the incident radiation is reflected and 40% of this reflection is reflected specularly.

We chose three parameters to define the initial conditions for the simulations:

1. The orientation of the solar panels with respect to the body frame;

2. The initial orientation of the satellite with respect to the orbital frame;

3. The initial angular velocity vector of the rotation.

Regarding the first parameter, canting angles (which are the angle between the two solar panels) are important for providing an asymmetry to the satellite model. We learned this from the case of ECHOSTAR 2 and GORIZONT that we have discussed in Section 2.4. According to *Earl* (2017), if the satellite solar panels had identical dimensions, identical reflectivity (both panel sides 1 and 2) and canting angle of zero then the instantaneous net SRP torque on the satellite would always be zero and therefore the angular velocity would not vary over time. In the case of GORIZONT satellite, since the presence of asymmetry is also necessary, *Albuja et al.* (2015) assumed that the center of mass of the satellite is located at the center of the bus offset by 10 cm along the y-axis to simulate some asymmetry that may be present in the bus of the satellite. The authors also provided an asymmetry by assuming density homogeneity (i.e. no center of mass off-set) and rotating one of the solar panels. In this case, the solar panels needed to be rotated between 9° and 22° in order to match the inferred coefficients of YORP.

Simulation time was varying from 3 minutes to 3 years. The shorter simulation time was set up to see the rotational dynamics in more detail. After getting the results from the first iterations (which only use SRP torque) we did the second iterations using also other relevant environmental forces available which are third body forces, eddy current damping, and gravitational torque.

In iOTA, the initial attitude state is specified using roll, pitch and yaw angles and the corresponding roll, pitch and yaw rates, either relative to the inertial frame or relative to the orbital frame. The latter is shown in Fig. 4.9. The rotations are performed in the following order with respect to the (non-rotated) reference axes: yaw – pitch – roll.

---

satellite model

$$I = \frac{\text{inertia tensor from MeshLab}}{\text{mesh volume from MeshLab}} \times \text{object's mass}$$
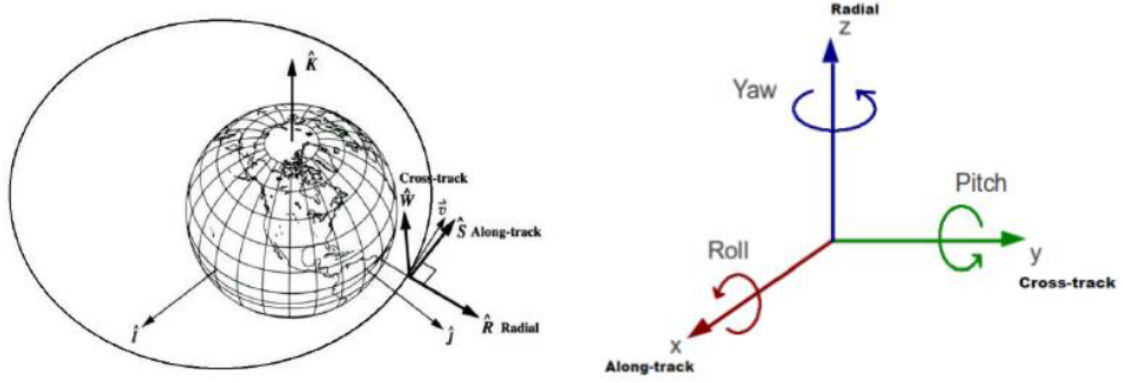
Figure 4.9.: Configuring initial state in iOTA (*Karrang and Kanzler*, 2017)

Two-line element orbital data for the simulation which is needed by iOTA was obtained from the Space-Track website (`www.space-track.org`). State vectors were extracted from this data to obtain the positions and velocities of the satellite at the beginning of the simulations which is defined as 1 September 2015 at 21:00:00 UTC. COSMOS 2140 is moving in a circular medium Earth orbit with a radius around 19180 km from Earth's center and an inclination of 65.48°.

After doing a lot of simulations using different conditions, we found that the orientation of solar panels with respect to the body frame and the initial orientation of the satellite with respect to the orbital frame as shown in Fig. 4.10 successfully produced an oscillating or sinusoidal pattern with a period around one year.[5] To be specific, the solar panels are orthogonal to each other and both of them are slanted with respect to the body (bus). Also we used initial angles of [0, 90, 0] in terms of Euler angles which means that the model was rotated only around its pitch axis (y-axis in Fig. 4.10) by 90° and initial angular velocity of [0, 0, 6] in terms of rotation vector which means that the angular velocity was only applied around the yaw axis (z-axis in Fig. 4.10) by 6°/s. As a comparison to the default orientation before adding any rotation to the model, see Fig. 4.8. The moment of inertia tensor for the satellite model used in the simulation which is Sim 83 (means simulation number 83) is

$$I_{\text{sim83}} = \begin{bmatrix} 3755.17 & -1.11 & 10.95 \\ -1.11 & 4954.97 & 11.55 \\ 10.95 & 11.55 & 7067.93 \end{bmatrix} \text{kg} \cdot \text{m}^2$$

which tells us the yaw axis (z-axis in the figure) is the object's major principal axis.

---

[5]Simulations with iOTA usually take a lot of computing time. We found that using 10^{-5} as the maximum error in the computation is our optimal setting.
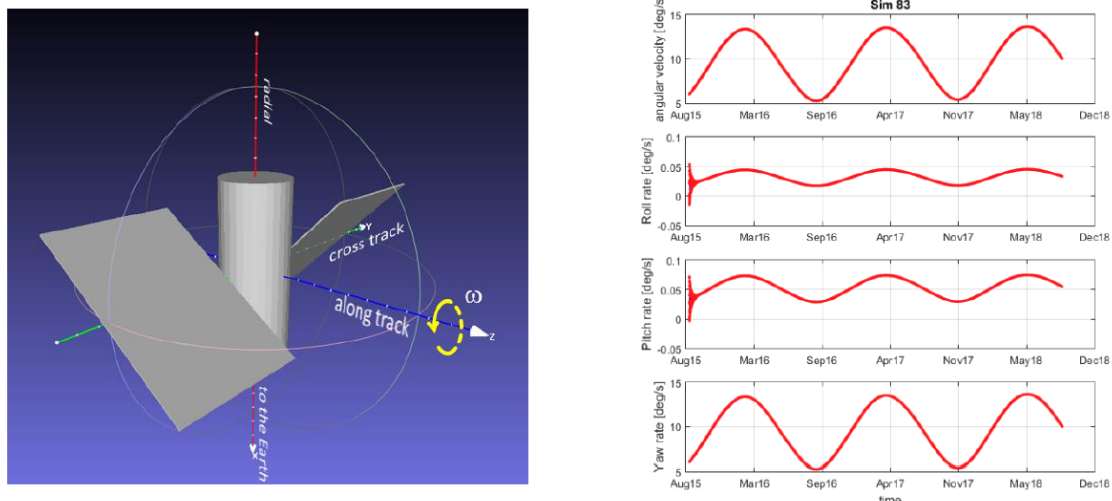
Figure 4.10.: The condition of solar panel with respect to the body frame and the initial orientation of the satellite with respect to the orbital frame which successfully produced an oscillating pattern with a period around one year (left image) and the result of the simulation (right image). On the left image, ω is the angular velocity.

By varying the canting angles, we found that this parameter determined the amplitude of the oscillating pattern (Fig. 4.11). From this finding, we concluded that a (roughly) annual oscillating pattern is achievable only if the two solar panels oriented differently.

The moment of inertia tensors for the satellite models used in the Fig. 4.11 are

$$
I_{\text{sim87}} = \begin{bmatrix} 3999.64 & 0 & 0 \\ 0 & 4955.03 & 0 \\ 0 & 0 & 6823.50 \end{bmatrix} \text{kg} \cdot \text{m}^2
$$

$$
I_{\text{sim88}} = \begin{bmatrix} 3995.07 & -0.00 & -0.00 \\ -0.00 & 4954.89 & 1.59 \\ -0.00 & 1.59 & 6827.94 \end{bmatrix} \text{kg} \cdot \text{m}^2
$$

$$
I_{\text{sim89}} = \begin{bmatrix} 3981.49 & -0.00 & -0.00 \\ -0.00 & 4954.89 & 3.17 \\ -0.00 & 3.17 & 6841.50 \end{bmatrix} \text{kg} \cdot \text{m}^2
$$

Our finding that a (roughly) annual oscillating pattern is achievable only if the two
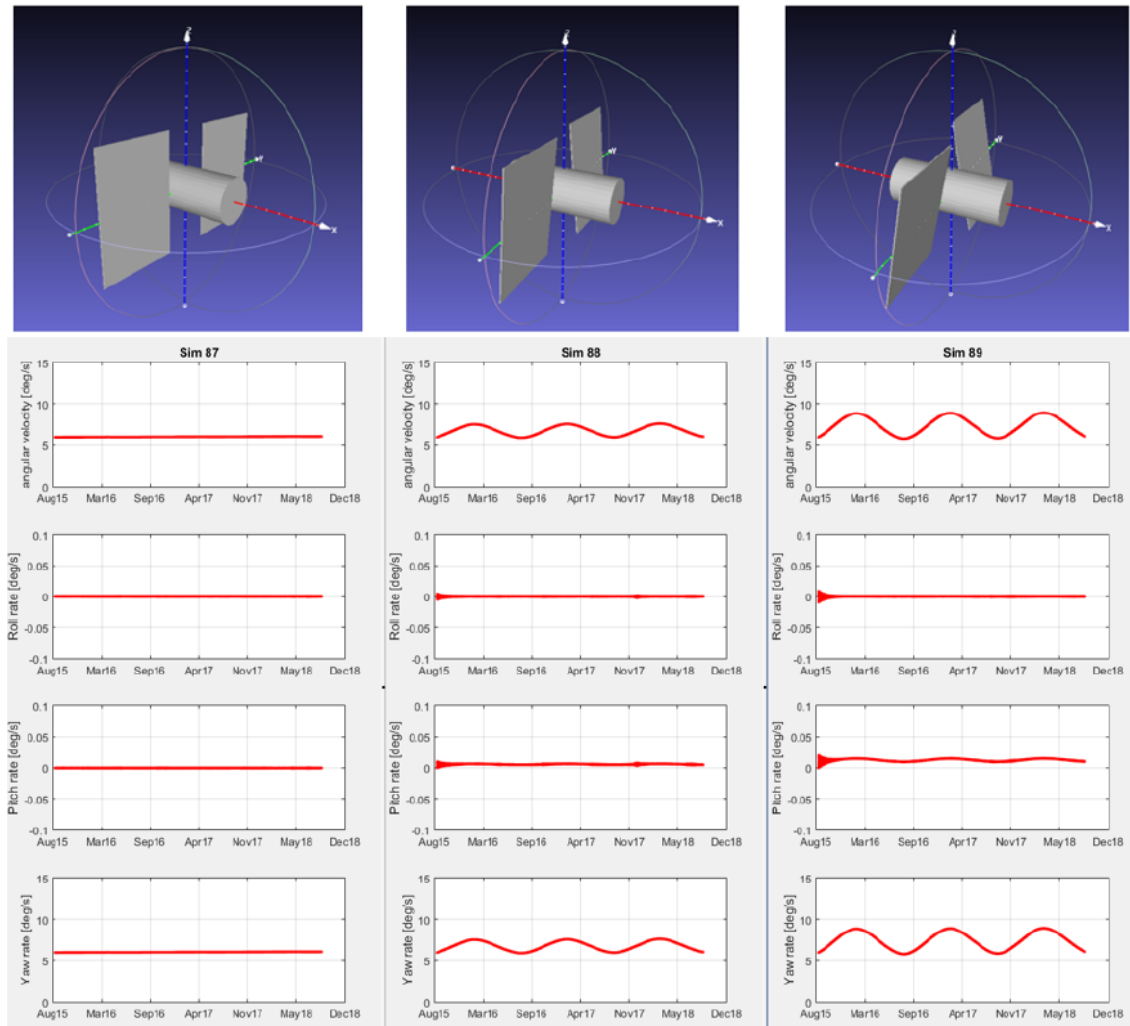
Figure 4.11.: The relation between canting angles and the amplitude of the oscillating spin rate evolution pattern: canting angle of 0° (left image), 10° (center image), and 20° (right image). All simulations were performed with only SRP, initial angle of [0, 90, 0] and initial angular velocity of [0, 0, 6].

solar panels oriented differently seems independent of the initial orientation of the satellites and of the rotation axis (which are the other two parameters that define the initial condition of the simulations). Fig. 4.12 gives the result from three simulations to demonstrate the notion. The figure also shows the geometry of the satellite model used in the simulations. We can see from the figure that Sim 79 uses a model where one of its solar panel is orthogonal to the bus while the other is slanted. Sim 84 and Sim 86 use a model similar to Sim 83 where both the solar panels are slanted with respect to the bus. The initial orientation of the satellites and the rotation axes are described in the legend of the figure. We can see from the result that although all the simulation succeed in producing an oscillating pattern, none of them looks similar to the repeating triangular shape we are looking for (which can be roughly produced by Sim 83).

Figure 4.12.: Oscillating patterns of three simulations with different orientation of solar panels, initial orientation of the satellites, and rotation axes. Each of the models has solar panels oriented differently. Sim 79 uses the model on the top right while Sim 84 and Sim 86 use the model on the bottom right.
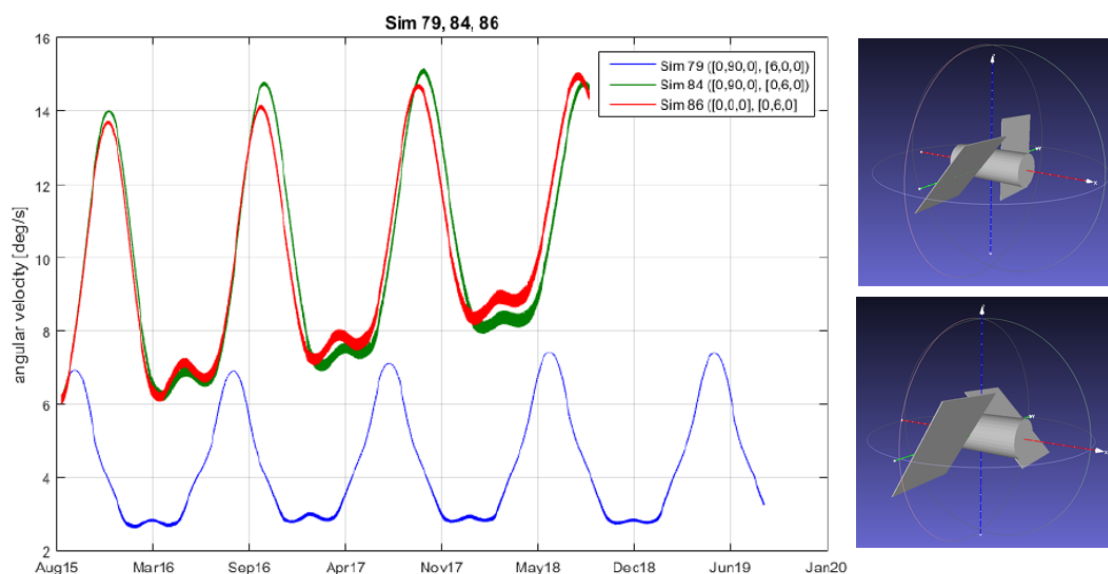
The moment of inertia tensors for the satellite models used in the Fig. 4.12 are

$$
I_{\text{sim79}} = \begin{bmatrix} 3875.33 & 2.13 & -148.18 \\ 2.13 & 4954.92 & 5.86 \\ -148.18 & 5.86 & 6947.68 \end{bmatrix} \text{kg} \cdot \text{m}^2
$$

$$
I_{\text{sim84}} = I_{\text{sim86}} = I_{\text{sim83}}
$$

103

After applying other environmental factors, we found that the only environmental force acting on the satellite that may be responsible for the oscillating pattern is the SRP as shown in Fig. 4.13 as expected. We can see from the figure how the SRP torque is amplified as the canting angle increases which is consistent with Fig. 4.11. *Lips et al.* (2017) also found the same behavior when analyzing the zigzag pattern in ENVISAT long-term angular velocity simulation. They concluded that the periodic behavior is caused by solar radiation pressure on the solar array of the satellite. The authors argued that a plausible explanation is that when the solar array is illuminated in spin direction, the SRP torque increases the spin rate, adding angular momentum. Periodically, the orientation of the solar array with respect to the incoming radiation is flipping. This makes the angular acceleration from SRP to be directed in counter-spin direction for the following period; hence decreasing the rotation.
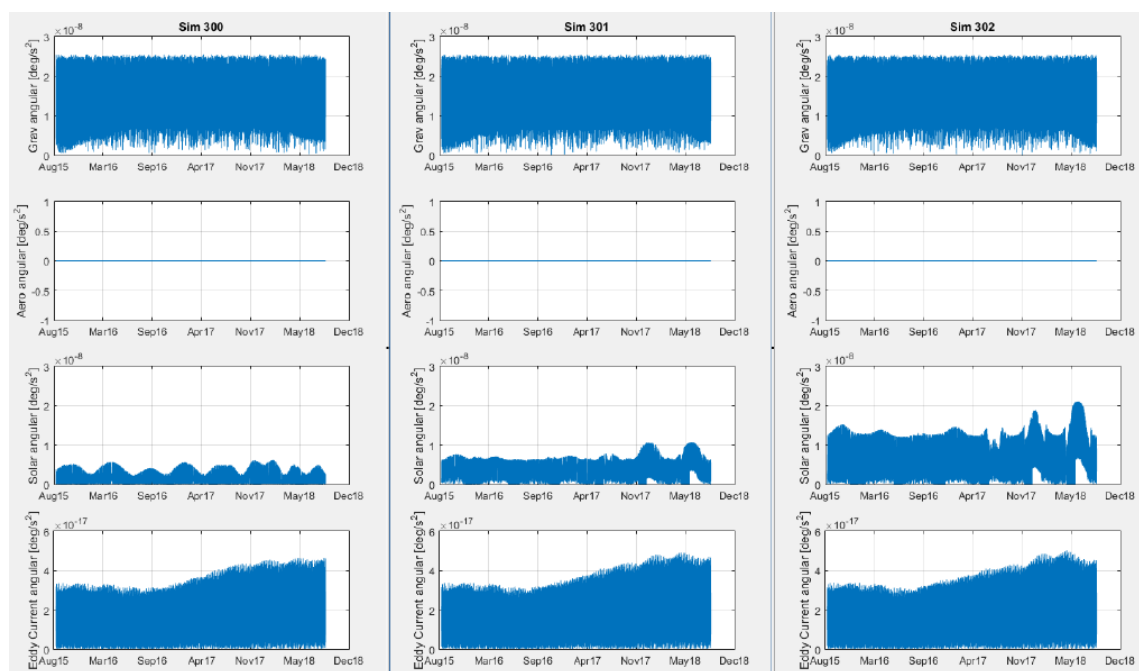
Figure 4.13.: COSMOS 2140 long-term environmental torques perturbations from three simulations: with canting angle of 0° (left image), 10° (center image), and 20° (right image). The effect of atmospheric drag is ignored in this simulation.

The canted solar panels in the case of box-wing satellites (e.g. of COSMOS 2140) are subject to a mechanism similar to a wind wheel or fan. Fig. 4.14 shows how the incoming sunlight (solar radiation) exerts a pressure whose direction is negative with respect to the surface's $\hat{n}$ unit vector direction. The pressure produces a torque $\boldsymbol{N}$ on each of the solar panel which altogether contributes to the rotation by increasing the spin rate. Later, when the orientation of the solar panels with respect to the incoming radiation is flipping (after roughly half a year) as the Earth is revolving around the Sun, it makes the angular acceleration to be directed in counter-spin

direction for the following roughly half a year period decreasing the rotation. The figure illustrates the case where the incoming radiation is parallel to the axis of rotation. The motion is more complicated if the incoming radiation is not parallel to the axis of the rotation which could create a precession. However, it can be assumed that in the general case, both components of the incoming radiation are always present and that this will result in two different torques.
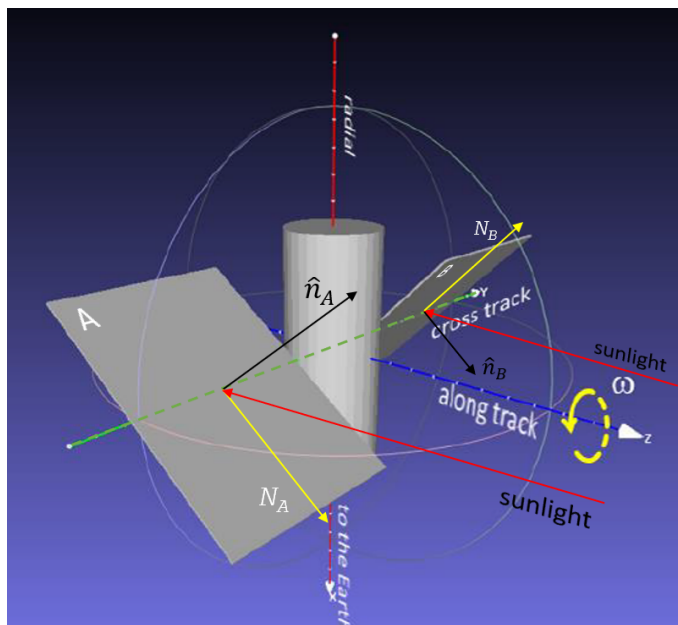
Figure 4.14.: Illustration of how the incoming sunlight produces torques that contribute to the rotation.

Modeling the effect of different optical properties of the satellite components which is an important part was not yet facilitated by iOTA. Therefore, another software called D-SPOSE was employed. The software was developed for space debris remediation purposes for the analysis and prediction of the rotational motion of large space debris in order to determine, to the highest degree of accuracy possible, the evolution of the rotational parameters of uncontrolled space objects over a time scale of years (*Sagnières*, 2020). Using the software, we tried to simulate the decreasing slope of one of the main objects which is COSMOS 2139 (COSPAR ID 1991-025A) with 20 years of debris age (Table 4.1).

According to the mechanism identified above, for the purpose of the fitting, the following parameters can be changed within D-SPOSE: 1) the initial velocity which will shift the whole plot up or down; 2) the direction of the z-axis in the ecliptic plane which will shift the whole plot left or right (phase of the sinusoid); 3) the specular reflection coefficients of front side and back side of the panels where the average of the two coefficients determines the amplitude in the plot while their ratio determines the secular slope; and 4) the canting angle which also determines the amplitude in the plot (alternative to the change of reflection coefficients). Using the

software, we were able to simulate the decreasing slope of one of the main objects which is COSMOS 2139 as shown in Fig. 4.15. A good fit was found using initial velocity of 8.5°/s; direction of z-axis in ecliptic plane = 119.3° ecliptic longitude; reflection coefficients: front = 0.5, back = 0.4; and canting angle = 5°. Compared to the observational data, we considered the overall accuracy is sufficient except for points near the peaks where the model cannot replicate the sharp pattern. Further studies and simulations are necessary to solve this issue.
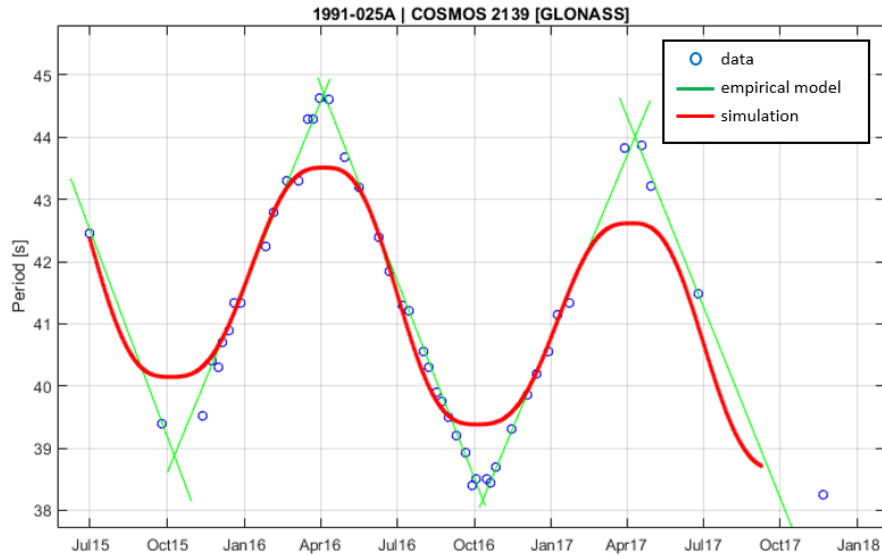
Figure 4.15.: Comparison between observational data and simulation for COS-MOS 2139.

4.3. Prediction

Given the regularity of the pattern we found on the main objects, we can use the empirical models to estimate the spin period on any date (covered by the historical data) by using interpolation. These values can be used as inputs to obtain the final spin periods using the methods described in Section 3.3. The interpolation can be applied for any member of the main objects for any date before the next estimated peak. As an example, let us estimate the spin period of last observation of COSMOS 2139 (1991-025A) on 24 August 2020 (which is the last observation for the object in this study) and compare the result with the one from the database. For this purpose, a short script was created which takes the specified date and the coordinates of all the peaks as inputs. The peaks are used to create the segments and subsequently their equation to get the period. Using the equation we got the spin period of the satellite on 24 August 2020 equals to 38.867 sec. This value is reasonably close to the one from the database which is 38.825 sec. Fig. 4.16 shows the observational

data and its model used in the example.
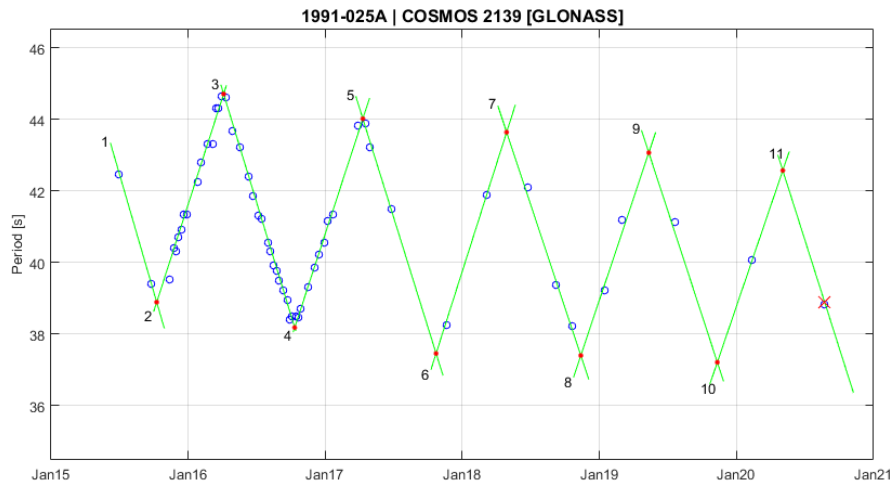
Figure 4.16.: The observational data (blue circle) and its model (green segments) for the spin period evolution of COSMOS 2139. Each segment is marked with a number. A red cross on the last segment (segment number 11) indicates the period obtained using the model which matches the data.

Listed below is the MATLAB script we used for the example.

```
function [mdate,per] = find_period(date,peaks)
mdate = jd2md(julianDay(date));
p = peaks(:,1) < mdate;
s = size(find(p == 1));
linenum = s(1) + 1;
lineObj = findobj(gca,'type','line','color','g');
x = lineObj(length(lineObj) + 1 - linenum).XData;
y = lineObj(length(lineObj) + 1 - linenum).YData;
m = (y(2) - y(1))/(x(2) - x(1)); % slope
per = y(2) + m*(mdate - x(2));
hold on, plot(mdate,per,'^r')
```

COSMOS 2139 is among six objects which have a nearly linear trend. The others are COSMOS 1988 (1989-001B), COSMOS 2109 (1990-110A), COSMOS 2204 (1992-047B), COSMOS 2363 (1998-077B), and COSMOS 2404 (2003-056A). For these objects, the spin period estimation can be performed even further in the future (or in the past) if we can assume that the pattern is preserved. The assumption will allow us to estimate the location of the next peaks (which, again, are necessary to create the segments). The model of each of the six objects can be seen in Appendix A.

It is interesting to see how other objects deviate from the linear trend. Significantly shorter or longer segments than the average in the evolution may be an indication of particular events such as collision with debris, etc. Unfortunately, we found that

in some cases, the data points were simply not sufficient to confirm the location of the adjacent peaks which define the length of the related segments.

4.4. Conclusion and interpretation

The likely natural cause responsible for the roughly annual oscillating pattern in the spin period evolution of the main objects is solar radiation pressure. For those objects, the feature can only be possible if the solar panels are canted which allows a mechanism similar to a wind wheel or fan to work on the system. Depending on the relative orientation of the incoming radiation to the axis of rotation which switches over every approximately half a year, SRP produces a torque on each of the solar panel resulting on an increase or decrease of the spin rate. Another feature, the secular trend of the spin period evolution, is a result of different values of the specular reflection coefficients of front side and back side of the panels. Since each side of a solar panel is expected to have a different reflectivity (and smoothness) due to their basic design (as mentioned in Section 3.5), we found all main objects usually possess a secular trend. As for the reason why the canting angle exists, it could be related to the design of the solar panel system. It is possible that the satellite manufacturer may intentionally put a tolerance for the system which allows for the cant. How much the canting angle is, remains a question. While we found a value of 5° in this study, *Earl* (2017) found for the case of ECHOSTAR 2 that the canting angle is only 0.01° which he said very low when compared with previously reported values.

As also mentioned in Section 3.5, we found an indication that all inactive GLONASS satellites possess both features (an oscillating pattern and a secular trend) after inspecting the whole group in the database especially having at least 40 observations. This suggests that those features are part of common characteristics of inactive GLONASS satellites of type IIv and M. However, the cycle between normal rotation and tumbling or complex rotation as we found in three cases and discussed in Appendix E, can terribly disrupt the oscillating pattern. Less dramatic changes to the pattern can happen if a segment's length is significantly different (either shorter or longer) than the previous similar (either left or right) segment. This changes will deviate the evolution pattern from the "ideal" linear trend. The fact that there are six objects which closely demonstrate a linear trend and with average cycle periods very close to one year (overall mean value equals to 0.9917 year) suggests that a long term (more than 5 years) consistency of a cyclic spin period evolution pattern of RSOs is possible.

Knowing that some RSOs can remain in a consistent attitude behavior for such a long time can be useful in mitigating space debris problems. As discussed in Section 4.3, spin period estimations can be performed for those objects further in the future if we can assume that the pattern is preserved. This study has found six of those objects. If we use the value of 30°/s as the maximum spin rate which allows for

a successful capture in ADR missions (as mentioned in Section 2.1) then all those six objects are possible as candidates except for COSMOS 1988. In fact, 16 out of 18 main objects are possible as candidates for ADR missions in terms of spin rates (Fig. 4.4). This result can give us more insights into the spacecraft design which allows satellites to have a long consistent attitude behavior after decommissioning. Another benefit that can be obtained from this study which analyzes more than 1800 light curves from 70 defunct satellites with more or less similar design and represent more than 540 hours of observations, is that we can learn more about how the space environment interacts with spacecraft's components over a long duration.

5. Summary and Outlook

5.1. Summary

Humanity's dependence on space technology is extensive and varied. Yet, the proliferation of space debris is a major concern due to its potential for catastrophic damage to space activity. To mitigate this risk, extensive efforts must be undertaken to minimize potential hazards, including the characterization of interesting objects in terms of their attitude behavior. This will benefit future ADR missions which are considered necessary to stabilize space debris population. Moreover, knowledge of the rotational dynamics of defunct spacecraft will also benefit on-orbit servicing missions which can also be a part of the solution to the space debris issue. In line with this, this study aims to understand the oscillating pattern which we have seen in the spin period evolution of some of the inactive GLONASS satellites inside the AIUB light curve database maintained and produced by the Astronomical Institute of the University of Bern (AIUB) in Switzerland. Beside the light curve data, the database also contains related data including those derived from the light curve itself which are apparent (synodic) spin periods and phase diagrams.

Inactive GLONASS satellites were once part of Russian GLONASS constellation satellites in MEO region. This constellation together with (currently) four other constellations are part of global navigation satellite systems (GNSS). Each constellation consists of around 30 satellites which is the reason why GNSS region has relatively high spatial density since decades ago. It is expected that the density will keep on increasing (hence increasing the probability of collision) especially around the operational altitude of GLONASS satellites. This reality is important in the context of long term sustainability of outer space activity. Coupling this with the fact that all inactive GLONASS satellites are equipped with LRA which will benefit the observational aspect of future research, makes attitude studies of inactive GLONASS satellites exciting.

The AIUB light curve database contains more than 4,800 light curves from more than 540 selected space objects which cover all orbital regions and different types of objects until the end of this study period (November 2020). The light curves were obtained from photometric observations using a 1-m ZIMLAT telescope equipped with a CCD camera located at the Swiss Optical Ground Station and Geodynamics Observatory Zimmerwald (SwissOGS) or Zimmerwald Observatory for short. The planning for the observation, the observation itself, and the processing of the resulting data were performed manually (in general) using AIUB's internal tools on

a daily basis (weather permitting in case of the observation). During the course of this study, a computer program with Windows graphical user interface (GUI) was created to simplify the process of planning and data processing. The program also adds some levels of security by preventing planners to (accidentally) modify the scripts and the database beyond what is necessary.

Each object in the database is characterized by the property of its light curves. The data processing of a light curve will reveal whether it is a stable, a slow rotator, a normal, or an unfinished light curve. A stable light curve indicates that the object was not rotating relative to the station during the acquisition time. A slow rotator light curve indicates that the object was rotating relative to the station but the spin period is larger than the duration of the observation. A normal light curve indicates that the object was rotating relative to the station and the spin period was small enough to allow for a repeating pattern in the light curve. An unfinished light curve indicates that the object was rotating relative to the station but the period cannot be extracted due to complex attitude motions of the objects or other reasons. Only from the normal light curve we can measure the spin period and obtain the associated phase diagram. Basically, a spin period tells us how fast the object rotate around its axis of rotation while a phase diagram tells us about the morphology of the light curve. An object can have only one or a combination of the three light curve types. Based on the historical data of its light curve processing results, an object is classified into one of four attitude groups: rotator group, slow rotator group, stable group, or unknown group. The rotator group is further classified into four groups basically based on the general pattern or trend in the object's spin period evolution: oscillating group, increasing group, decreasing group, and common group (for unknown trend).

Inside the database, there are 42 oscillating rotators, 12 increasing rotators, 26 decreasing rotators, and 107 common rotators. Oscillating rotators appear to display a similar pattern which consists of linear segments and abrupt changes in its spin period evolution that form a series of triangular shapes. Almost all of the oscillating rotators are found in MEO payloads while other groups shows no such preferences. Rotators dominate all orbital regions in the database except the LEO region in which slow rotators dominate payloads and stable objects dominate rocket bodies. While most of rocket bodies are very fast rotators, on the other hand, payloads are more distributed in terms of spin period. Fastest payloads are mostly found in LEO while the slower ones are mostly found in MEO and GEO. Overall, objects' spin periods vary from less than 1 sec to nearly 1500 sec (25 min).

Regarding inactive GLONASS satellites as the main subjects of this study, more than 1800 light curves representing 70 members of the group are available in the database. The whole light curves represent more than 540 hours of observations. Most of the satellites are first generation GLONASS (block IIv) while the rest are GLONASS-M satellites which were launched between 1989 until 2011. On average, they have become debris for more than 10 years when they were first observed by AIUB. Nearly all of them are rotators and we found an indication that all of

them basically possess the oscillating pattern with an increasing or decreasing trend. Regarding the morphology of the light curves, we found that typically four peaks (bright reflections) are present in the corresponding phase diagram despite different shapes. Also, many of the light curves come in 2 pairs of roughly similar shape (typically sharp) but different size. Within one pair, the distance between the peaks is usually around 180°. This morphology can be explained by assuming that it is caused by the four thermal control flaps or radiators which are distributed evenly around the satellite bus. It is interesting that we found three inactive GLONASS satellites which cycle between phases of uniform (normal rotation) and tumbling motion (complex rotation). This phenomenon has also been reported on some GEO satellites in a previous study which proposes the Yarkovsky-O'Keefe-Radzievskii-Paddack (YORP) effect as the responsible driving force. In addition, we also found one object which is stable although it has become a debris for at least seven years.

There are 18 oscillating inactive GLONASS satellites which maintain a triangular pattern (with different levels of confidence due to the number of observations available) until the end of our study period. We call those objects *the main objects* for this study. All the main objects have at least 23 observational data and have been observed between five and six years. In total, 652 light curves of the main objects are available in the database which represent more than 154 hours of observations. They are usually observed using 1 sec of exposure time with no filter.

The characterization the oscillating pattern of the main objects' spin period evolution was performed by using an assumption that the variations in the evolution can be modeled by a series of triangular shapes having similar slopes for the left and right segments. This resulted with an empirical model for each object. Using statistics, we found that the average spin period of the main objects varies greatly from 8.11 sec to 469.58 sec which is similar to the average cycle amplitude which varies from 1.10 sec to 513.24 sec. On the contrary, the average cycle period only varies slightly from 0.78 years (285.10 days) to 1.35 years (494.22 days) and its mean and median values are close to 1 year (365.25 days). We also found that the average spin period correlates well with the average cycle amplitude. Interestingly, we found that, overall, the main objects tend to get faster during their lifetime and objects with higher spin rate tend to accelerate more.

From the modeling and simulation of a selected main object, we found that the (roughly) annual oscillating pattern is achievable only if the solar panels are oriented differently. In other words, the two solar panel are canted, which provides an asymmetry to the satellite model. The larger the cant, the larger the amplitude of the oscillating pattern. Moreover, this seems independent of the initial orientation of the satellites and of the rotation axis (which are the other two parameters that define the initial condition of the simulations). However, the repeating (roughly) *triangular shape* can only be achieved if the model was initially oriented as it looks in Fig. 5.1 (the figure is taken from Chapter 4 and displayed here for clarity). Specifically, the long side of the bus was parallel to the radial line and the axis of the solar panel was parallel to the cross track line. In addition, the angular velocity

was only applied to the body-axis parallel to the along track line.
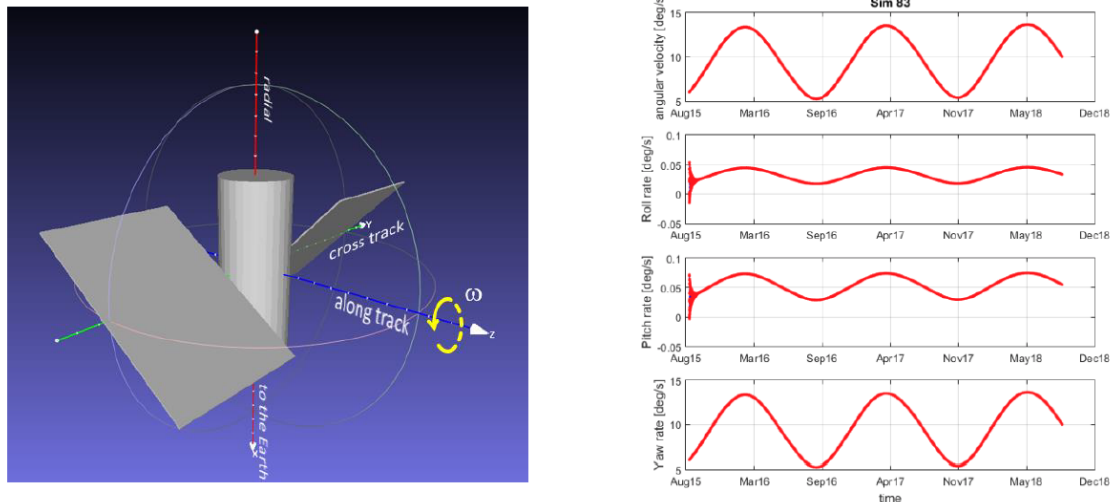
Figure 5.1.: The condition of solar panel with respect to the body frame and the initial orientation of the satellite with respect to the orbital frame which successfully produced an oscillating pattern with a period around one year (left image) and the result of the simulation (right image). On the left image, ω is the angular velocity.

After evaluating all the environmental forces acting on the satellite (SRP, third body forces, eddy current damping, and gravitational torque) in the simulation, we found that the only force that may be responsible for the oscillating pattern is the SRP. The canted solar panel allows a mechanism similar to a wind wheel or fan to work on the system. Depending on the relative orientation of the incoming radiation to the axis of rotation which switches over every approximately half a year, SRP produces a torque on each of the solar panel resulting on an increase or decrease of the spin rate. When the incoming sunlight exerts a pressure whose direction is negative with respect to the surface's unit vector direction, the pressure produces a torque on each of the solar panel which altogether contributes to the rotation by increasing the spin rate. Later, when the orientation of the solar panels with respect to the incoming radiation is flipping (after roughly half a year) as the Earth is revolving around the Sun, it makes the angular acceleration to be directed in counter-spin direction for the following roughly half a year period decreasing the rotation. Another feature, the secular trend of the spin period evolution, is a result of different values of the specular reflection coefficients of front side and back side of the solar panels which is something common.

The regularity of the pattern found on the main objects allows us to use the empirical models to estimate the spin period on any date (covered by the historical data) by using interpolation. The period estimation can be performed even further in the

future (or in the past) if we can assume that the pattern is preserved as we found on the six objects which have a nearly linear trend. It is interesting to see how other objects deviate from the linear trend since it may indicate particular events such as collision with debris, etc.

5.2. Outlook

We have identified several points that we considered necessary to be performed in the future to improve the quality of the photometric related activity at AIUB and will also benefit the photometric study of space debris in general.

1. Evaluating the result of data processing in AIUB light curve database for interesting objects with several years of spin period evolution. This is to verify supposedly erroneous period values which can be identified by inspecting their conformity with the associated object's spin period evolution. The initial value for the correction can be obtained through interpolation using adjacent data points with convincing period values.

2. Using SLR for defunct GLONASS satellite observations. All GLONASS satellites are equipped with LRA, which can inadvertently act as cooperative targets for laser instruments. This allows the objects to be observed not only by optical telescopes, but also with laser equipment. The possibility to observe them using multiple observation techniques opens up the possibility of gaining more insights into their characteristics. In fact, this approach has been experimented at AIUB in conjunction with data processing to obtain the satellite's attitude states. Resuming this effort could yield valuable results and contribute to a better understanding of these defunct satellites.

3. Upgrading the optical observation system by using a faster CMOS camera for routine photometry and implementing a fully automatic system for photometry. The CCD camera which was used for this study is considered sufficient for the study purpose but for significantly faster rotating objects, a faster camera with more sensitivity is necessary to optimize the observations. A fully automatic system which covers planning, observation, and data processing is also necessary to optimize the photometric activity. Minimizing human interventions in all phase of the activity can also improve the accuracy of the results. A dedicated telescope for photometry may be necessary.

4. Considering the unique characteristics of the inactive GLONASS satellites as described in this study, it is necessary to perform another special campaign for this group. Using the planning setup during this study period, on average only 10 inactive GLONASS satellites were observed every 13 days. In other words, only 1 object per day, on average. This made it impossible to update each object in the database at least once per month which is considered necessary to capture the dynamics.

5. Considering the great potential of iOTA software for attitude study of space debris, it is necessary to improve and expand its capability and optimize its computing performance. During the course of this study, several points to improve have been identified such as the capability to give different optical properties of satellite's components and the improvement of the feature to simulate light curves. iOTA should also take into account the YORP effect in the simulation as it seems significant for a more complete understanding of solar radiation effect on spacecrafts.

6. A study which reanalyzes the main objects using iOTA with YORP effect will be interesting. Especially for the three objects that cycle between phases of uniform (normal rotation) and tumbling motion (complex rotation) which we found in this study. A special campaign for those objects will be necessary to obtain enough data points.

7. Collaborating with other institutions for photometry activities of interesting targets. This is necessary to improve especially the observation aspect of the activity since a comprehensive high quality photometric characterization of space debris can only be obtained through several stations which are widely separated across the globe.

A. The Main Objects

This appendix contains graphs of spin period evolution of all the main objects together with their empirical model described in Chapter 4. In each empirical model, green lines are segments which connect adjacent peaks while red lines runs through each center of all applicable segments (only the ones joining two peaks) to represent the average dynamics of the evolution. Each segment is labeled with a number. Red dots represent peaks.
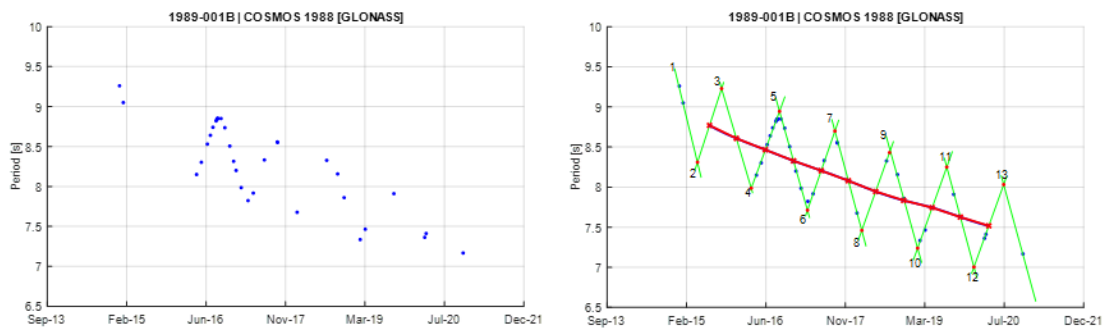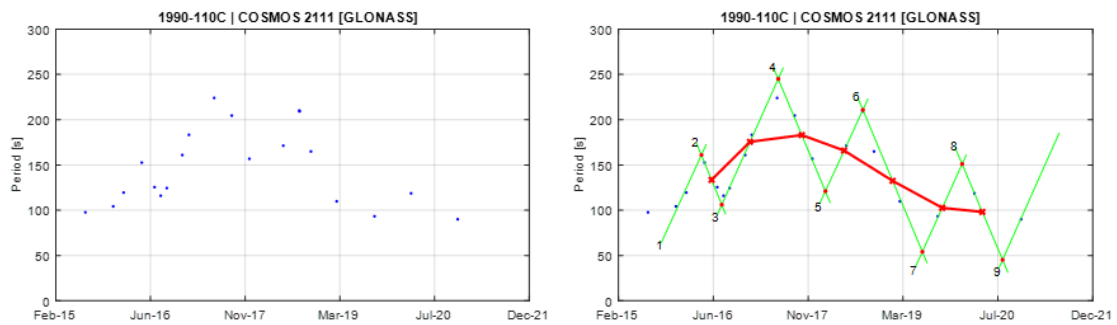

Figure A.1.: Observational data of spin period evolution of COSMOS 1988 (left) and its empirical model (right). Segment 4 and 5 are used to create the principal triangular shape.
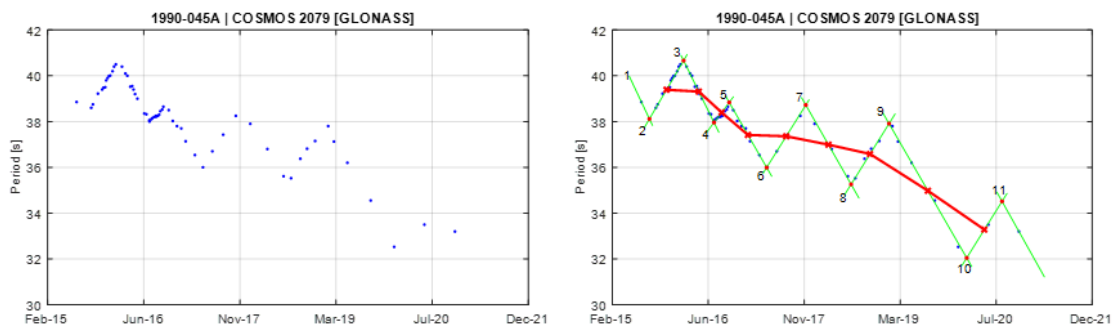
Figure A.2.: Observational data of spin period evolution of COSMOS 2079 (left) and its empirical model (right). Segment 2 and 3 are used to create the principal triangular shape.
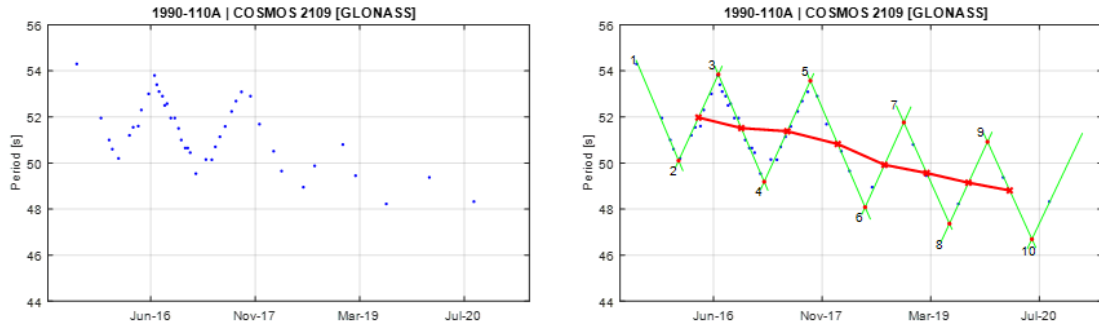
Figure A.3.: Observational data of spin period evolution of COSMOS 2109 (left) and its empirical model (right). Segment 2 and 3 are used to create the principal triangular shape.
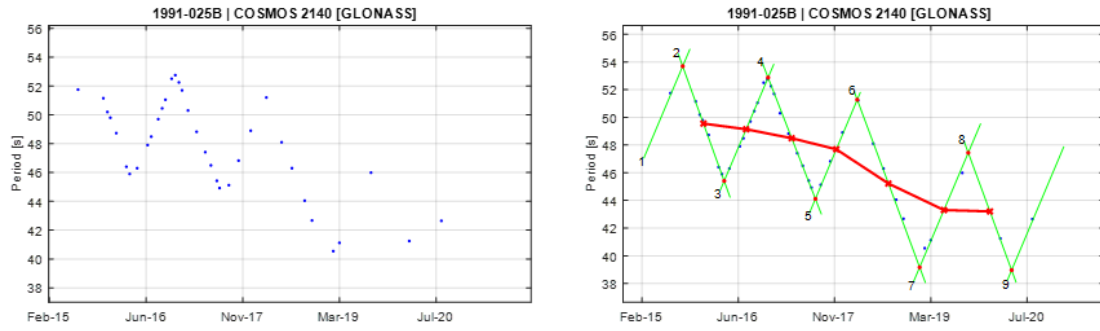

Figure A.4.: Observational data of spin period evolution of COSMOS 2111 (left) and its empirical model (right). Segment 3 and 4 are used to create the principal triangular shape despite the difficulty in selecting the two appropriate segments due to the low number of data points.
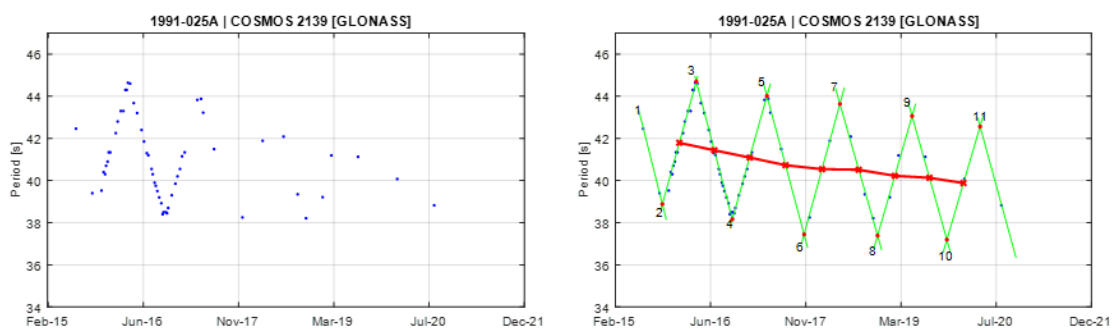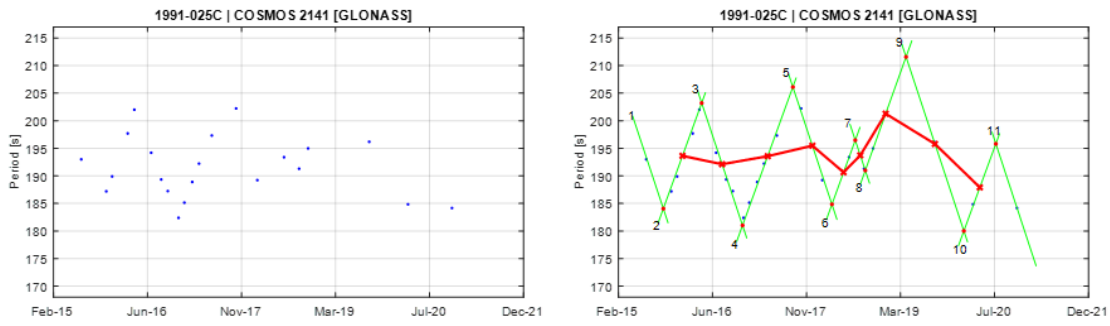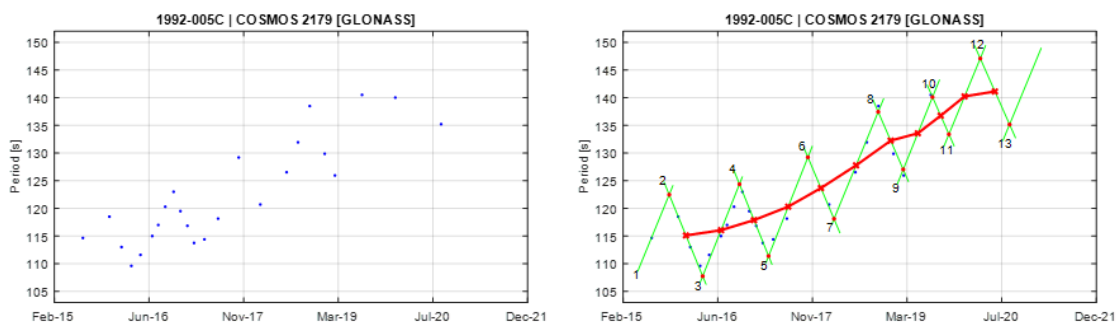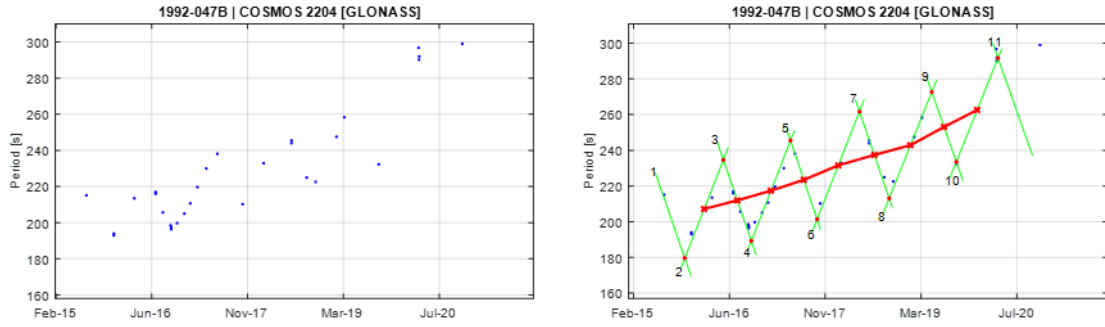

Figure A.5.: Observational data of spin period evolution of COSMOS 2139 (left) and its empirical model (right). Segment 2 and 3 are used to create the principal triangular shape.

Figure A.6.: Observational data of spin period evolution of COSMOS 2140 (left) and its empirical model (right). Segment 3 and 4 are used to create the principal triangular shape.
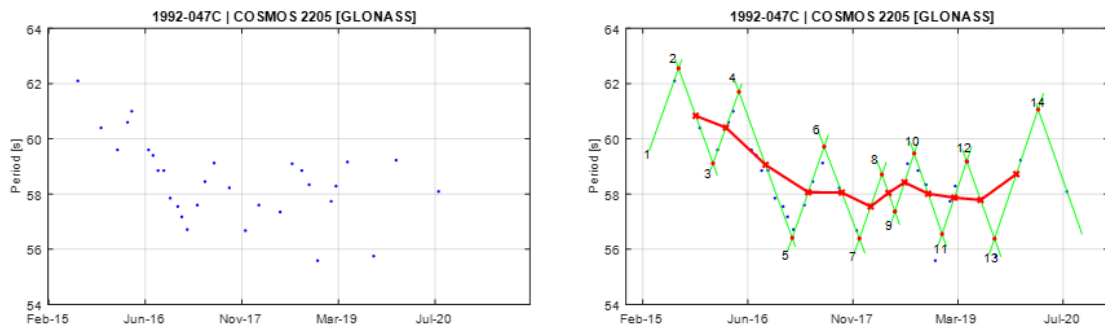

\

Figure A.7.: Observational data of spin period evolution of COSMOS 2141 (left) and its empirical model (right). Segment 2 and 3 are used to create the principal triangular shape.
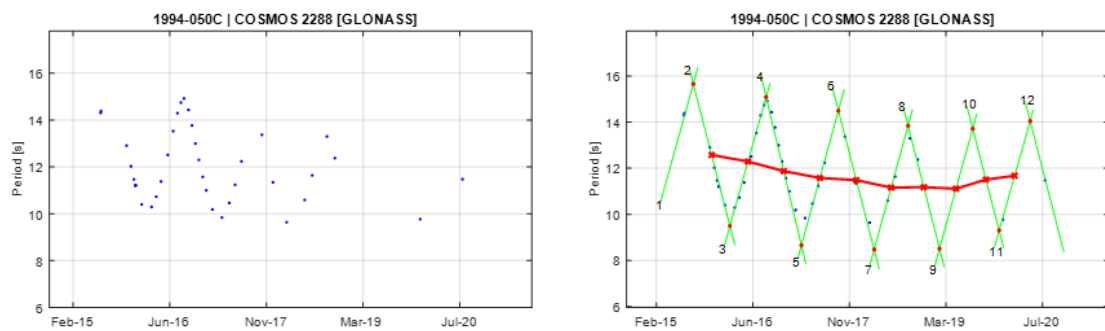

Figure A.8.: Observational data of spin period evolution of COSMOS 2179 (left) and its empirical model (right). Segment 3 and 4 are used to create the principal triangular shape.
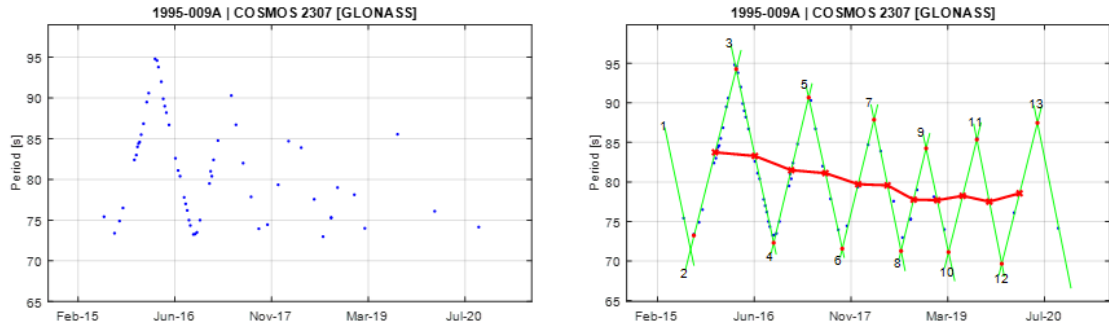
Figure A.9.: Observational data of spin period evolution of COSMOS 2204 (left) and its empirical model (right). Segment 3 and 4 are used to create the principal triangular shape.
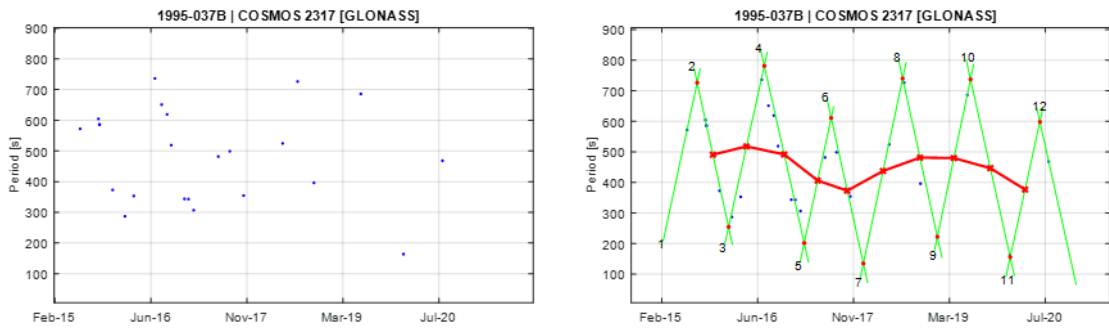

Figure A.10.: Observational data of spin period evolution of COSMOS 2205 (left) and its empirical model (right). Segment 4 and 5 are used to create the principal triangular shape.
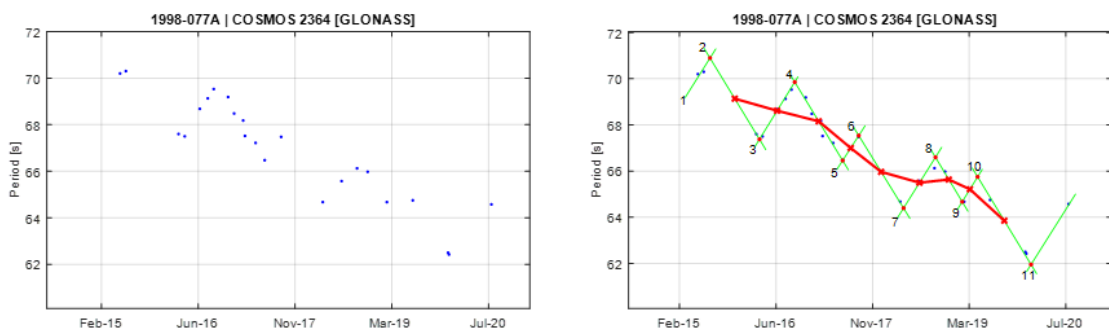

Figure A.11.: Observational data of spin period evolution of COSMOS 2288 (left) and its empirical model (right). Segment 3 and 4 are used to create the principal triangular shape.

Figure A.12.: Observational data of spin period evolution of COSMOS 2307 (left) and its empirical model (right). Segment 2 and 3 are used to create the principal triangular shape.

Figure A.13.: Observational data of spin period evolution of COSMOS 2317 (left) and its empirical model (right). Segme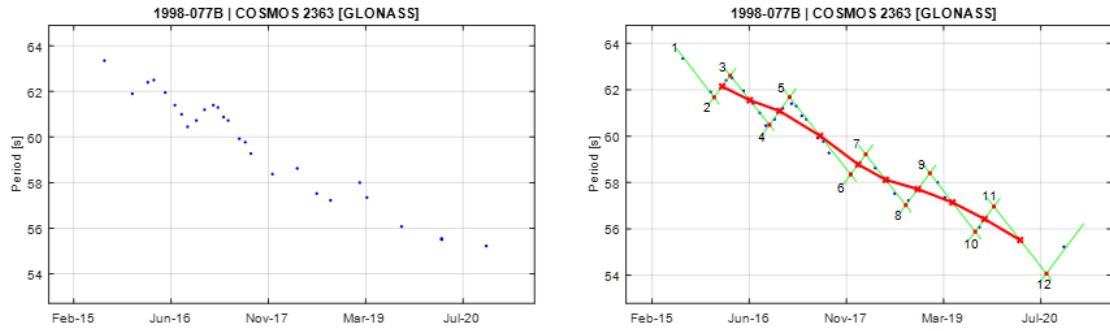nt 3 and 4 are used to create the principal triangular shape despite the difficulty in selecting the two appropriate segments due to the low number of data points.
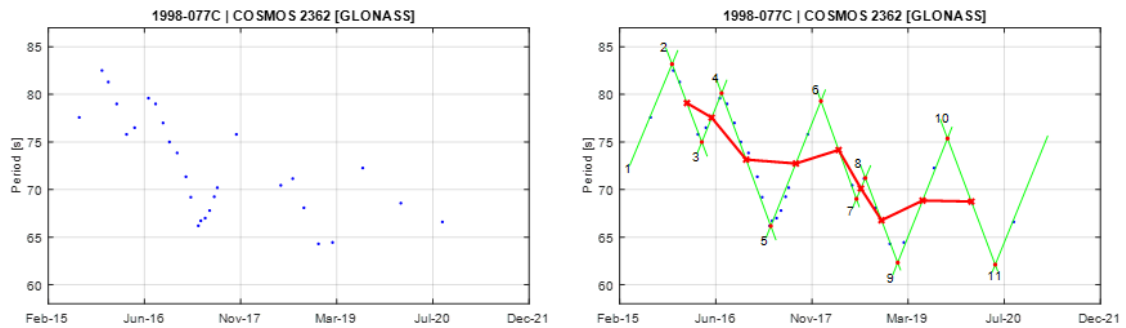

Figure A.14.: Observational data of spin period evolution of COSMOS 2364 (left) and its empirical model (right). Segment 3 and 4 are used to create the principal triangular shape.

Figure A.15.: Observational data of spin period evolution of COSMOS 2363 (left) and its empirical model (right). Segment 4 and 5 are used to create the principal triangular shape.

Figure A.16.: Observational data of spin period evolution of COSMOS 2362 (left) and its empirical model (right). Segment 4 and 5 are used to create the principal triangular shape.

Figure A.17.: Observational data of spin period evolution of COSMOS 2395 (left) and its empirical model (right). Segment 5 and 6 are used to create the principal triangular shape despite the difficulty in selecting the two appropriate segments due to the low number of data points.
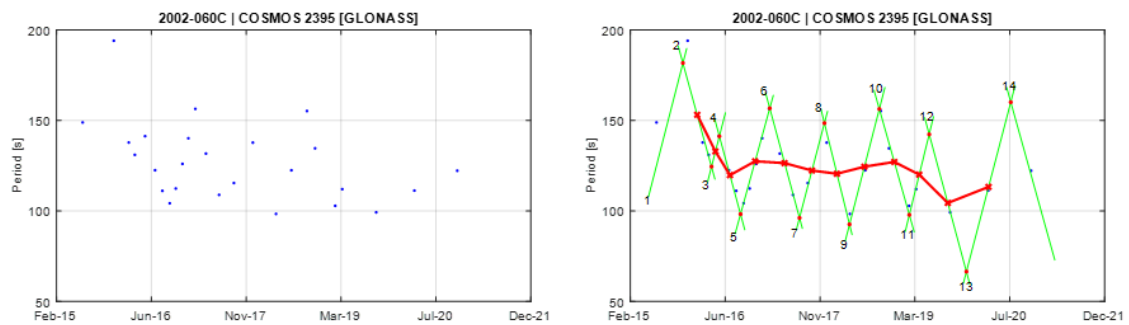
Figure A.18.: Observational data of spin period evolution of COSMOS 2404 (left) and its empirical model (right). Segment 2 and 3 are used to create the principal triangular shape.
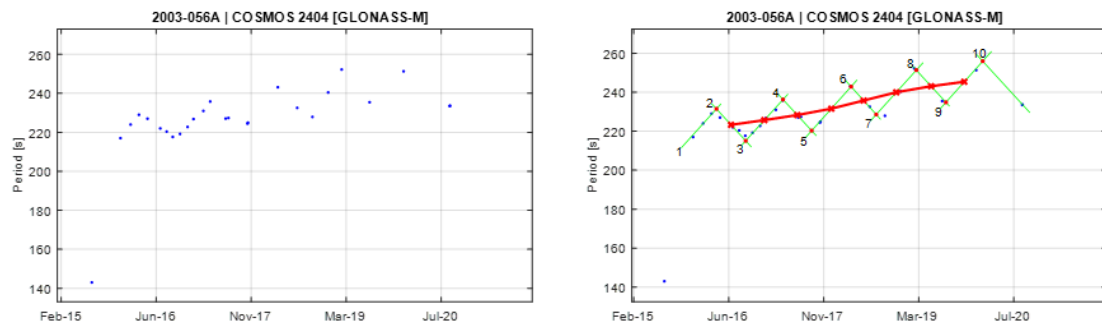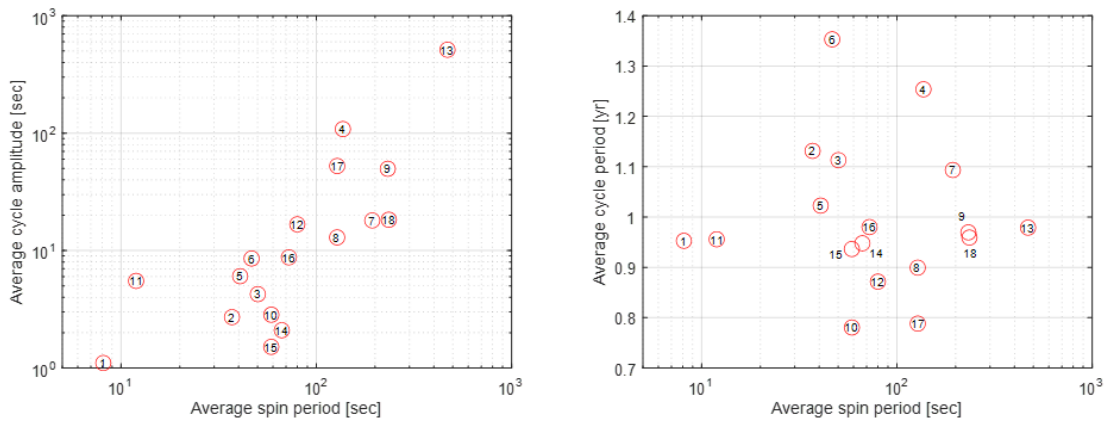
B. Relationship between Parameters of Spin Period Evolutions

This chapter contains relationships between the parameters for characterizing spin period evolutions of the main objects as listed in Table 4.2. For each figure, circles correspond to the objects and number inside the circles indicates the object's number in the table.

Figure B.1.: Relationship between average cycle amplitude and average spin period (left) and that between average cycle period and average spin period (right).
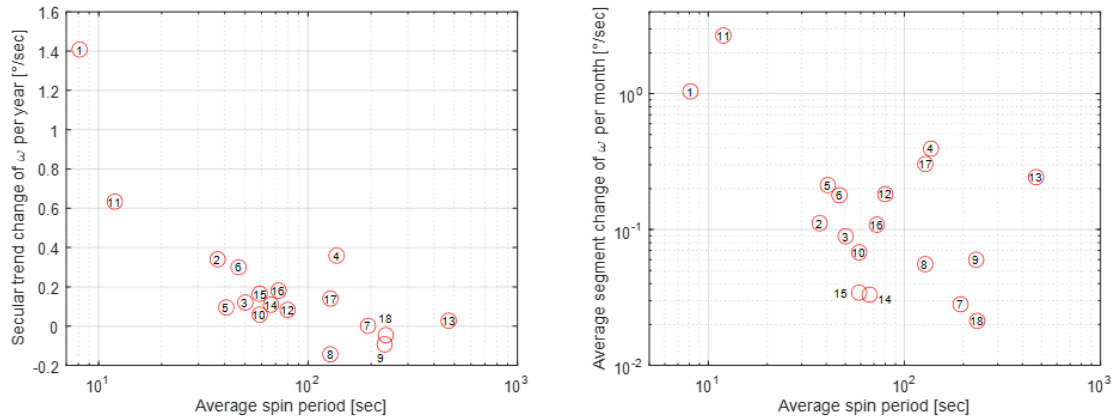
Figure B.2.: Relationship between secular trend change of angular velocity ω per year and average spin period (left) and that between average segment change of angular velocity ω per month and average spin period (right).

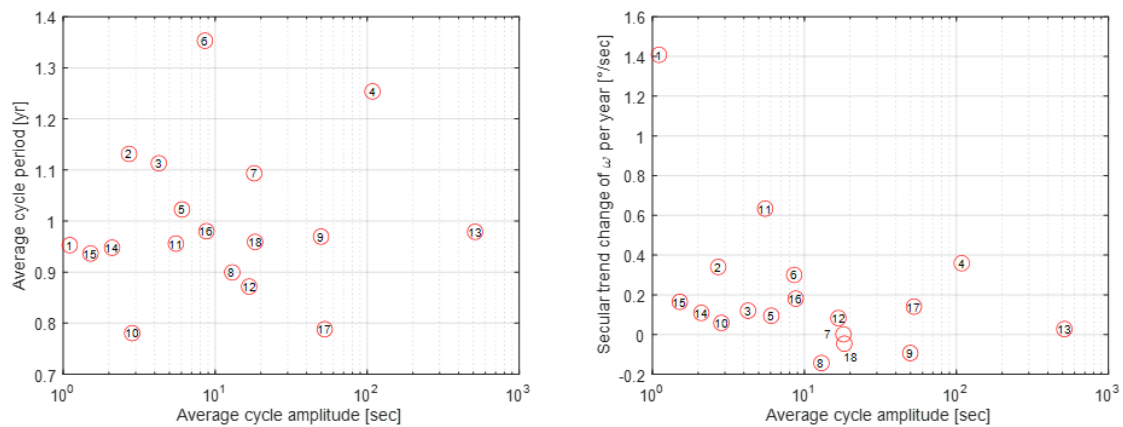

Figure B.3.: Relationship between average cycle period and average cycle amplitude (left) and that between secular trend change of angular velocity ω per year and average cycle amplitude (right).

Figure B.4.: Relationship between average segment change of angular velocity ω per month and average cycle amplitude (left) and that between average segment change of angular velocity ω per month and secular trend change of angular velocity ω per year (right).
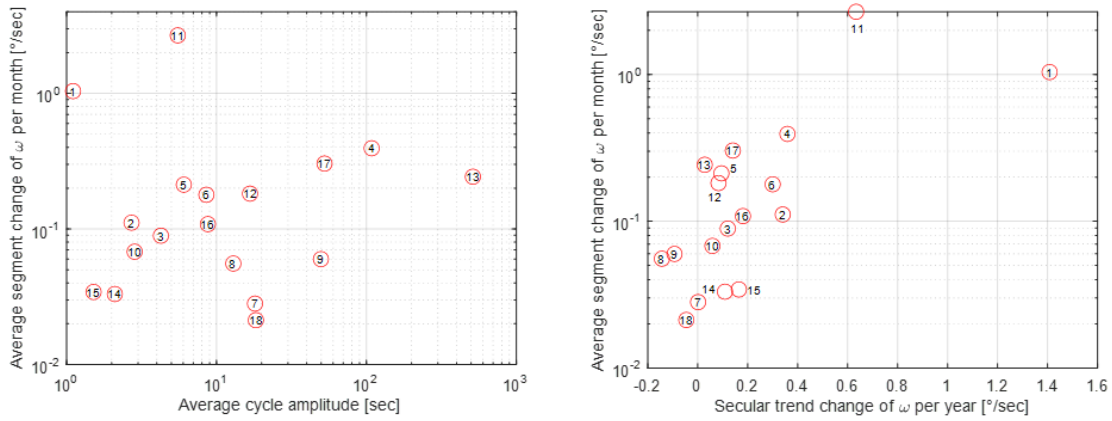

Figure B.5.: Relationship between secular trend change of angular velocity ω per year and average cycle period (left) and that between average segment change of angular velocity ω per month and average cycle period (right).
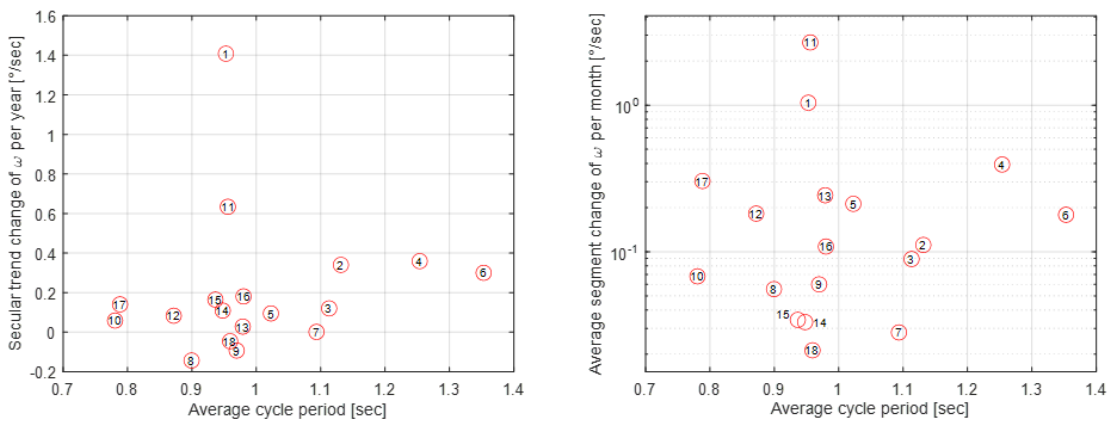
C. AIUB Phototool

This appendix explains briefly the AIUB Phototool. Since there is no user manual written for the software yet, further information including troubleshooting can only be obtained from experienced users. The chapter starts with describing main features of the tool in Section C.1 and ends with describing the main menu and some important context menus (available through right mouse button) in Section C.2. The tool was created using Delphi 2010 programming language since November 2016 and only runs on Windows platform with Java Runtime Environment installed. It was designed to encapsulate nearly all scripts and programs already available for doing routine photometry planning and data processing at AIUB while also adding some useful features. By the encapsulation, the program also adds some levels of security by preventing planners to (accidentally) modify the scripts and the database beyond what is necessary.

C.1. Main features

AIUB Phototool can be operated in four modes as discussed in Section 3.1 (Fig. C.1). Basically, it consists of a main menu (Fig. C.7) and two tabs which are the planning tab and the processing tab. After copying all the necessary files to the local storage and running the program (and selecting one of the modes), the first thing to do is to set up the environment by going to the Setting menu in the main menu. Here, several parameters can be set such as the main folder path which is the location of all the planning and processing files and the allocated time for photometry observations which will limit the number of objects that can be observed in a given night.
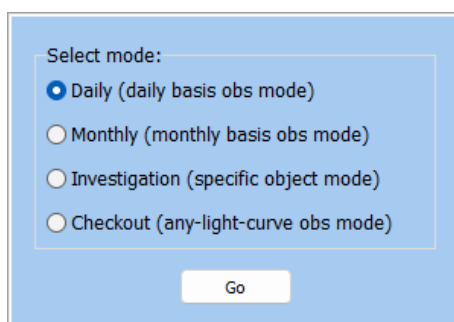

Figure C.1.: The four modes in the AIUB Phototool.

Planning tab

The planning tab contains four main parts as shown in Fig. C.2. Their description is described below.

Part-1 contains four buttons which should be executed sequentially from top to bottom. This part will process the data obtained from previous observations (the first two buttons) and prepare for the next observation (the last two buttons). Internally, three of the buttons will call three executable Java Jar files which are responsible for the associated functions. Planning for several dates ahead is possible.

Part-2 shows data for planning which is created after clicking the third button in Part 1. The data should be inspected and modified manually if necessary (e.g., changing the exposure time from the default value). Two functions are available to prioritize a selected object or to ignore it on the date of observations. In trying to make sure that an object will be in the list of selected objects to be observed, ignoring an SLR priority pass (which is normally forbidden) can even be performed by deleting the line for the pass. Other functions are available to save the changes or undo the changes completely by restoring the original data.

Part-3 shows a list of selected objects based on the final data for planning for the selected date and the criteria discussed in Section C.2. Clicking one of the object will display all the special groups where the object belongs to in the Light curve image panel window (as seen in Fig. 3.3). This information can be useful in manually managing the priority of the selected object which can be performed by using the "priority button" or the "ignore button" in Part 2. Historical data about the selected object can be accessed by clicking the PROCESSING button. A complete list of the special groups can be accessed from the View menu in the main menu. Several functions are available by right clicking an object such as putting the object in *To be ignored list.*

Part-4 shows three links to show the outputs of the planning process in two formats which are chart format (e.g., Fig. 3.4) and text format. There is also a link to show the list of SLR priority passes which are considered in creating the output, as photometry observations should not be in conflict with priority passes for SLR observations.

Several other functions are available to further ease and customize the on-going planning which can be accessed from the View menu (Fig. C.7). For example, by inspecting the *To be observed again list* (which is created in the processing phase) and the *To be ignored list* (which is created in the planning phase). Current status of the AIUB photometric observation activity can also be obtained from the menu by clicking the *Observation status.* In the Observation status window, users can see, for example, which objects are currently monitored or skipped in the pipeline. In
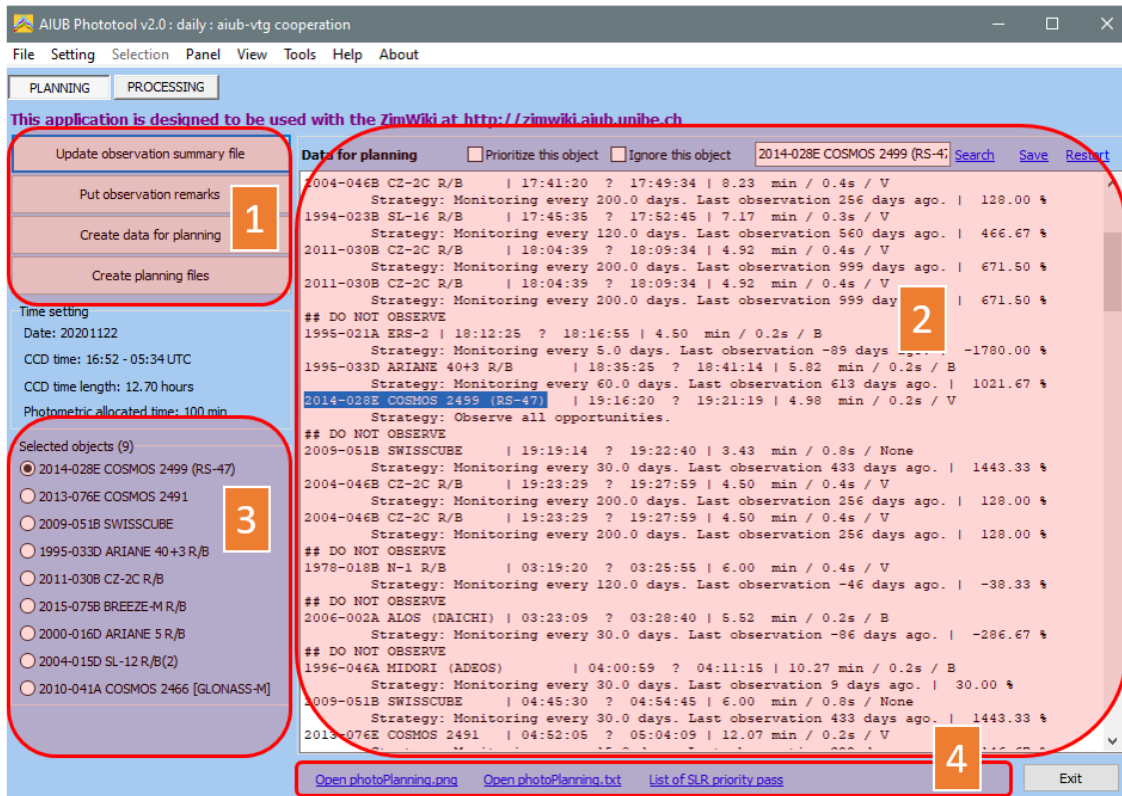
Figure C.2.: Main parts of the Planning tab of the AIUB Phototool.

the same window, they can also access the ONF chart which is discussed in Section 3.1.

Processing tab

The processing tab contains five main parts as shown in Fig. C.3. Their description is described below.

Part-1 shows a summary of observation results. This should be updated on a daily basis using the first two buttons of the Part 1 in the planning tab. Although users cannot directly modify the content (to prevent accidental errors), there is a procedure to update period values (if considered necessary) through the context menu. The menu contains many other functions as well which depend on whether users select an object (Fig. C.8) or an observation (Fig. C.9). If sub windows are displayed through the Panel menu, Selecting an object will show its observational setting and its special groups as shown in Fig. 3.3 while selecting an observation will show its light curve and the related phase diagram (Fig. C.4). Either of the selections will affect other parts (Part-3, Part-4, and Part-5) accordingly. The light curve image and the upper phase diagram image

are both auto-generated and users can modify their appearance (among other things) by interact with the images by dragging with the mouse (with left or right button) or right clicking on the image to access several functions (Fig. C.10 and Fig. C.11). For example, users can process only some part of the light curve by zooming-in the image and recreate the phase diagram. Users are also allowed to delete any data points (through the context menu) which is sometimes necessary for example to delete outliers. The phase diagram is actually available in two periods to allow users to customize the phase by dragging the image with the right mouse button. Both the light curve and the phase diagram images can be resized as necessary.

Part-2 contains a list of observations (or light curves) to be processed. Several functions are available to ease the process either displayed on the area or through the context menu. When the tool is closed, the program remembers the position of the last observation processed.

Part-3 shows the period evolution of the selected object. Several functions are available for users to interact with the graph by dragging with the mouse (with left or right button) or right clicking on the image to access the context menu. For example, they can click any data point to locate the observation line in the summary of the observation results. Other functions through the context menu can be seen in Fig. C.12. The image can be undocked from the container and resized as necessary. Users are also allowed to delete any data points (through the context menu), which is sometimes necessary for example to better evaluate the period evolution patterns.

Part-4 contains two MATLAB commands. The first will guide users to navigate according to the routine analysis of light curve data displayed in Fig. 3.10. The second command will run the iterative process of finding the period using the PRM method. When running the first command, the result of the the detrending should be evaluated. If the default value which is 15 (the last parameter in the command) distorts the original pattern of the light curve too much (which can be witnessed in one of the output images) then lower down the value. A significantly lower value such as 5 usually gives better result.

Part-5 shows notes on the selected object or light curve. The notes are not only important since they give related information but also, in the case of an object, contain inputs to create statistics of the database and a summary table (Fig. C.5) which are accessed through the main menu (View | summaryTable and statistics). The statistics and the summary table can be used in a special Excel file (Fig. C.6) to produce most of the graphs and tables in Section 3.4.
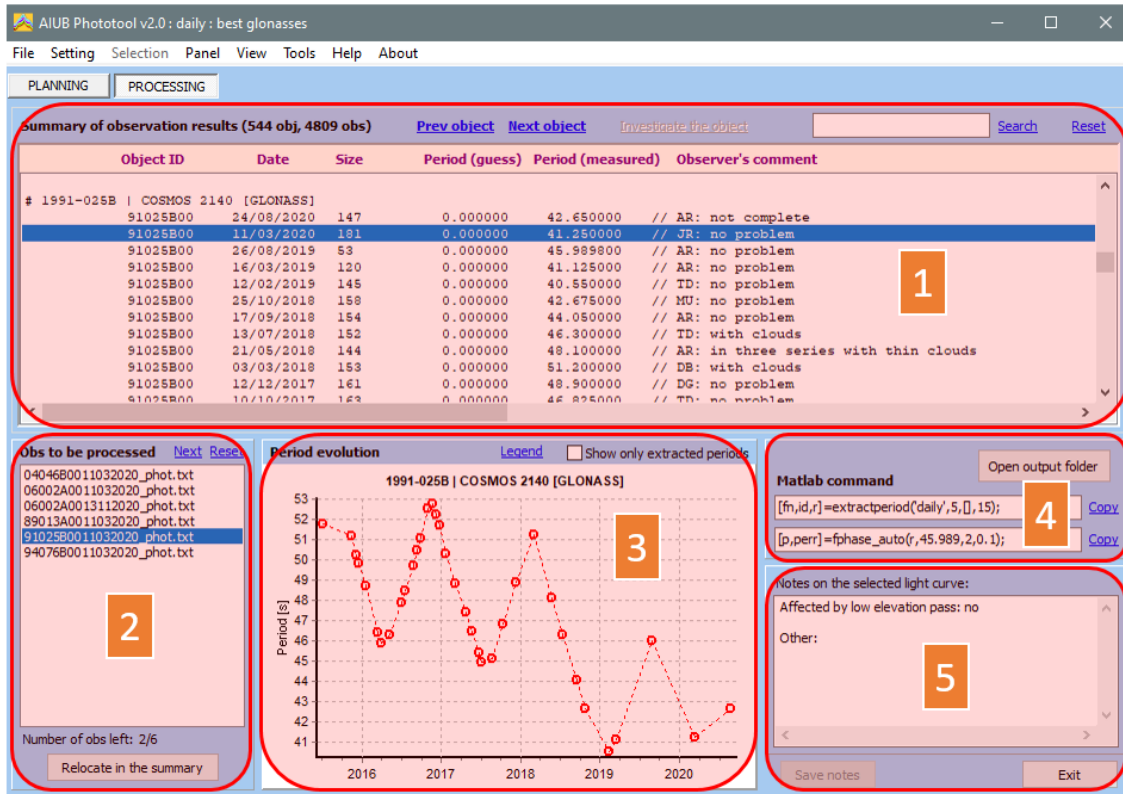
Figure C.3.: Main parts of the Processing tab of the AIUB Phototool.

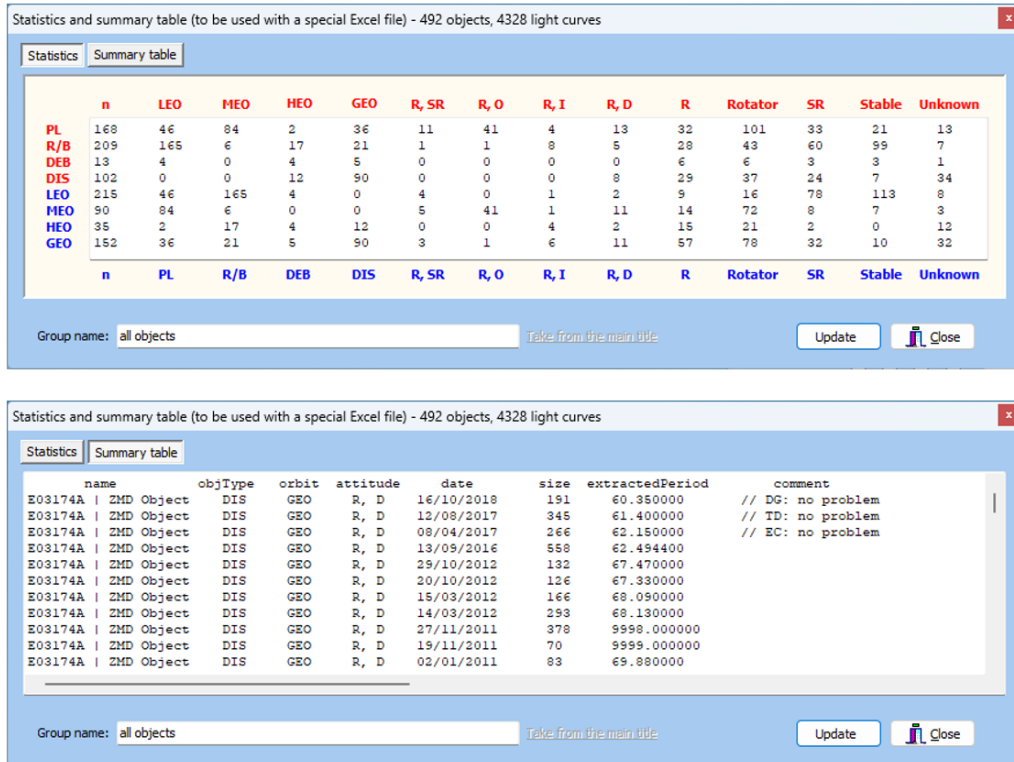**Figure C.4.:** The Processing tab with all sub windows opened.

Figure C.5.: Statistics and summary table window.
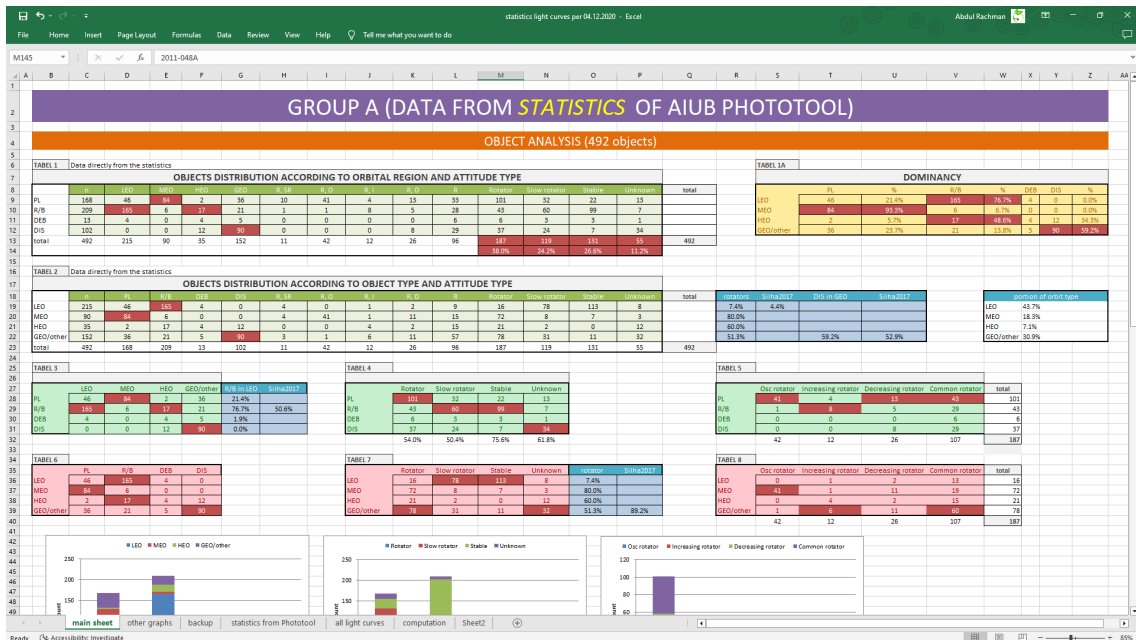

Figure C.6.: The special Excel file to produce graphs and tables for reports.

C.2. Menus
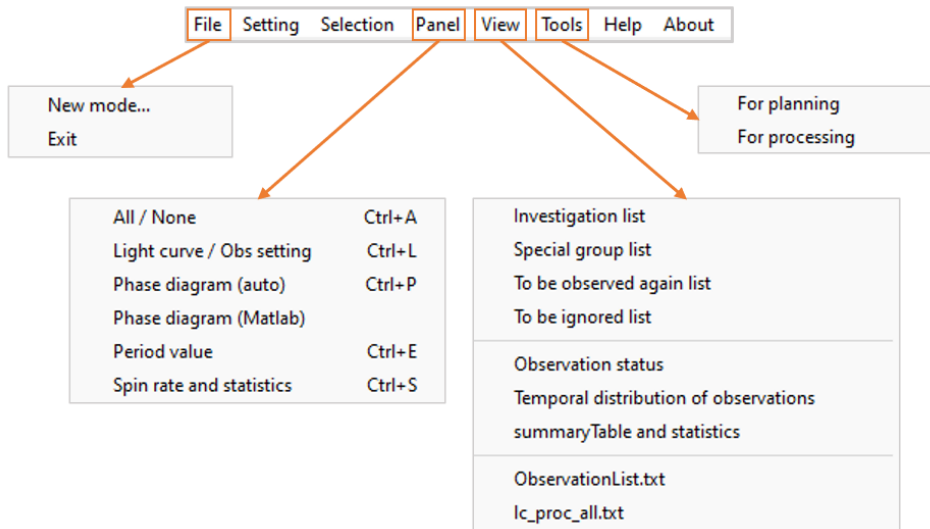
Figure C.7.: Contents of the main menu.
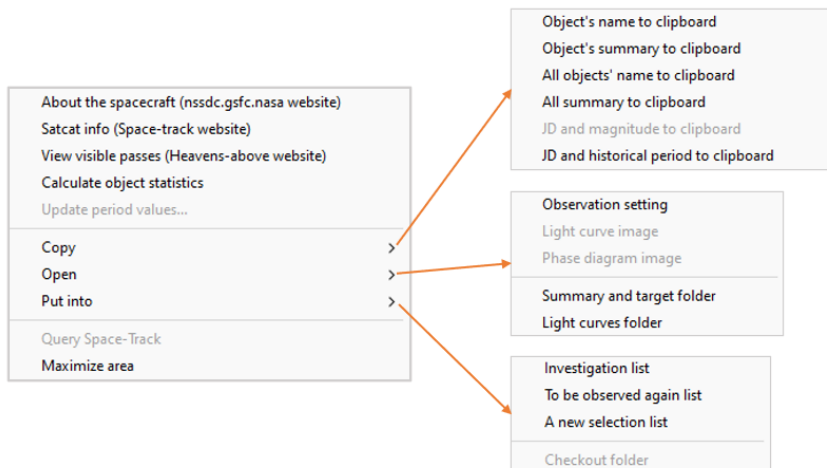
Figure C.8.: Contents of the context menu for a selected object in *Summary of observation results*.
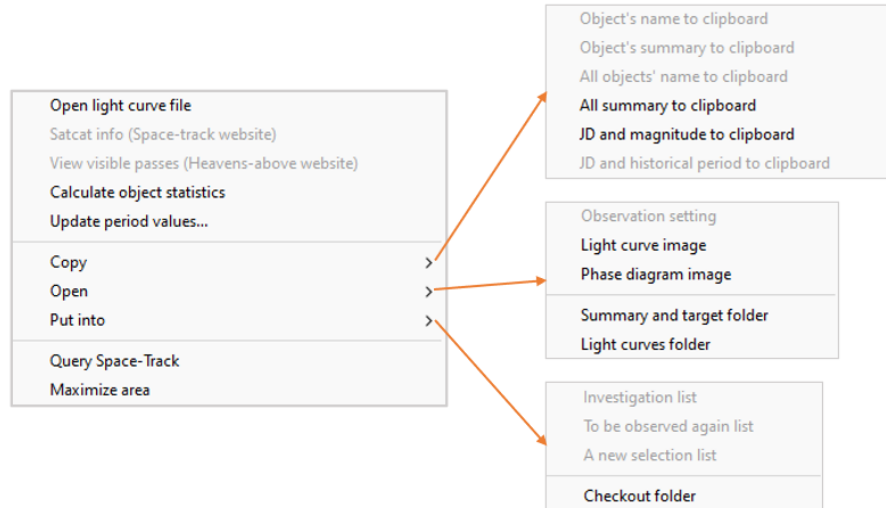
Figure C.9.: Contents of the context menu for a selected observation in *Summary of observation results*.
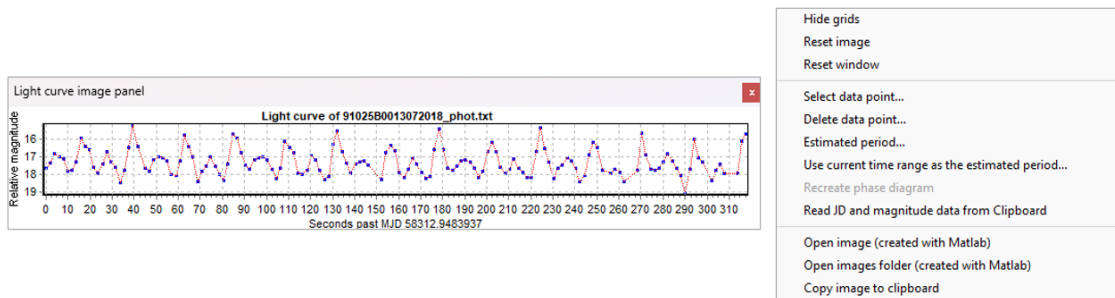

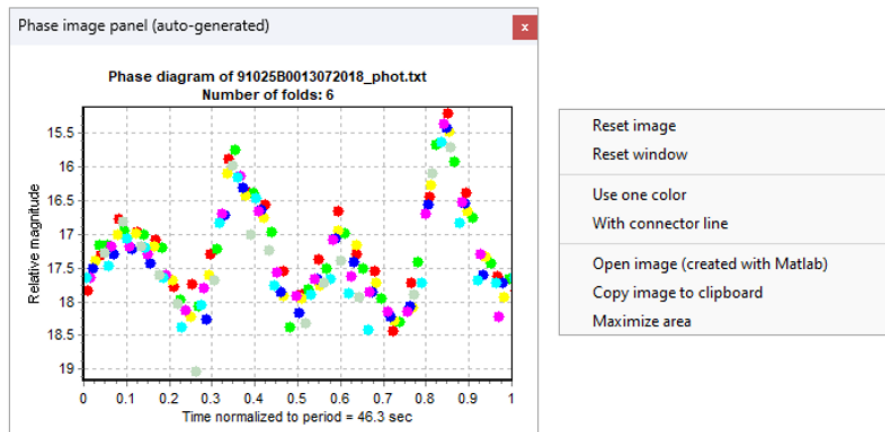**Figure C.10.:** Light curve image and the contents of its context menu.

Figure C.11.: Phase diagram image and the contents of its context menu.
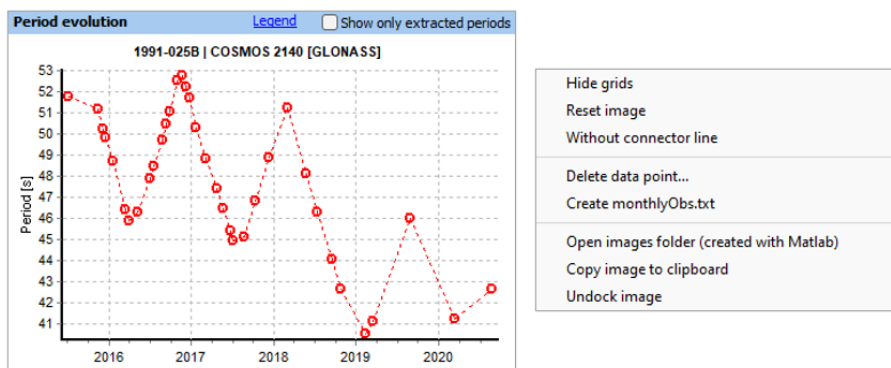
Figure C.12.: Period evolution image and the contents of its context menu.

D. Light Curve Morphology of Inactive GLONASS Satellites

Both type IIv and type M of GLONASS satellites include radiators for their thermal control. Fig. D.1 shows the shape and location of the four radiators for GLONASS satellites which apparently are distributed equally around the bus (and this will be our assumption). We can see from the figure that the radiators are quite big (given the length of the bus is around 4 m) and they are bright. Also, the shape of each radiator looks similar which is a curve rectangular. In terms of their direction of opening, we can see that the radiators are arranged into two pairs ("clockwise pair" and "counter clockwise pair") where each member of a pair is separated by 180°.
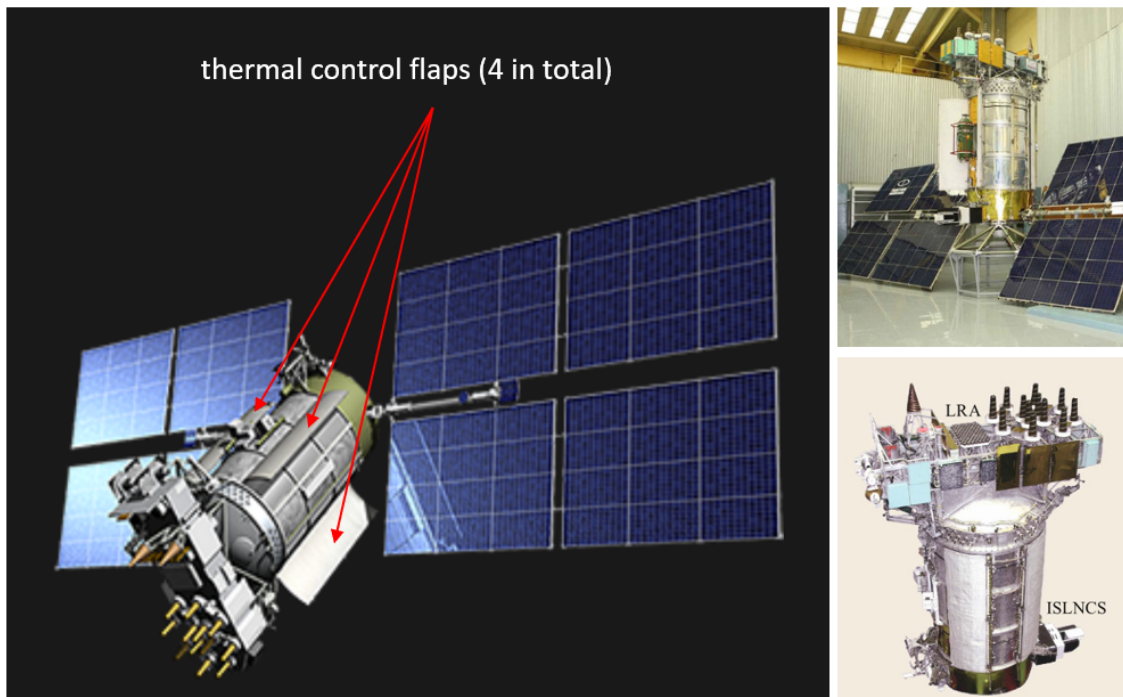
Figure D.1.: GLONASS satellites use four flaps as part of their thermal control. Images are taken from the internet and from *Revnivykh et al.* (2017).

Fig. D.2 shows four phase diagrams of an inactive GLONASS satellites which represent the typical light curve morphology of the group in which the light curves come in 2 pairs of (more or less) similar shape but different size. Also, the distance

between the peaks within one pair is usually around 180° and the peaks are sharp. In many occasions, one pair is significantly smaller than the other.
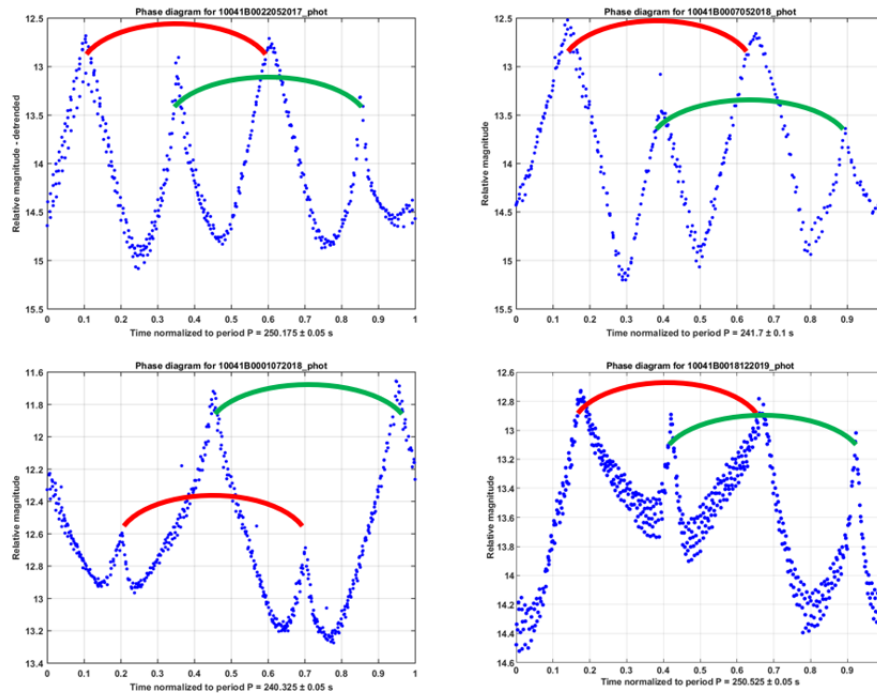
Figure D.2.: Phase diagrams of inactive GLONASS satellites typically show four peaks in two pairs. The two pairs are identified by two arcs of different color.

In Section 3.5 we discussed that although a specular reflection can also come from solar panels, they are not likely to be the reason for the li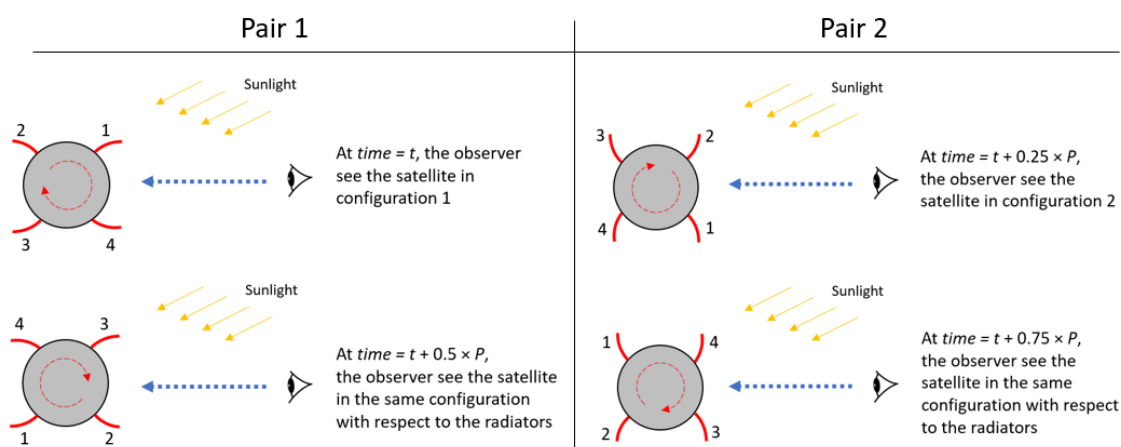ght curve morphology of inactive GLONASS satellites we saw. Fig. D.3 explains how the arrangement of the radiators on the bus allows an observer to have similar profile of peaks within one pair which are separated by 180° as shown in the morphology. As we see in the figure, at $time = t$, the observer see the satellite in a specific configuration with respect to radiators (configuration 1) which gives a specific brightness. Half of a period later ($time = t + 0.5 \times period$), the observer see the satellite in the same configuration again with respect to the radiators hence (supposedly) similar brightness. Therefore, this repeating similar configuration will allow the observer to have one of the two pairs in the light curve morphology. The other pair will be obtained at $time = t + 0.25 \times period$ and $time = t + 0.75 \times period$ when the observer see the satellite in another configuration (configuration 2).

Figure D.3.: A simplified scenario to explain the light curve morphology of inactive GLONASS satellites. The bus on the left is looked from one of its end. The four radiators are marked with numbers. In this illustration, the bus is rotating clockwise around its (supposedly) minimum axis of inertia. P is the spin period of the satellite.

E. Inactive GLONASS Satellites with Tumbling State

This appendix contains spin period evolutions of the three GLONASS satellites which we assume to cycle between normal rotation and tumbling or complex rotation. They have been discussed at the end of Section 3.5. We can see that both COSMOS 2236 (Fig. E.1) and COSMOS 2275 (Fig. E.2) started their spin period evolution "normally" but later their spin periods become much larger and complex at many points of their evolution. Unfortunately not so much data for COSMOS 2411 (Fig. E.3) is available as for the other two.
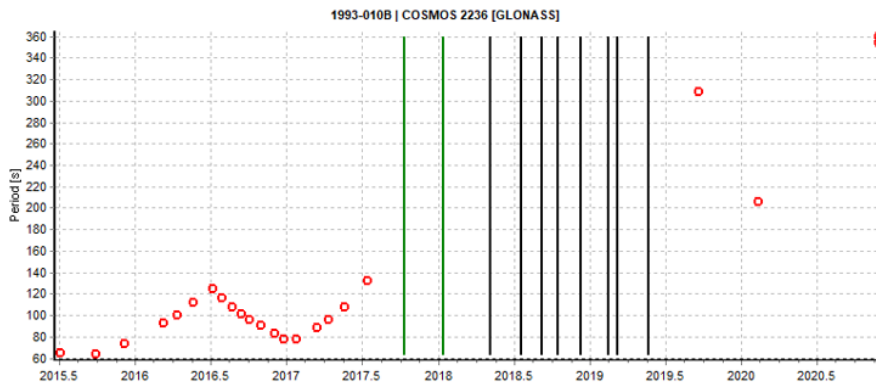
Figure E.1.: Spin period evolution of COSMOS 2236. Red circles indicate periods, black lines indicate slow rotator light curves, and green lines indicate unfinished light curves (due to their complexity).

If we compare the shape of the normal phase between the three objects and that of the main objects then we can spot a dissimilarity. While the normal phase of the main objects increases linearly (towards a peak of the triangular shape), that of the three objects apparently increased asymptotically. This can be easily seen in the case of COSMOS 2275. This asymptotic behavior looks similar to the case of GOES-8 satellite (Fig. E.4). In the figure, we can see how the periods increased asymptotically which means that the satellite's spin rate was going slower and slower towards zero. *Albuja et al.* (2018) tried to explain this phenomena by hypothesizing that as the spin rate approached zero due to YORP (which is the hypothesized driving force), the satellite lost its angular momentum and began to tumble as shown by the simulation on the right side of the figure. As we can see, the preferred

143
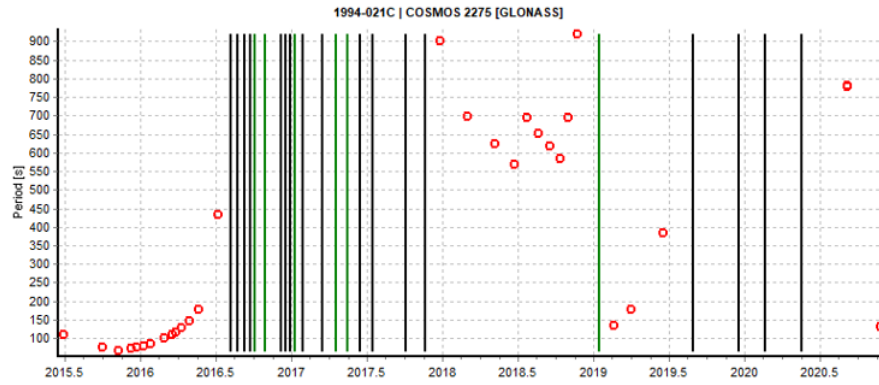
Figure E.2.: Spin period evolution of COSMOS 2275. Red circles indicate periods, black lines indicate slow rotator light curves, and green lines indicate unfinished light curves (due to their complexity).
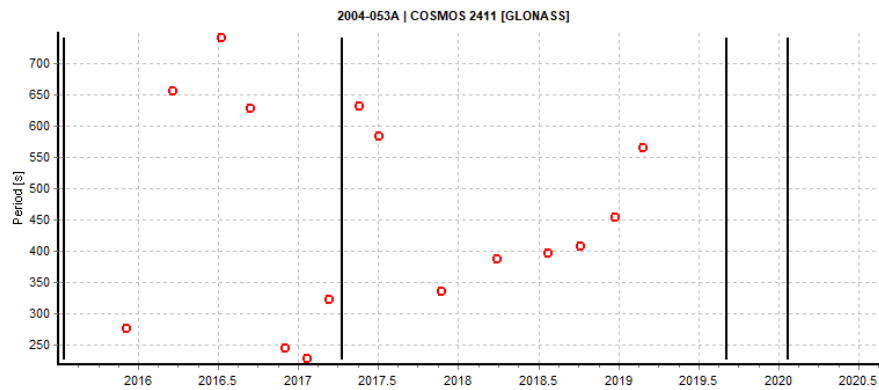

Figure E.3.: Spin period evolution of COSMOS 2411. Red circles indicate periods, black lines indicate slow rotator light curves, and green lines indicate unfinished light curves (due to their complexity).

tumbling axis is the y-axis which is the axis with minimum inertia (according to Fig. E.5) since this axis requires the minimum torque to accelerate. While spinning up about this axis, energy dissipation starts to dominate (discussed in Section 2.2.3) which eventually causes the satellite to return to stable uniform rotation about the axis of maximum inertia (z-axis). With all excess energy dissipated, YORP again becomes the most dominant perturbation and the cycle starts over.
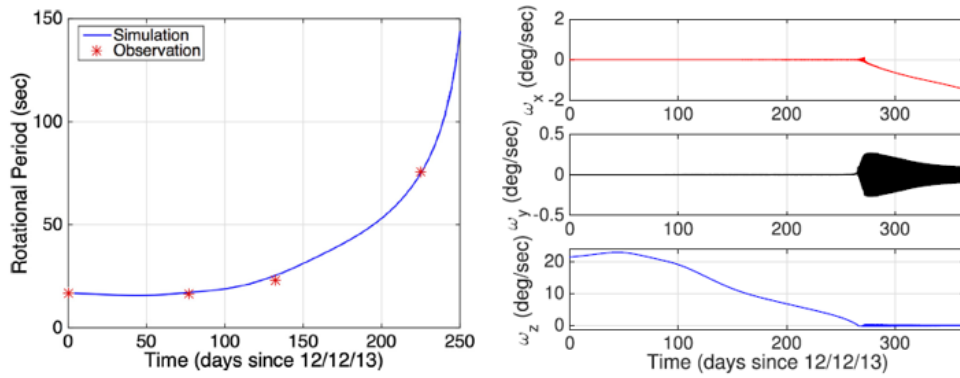
Figure E.4.: Rotational period of GOES-8 satellite from observation and simulation (left) and the satellite angular velocity evolution (right) (*Albuja et al.*, 2018).
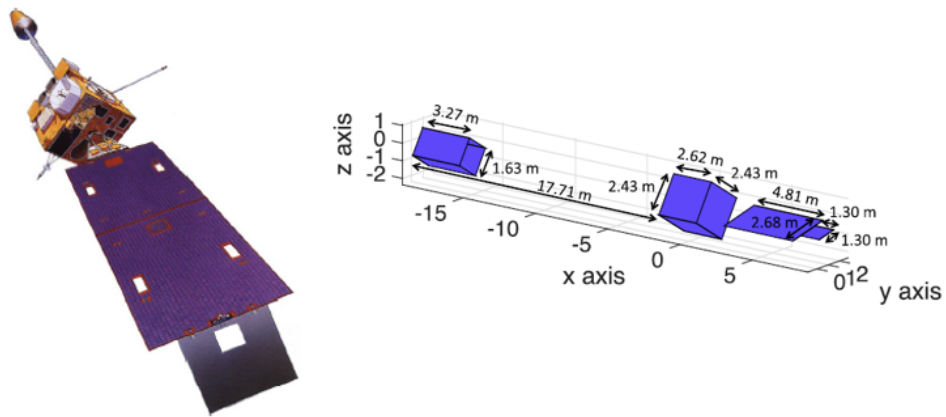
Figure E.5.: GOES-8 satellite (left) and its full model (right) (*Albuja et al.*, 2018).

Bibliography

Albuja, A., and D. J. Scheeres (2013), Defunct satellites, rotation rates and the YORP effect, in *2013 AMOS Technical Conference Proceedings*, pp. 156–163.

Albuja, A. A., D. J. Scheeres, and J. W. McMahon (2015), Evolution of angular velocity for defunct satellites as a result of YORP: An initial study, *Advances in Space Research*, *56*(2), 237–251.

Albuja, A. A., D. J. Scheeres, R. L. Cognion, W. Ryan, and E. V. Ryan (2018), The YORP effect on the GOES 8 and GOES 10 satellites: A case study, *Advances in Space Research*, *61*(1), 122–144.

Benson, C., D. J. Scheeres, W. H. Ryan, E. V. Ryan, and N. Moskovitz (2017), Rotation state evolution of retired geosynchronous satellites, in *2017 AMOS Technical Conference Proceedings*.

Benson, C. J., D. J. Scheeres, W. H. Ryan, and E. V. Ryan (2018), Cyclic complex spin state evolution of defunct GEO satellites, in *2018 AMOS Technical Conference Proceedings*.

Benson, C. J., D. J. Scheeres, W. H. Ryan, E. V. Ryan, and N. A. Moskovitz (2020), GOES spin state diversity and the implications for GEO debris mitigation, *Acta Astronautica*, *167*, 212–221.

Diebel, J. (2006), Representing attitude: Euler angles, quaternions, and rotation vectors, in *Tech Rep.*, Stanford University Palo alto, CA.

Domınguez-González, R., N. Sánchez-Ortiz, F. Cacciatore, J. Radtke, and S. Flegel (2013), Disposal strategies analysis for MEO orbits, in *64th International Astronautical Congress, Beijing, China*, pp. 23–27.

Earl, M. A. (2017), Photometric analysis and attitude estimation of inactive box-wing geosynchronous satellites, PhD thesis, Royal Military College of Canada.

Earl, M. A., P. W. Somers, K. Kabin, D. BÃšdard, and G. A. Wade (2018), Estimating the spin axis orientation of the Echostar-2 box-wing geosynchronous satellite, *Advances in Space Research*, *61*, 2135–2146.

Hugentobler, U., and O. Montenbruck (2017), Satellite orbits and attitude, in *Springer Handbook of Global Navigation Satellite Systems*, edited by P. J. G. Teunissen and O. Montenbruck, Springer.

Hughes, P. C. (2004), *Spacecraft attitude dynamics*, Dover Publications, Inc.

Jenkin, A. B., and R. A. Gick (2001), Collision risk associated with instability of MEO disposal orbits, in *3rd European Conference on Space Debris*, ESA, Darmstadt, Germany.

Kanzler, R., J. Silha, T. Schildknecht, B. Fritsche, T. Lips, and H. Krag (2014), Space debris attitude simulation - iOTA (In-Orbit Tumbling Analysis), in *2014 AMOS Technical Conference Proceedings*.

Karrang, P., and R. Kanzler (2017), *iOTA Software User's Manual*, HTG, revision: 0.2.0 ed., ESA AO/1-7803/14/D/SR.

Kelso, T. S. (2007), Analysis of the 2007 Chinese ASAT test and the impact of its debris on the space environment, in *2007 AMOS Technical Conference Proceedings*.

Kessler, D. J., and B. G. Cour-Palais (1978), Collision frequency of artificial satellites: The creation of a debris belt, *Journal of Geophysical Research: Space Physics*, *83*(A6), 2637–2646.

Kirchner, G., M. Steindorfer, P. Wang, F. Koidl, D. Kucharski, J. Silha, T. Schildknecht, H. Krag, and T. Flohrer (2017), Determination of attitude and attitude motion of space debris, using laser ranging and single-photon light curve data, in *7th European Conference on Space Debris*, ESA, Darmstadt, Germany.

Koller, P. (2016), Attitude determination of cylindrical rocket bodies from optical light curves, Bachelor's thesis, Astronomy Institute of the University of Bern.

Lin, H.-Y., et al. (2019), Tiangong-1's accelerated self-spin before reentry, *Earth, Planets and Space*, *71*(1), 1–9.

Linder, E., J. Silha, T. Schildknecht, and M. Hager (2015), Extraction of spin periods of space debris from optical light curves, in *66th International Astronautical Congress*, IAC-15-A6.1.2, Jerusalem, Israel.

Liou, J.-C. (2011), An active debris removal parametric study for LEO environment remediation, *Advances in Space Research*, *47*(11), 1865–1876.

Liou, J.-C., and N. L. Johnson (2008), Instability of the present LEO satellite populations, *Advances in Space Research*, *41*(7), 1046–1053.

Lips, T., et al. (2017), Debris attitude motion measurements and modeling-observation vs. simulation, in *2017 AMOS Technical Conference Proceedings*, p. 19.

NASA (2008), *Handbook for Limiting Orbital Debris*, NASA, Washington, DC 20546, NASA-Handbook 8719.14.

NASA ODPO (2013), An update of the FY-1C, Iridium 33,and Cosmos 2251 fragments, *Orbital Debris Quarterly News*, *Volume 18, Issue 1*.

NASA ODPO (2014), Fengyun-1C debris cloud remains hazardous, *Orbital Debris Quarterly News*, *Volume 17, Issue 1*.

NASA ODPO (2018), History of on-orbit satellite fragmentations - 15th edition, *tech. report.*

NASA ODPO (2020a), The 2019 U.S. Government Orbital Debris Mitigation Standard Practices, *Orbital Debris Quarterly News, Volume 24, Issue 1.*

NASA ODPO (2020b), Monthly effective number of objects in earth orbit, *Orbital Debris Quarterly News, Volume 24, Issue 2.*

NASA ODPO (2020c), The tracked objects in low earth orbit: 2000-2020, *Orbital Debris Quarterly News, Volume 24, Issue 4.*

National Research Council (1995), *Orbital Debris: A Technical Assessment*, The National Academies Press, Washington, DC.

Nishida, S.-I., and S. Kawamoto (2011), Strategy for capturing of a tumbling space debris, *Acta Astronautica, 68*(1-2), 113–120.

Ojakangas, G. W., and N. Hill (2011), Toward realistic dynamics of rotating orbital debris and implications for light curve, in *2011 AMOS Technical Conference Proceedings.*

Papushev, P., Y. Karavaev, and M. Mishina (2009), Investigations of the evolution of optical characteristics and dynamics of proper rotation of uncontrolled geostationary artificial satellites, *Advances in Space Research, 43*, 1416–1422.

Pardini, C., and L. Anselmo (2012), Post-disposal orbital evolution of satellites and upper stages used by the GPS and GLONASS navigation constellations: The long-term impact on the Medium Earth Orbit environment, *Acta Astronautica, 77*, 109–117.

Pittet, J.-N., J. Šilha, and T. Schildknecht (2018), Spin motion determination of the Envisat satellite through laser ranging measurements from a single pass measured by a single station, *Advances in Space Research, 61*(4), 1121–1131.

Pontieu, B. D. (1997), Database of photometric periods of artificial satellites, *Advances in Space Research, 19*, 229–232.

Rachman, A., T. Schildknecht, J. Silha, J.-N. Pittet, and A. Vananti (2017), Attitude state evolution of space debris determined from optical light curve observations, in *68th International Astronautical Congress*, IAC-17-F1.2.3, Adelaide, Australia.

Rachman, A., T. Schildknecht, and A. Vananti (2018), Analysis of temporal evolution of debris objects' rotation rates inside AIUB light curve database, in *69th International Astronautical Congress*, IAC-18-A6.3, Bremen, Germany.

Rachman, A., A. Vananti, and T. Schildknecht (2020), Understanding the oscillating pattern in the rotational period evolution of several GLONASS satellites, in *2020 AMOS Technical Conference Proceedings.*

Revnivykh, S., A. Bolkunov, A. Serdyukov, and O. Montenbruck (2017), GLONASS, in *Springer Handbook of Global Navigation Satellite Systems*, edited by P. J. G. Teunissen and O. Montenbruck, Springer.

Rossi, A., E. M. Alessi, G. B. Valsecchi, H. G. Lewis, C. Colombo, L. Anselmo, C. Pardini, F. Deleflie, and K. Merz (2017), MEO dynamics and GNSS disposal strategies, in *7th European Conference on Space Debris*, ESA, Darmstadt, Germany.

Rubincam, D. P. (2000), Radiative spin-up and spin-down of small asteroids, *Icarus*, *148*(1), 2–11.

Sagnières, L. B. M. (2020), *D-SPOSE Software User Manual*, Department of Mechanical Engineering, McGill University.

Schildknecht, T. (2007), Optical surveys for space debris, *The Astronomy and Astrophysics Review*, *14*(1), 41–111.

Schildknecht, T., R. Musci, C. Früh, and M. Ploner (2008), Color photometry and light curve observations of space debris in GEO, in *2008 AMOS Technical Conference Proceedings*, pp. 17–19.

Schildknecht, T., E. Linder, J. Silha, M. Hager, N. Koshkin, E. Korobeinikova, S. Melikiants, L. Shakun, and S. Strakhov (2015), Photometric monitoring of non-resolved space debris and databases of optical light curves, in *2015 AMOS Technical Conference Proceedings*, p. 25.

Shan, M., J. Guo, and E. Gill (2016), Review and comparison of active space debris capturing and removal methods, *Progress in Aerospace Sciences*, *80*, 18–32.

Shappirio, M., et al. (2016), Application of satellite laser ranging techniques for space situational awareness efforts, in *2016 AMOS Technical Conference Proceedings*.

Silha, J., E. Linder, M. Hager, and T. Schildknecht (2015), Optical light curve observations to determine attitude states of space debris, in *30th International Symposium on Space Technology and Science, Kobe-Hyogo, Japan*.

Silha, J., J.-N. Pittet, M. Hamara, and T. Schildknecht (2018), Apparent rotation properties of space debris extracted from photometric measurements, *Advances in Space Research*, *61*, 844–861.

Silha, J., et al. (2017), Debris attitude motion measurements and modelling by combining different observation techniques, in *7th European Conference on Space Debris*, ESA, Darmstadt, Germany.

UNOOSA (2010), Space Debris Mitigation Guidelines of the Committee on the Peaceful Uses of Outer Space.

Wertz, J. R. (1978), *Spacecraft attitude determination and control*, vol. 73, Springer Science & Business Media.

Wilde, M., J. Harder, and E. Stoll (2019), Editorial: On-orbit servicing and active debris removal: Enabling a paradigm shift in spaceflight, *Frontiers in Robotics and AI*, *6*, 136, doi:10.3389/frobt.2019.00136.

Yanagisawa, T., and H. Kurosaki (2012), Shape and motion estimate of LEO debris using light curves, *Advances in Space Research*, *50*, 136–145.

Declaration of consent

on the basis of Article 18 of the PromR Phil.-nat. 19

Name/First Name: Rachman/Abdul

Registration Number: 15-136-666

Study program: PhD in Physics with special qualification in Astronomy

Bachelor ☐   Master ☐   Dissertation ✔

Title of the thesis: Understanding attitude behavior of inactive GLONASS satellites
using spin period evolution

Supervisor: Prof. Thomas Schildknecht

I declare herewith that this thesis is my own work and that I have not used any sources other than
those stated. I have indicated the adoption of quotations as well as thoughts taken from other authors
as such in the thesis. I am aware that the Senate pursuant to Article 36 paragraph 1 litera r of the
University Act of September 5th, 1996 and Article 69 of the University Statute of June 7th, 2011 is
authorized to revoke the doctoral degree awarded on the basis of this thesis.
For the purposes of evaluation and verification of compliance with the declaration of originality and the
regulations governing plagiarism, I hereby grant the University of Bern the right to process my
personal data and to perform the acts of use this requires, in particular, to reproduce the written thesis
and to store it permanently in a database, and to use said database, or to make said database
available, to enable comparison with theses submitted by others.

Kupang, 19.04.2023

Place/Date

Signature

Curriculum Vitae

Personal information

Name	:	Abdul Rachman
Date of birth	:	29.11.1974
Place of birth	:	Makassar, Indonesia
Nationality	:	Indonesia

Education

2023   PhD Candidate in Astronomy,
        Astronomical Institute, University of Bern, Bern, Switzerland
        Thesis: Understanding attitude behavior of inactive GLONASS satellites using spin period evolution

2012   Master of Science in Astronomy,
        Institut Teknologi Bandung, Bandung, Indonesia
        Thesis: Effects of energetic charged particles related to CME and CIR to GSO satellite operations from 1997 to 2011

2000   Bachelor of Science in Astronomy,
        Institut Teknologi Bandung, Bandung, Indonesia
        Thesis: Changing of an Earth's satellite orbit using Moon's gravity

Work Expericences

2021 - now   National Research and Innovation Agency (BRIN),
              Indonesia

2005 - 2021   National Institute of Aeronautics and Space (LAPAN),
              Indonesia